Palaeoenvironment of a Late Triassic microbialite: clumped isotopes in the Cotham Marble.

Stefania Anastasia Schinaia
100299783/1

A thesis submitted for the degree of
Master of Science by Research in Environmental Sciences

School of Environmental Sciences

University of East Anglia

September 2023

Abstract

The Cotham Marble is a late-Triassic microbialite of Rhaetian (late Triassic) age, present in parts of SW Britain (especially the Bristol area), at the top of the Upper Cotham Member (Lilstock Formation, Penarth Group). The Cotham Marble consists of cycles of microbialites growing principally with laminated or dendrolitic morphologies. The combined use in this study of clumped isotope and high-resolution stable isotope analyses, backed by sedimentological observations, provides insights into the palaeoenvironmental conditions that facilitated development of the microbialites and the underlying facies of the Upper Cotham Member.

The study focussed on material from Wickwar (Gloucestershire) and the Δ_{47}-derived temperatures from clumped isotope analyses show that microbialite depositional temperatures were generally warmer (ca. +12 to +26 °C) than those in an underlying thrombolite and non-microbial micrites (+8 to +12 °C). Moreover, evidence of temperature seasonality in the laminar and dendrolitic microbialite facies identified in previous studies was not found in the specimen from Wickwar. A distinct negative inorganic carbon isotope excursion was discovered in the first laminar stromatolite and is consistent with earlier work that implicated a phase of prolific microbial mat growth as a source of isotopically light carbon to the Cotham lagoon water. The combined data on modern microbial analogues, clumped isotopes and stable isotope analyses overall suggest that: (a) regressive conditions promoted deposition of the lower facies of the Upper Cotham Member in cool, coastal marginal lagoons of broadly non-marine character; (b) the Cotham Marble microbialites developed during sea-level stillstand in quasi-marine, warm lagoons where evaporation was common and water residence times relatively long; (c) alternating conditions of exposure and inundation created the hydrodynamic conditions under which laminar stromatolites and dendrolites developed, respectively; (d) longer exposure may have facilitated formation of desiccation surfaces within the laminar stromatolites and transitory colonisation of burrowing organisms in the latter two laminar stromatolitic phases.

Table of Contents

List of Figures

List of Tables

Acknowledgments

I would like to thank my supervisory team, Prof. Julian Andrews, Prof. Paul Dennis, and Dr Alina Marca, for their constant support during my research and for being always available to find time to discuss any matter concerning the research and the administrative aspects of the master's degree. Furthermore, I would like to thank Prof. Julian Andrews for giving me the opportunity to undertake this research on an intriguing and fascinating microbialite such as the Cotham Marble, for guidance and discussion on the specific aspects of the research and the writing of the thesis and for proofreading. I would like to thank Prof. Paul Dennis for the opportunity to access the Stable Isotope Laboratory (SIL), for his willingness to explain all scientific and technical aspects of the MIRA mass spectrometer and any other device in the lab, for his help with the methods chapter in the thesis and for 'creating' and constantly 'perfecting' the MIRA. I would like to thank Dr Alina Marca for her constant guidance and support on all aspects of the clumped isotope and stable isotope analyses, for her willingness to explain all processes involved in the analyses run in the SIL, and for help in all UEA matters.

Thanks to Dr Richmal Paxton because her research improved the clumped isotope analyses for this research and the related methods chapter. I would like to thank Mr Betrand Lezé for the opportunity to run RDX and SEM analyses, for making possible the process of thin section preparation in the lab and for preparing the thin sections that made possible the descriptions of the microstructures of the specimen. I would like to thank Mr Simon Ellis for his help and skills in cutting and polishing the specimen in the lab.

I would also like to thank everybody mentioned for their dedication during the difficult and challenging years of the pandemic.

Finally, many thanks to my family and my friends, Grace, Lucia, Andy, Claire, Elena, Susan, Harry, Monica, Mara, and many more, for being constantly supportive.

CHAPTER 1

Introduction and aims of the study.

1.1 Introduction.

Continental carbonates from caves, rivers and lakes have been widely used to extract terrestrial palaeoenvironmental information, because they record geochemical characteristics of their parent waters (e.g. Andrews et al., 1997; Andrews and Brasier, 2005; Andrews, 2006, Brasier et al., 2010). The stable oxygen ($\delta^{18}O$) and carbon ($\delta^{13}C$) isotope composition of carbonates are particularly useful and may be related to climatic or other environmental parameters. The temperature-dependent fractionation of oxygen isotopes between water and calcite precipitating from it, is one of the most widely used relationships to reconstruct the temperature at which carbonates precipitate (Kele et al., 2015). In addition, stable carbon isotopes ($\delta^{13}C$) are influenced by the principal carbon source in the water, e.g. soil CO_2, atmospheric CO_2 or CO_2 from aquifer rock dissolution (Andrews et al., 1997).

An increasing number of studies have attempted to reconstruct temperatures and short-term climatic changes in ancient deposits (e.g. see Arp et al., 2005; Brasier et al., 2010; Dabkowski et al., 2011; Brasier, 2011; Arenas et al., 2019; Martin-Bello et al., 2019). However, major constraints to the use of ancient carbonates for palaeoclimatic reconstructions include the lack of chronological data, potential for diagenetic alteration of original isotopic signal, microenvironmental conditions that alter the geochemical balance of oxygen isotope fractionation during calcite precipitation (Andrews et al., 1997) and precise knowledge of the oxygen isotope composition of the water from which the carbonate precipitated (McCrea, 1950; Urey et al.,1951).

The carbonate clumped isotope thermometer avoids the requirement for knowledge of the $\delta^{18}O$ of the originating water, and can thus be applied to carbonates in the geological record where stable isotope composition of waters are largely unknown (Gosh et al., 2006; Eiler, 2007). This technique is based on the proportionality between measured

excess abundance of $^{13}C^{18}O$-bonds in carbonate relative to its stochastic distribution (represented by Δ_{47}) and the carbonate precipitation temperature (Eiler, 2007; Kele et al., 2015). The excess abundance of $^{13}C^{18}O$-bonds is not dependent on the bulk carbonate isotopic composition (Eiler, 2007).

Microbial carbonates, including stromatolites, have great potential for palaeoclimatic reconstruction in deep geological time. However, there are several uncertainties regarding the use and interpretation of Δ_{47}-temperature data from microbial carbonates for reconstruction of depositional palaeotemperatures and environmental conditions (Hren and Sheldon, 2019). Measured Δ_{47}-temperatures may not reflect primary depositional temperatures but may record a combination of depositional and diagenetic (burial) temperatures and other secondary effects (Hren and Sheldon, 2019). For example, if carbonate precipitates as a result of rapid CO_2 degassing, kinetic isotope effects may decrease Δ_{47} values, resulting in an increase in apparent temperature (Hren and Sheldon, 2019). Also, due to their high porosity, microbial carbonates are particularly susceptible to post-depositional fluid-mediated diagenesis, such that meteoric fluids may modulate the original $\delta^{18}O$ composition, while burial fluids may alter both $\delta^{13}C$ and $\delta^{18}O$ toward lower values (Fairchild et al., 1990; Siahi et al, 2018; Hohl and Viehmann, 2021). If, however, the microbial carbonate forms at or near isotopic equilibrium, Δ_{47} data should yield reliable temperatures, unless fluid-mediated diagenetic alteration or solid-state reordering (during burial) occurs (Hren and Sheldon, 2019; Henkes et al., 2014). Recent studies (e.g. Frantz et al., 2014; Petryshyn et al., 2016) show that modern and recent microbialites yield Δ_{47} data that appear to reproduce water temperatures of formation reasonably well (Hren and Sheldon, 2019). Although the extent of kinetic bias on temperature relationships is not fully known, microbial carbonate temperatures recorded by modern carbonate Δ_{47} data are generally consistent with modern environmental conditions and represent at best a seasonal maximum (e.g. Petryshyn et al., 2016; Hren and Sheldon, 2012; Hren and Sheldon, 2019).

Stromatolites are organosedimentary deposits found as domes, columns or sheet-like masses, widely defined as layered, early-lithified, authigenic microbial structures that form at the sediment-water interface in freshwater, marine and evaporitic environments (Riding, 2010). The most ancient stromatolites have been found in Archean formations of ca. 3.5 Ga (e.g. Walter et al., 1980) in Pilbara Craton (Western Australia) and possibly

in even older rocks (3.7 Ga) in the Greenstone Belt in Greenland (Nutman et al., 2016), although the biogenic origin of the latter is disputed (Allwood et al., 2018).

Thrombolites, dendrolites and leiolites are categories of non-layered microbial deposits characterised by clotted, dendritic, and aphanitic (or structureless), macrofabrics, respectively (Riding, 2010). The term 'thrombolites', from the Greek word 'thrombos' meaning clot, was first introduced to the geological community in the 1960s by Aitken (1967) to describe structures consisting of a mesoscopically clotted texture, with millimetre to centimetre-size clots within a larger domal/columnar macrostructure (Kennard and James, 1986). The absence of any macroscopic framework-builders suggests that microbes are the main organisms responsible for the formation of the clots (Lee, 2021). Although there is a possible 1.9 Ga old thrombolite, the first known recognised appearance of thrombolites is in the Neoproterozoic and they are most commonly found in Cambro-Ordovician strata (Lee, 2021). Dendrolites, from the Greek word 'dendron' meaning 'tree', refers to a type of thrombolite with bush-like branching clots, where the dendritic structure is thought to be indicative of evidence of microbially-induced precipitation of calcite, rather than trapping and binding of detrital sediment (Lee, 2021). Leiolites, from the Greek word meaning 'smooth', lack generally clear lamination or structure and are described as massive or homogeneous mesostructures with a domal or columnar macrostructure that suggests their biological origin (Lee, 2021).

Stromatolites were first identified and attributed to 'algal activity' (broadly cyanobacterial) by Ludwig and Theobald (1852; in Gehler and Reich, 2010) while observing algal carpets and oolitic grains in the thermal waters of Bad Nauheim (Hesse, Germany) (Krumbein, 2008; Gehler and Reich, 2010). Ernst Louis Kalkowsky (1851–1938) observed the same features in Bad Nauheim and confirmed their biosedimentary character attributed to microorganisms (Krumbein, 2008). By describing them as made of '...a fine, more or less even layered fabric...', Kalkowsky introduced the term 'Stromatolith' to the earth science community in 1908 (Kalkowski, 1908; in Gehler and Reich, 2010; Paul et al., 2010). The pioneering work of Kalkowsky was contested by most geologists in Germany and was not accepted until several years after his death (Gehler and Reich, 2010).

1.2 Aims of the study.

The research aim of the work described here is to use clumped isotope and high-resolution stable isotope techniques to reconstruct the environmental conditions during deposition of the Triassic Cotham Marble, a well-known ancient microbialite deposit.

The Cotham Marble is a late-Triassic microbialite of the Rhaetian stage, present mostly in parts of SW Britain, at the top of the Upper Cotham Member within the Lilstock formation of the Penarth Group. Contrary to its name, the Cotham Marble, is not a metamorphosed limestone, but an association of microbialite forms, predominantly laminar and dendrolitic, interspersed with mechanical sediment deposition. The resulting association provides a striking resemblance in polished section to various representations of landscapes depicted with trees, hedges, ploughed fields, skies and clouds. The Cotham Marble, therefore, derives its name by its use as a decorative building stone, particularly popular in Victorian times (Fox, 2018). The first published description was in 1754 by Edward Owen who referred to it as the 'Landscape Marble', as it was known at the time in the area of Bristol (Thompson, 1894). It was then called 'Cotham Stone' because it was quarried with other materials near Cotham House north of Bristol (Thompson, 1894). According to Thompson (1894), "At the time of Owen the Cotham Stone was chiefly known by, and valued for, its peculiar, corrugated, upper surface, 'rustick' so-called, though some cut and polished specimens were to be found framed in the houses of 'the gentlemen of the neighbourhood. Nowadays, the Cotham Marble is still used as an ornamental rock and also for jewellery.

The Cotham Marble has been the focus of a number of studies to Interpret Its morphogenesis (e.g. Wright and Mayall, 1981; Ibarra et al., 2015), some of which more recently included the use of stable isotope geochemistry (Ibarra et al., 2016; Petryshyn et al., 2020) to investigate the possibility that the sedimentological and palaeontological peculiarities of the Cotham Marble could be a manifestation of end-Triassic mass extinction (Ibarra et al., 2016; Petryshyn et al., 2020). Using clumped isotope geochemistry, Petryshyn et al. (2020) reported a pattern of alternating higher and lower temperatures that indicated that the laminar and dendrolitic facies are the result of millennial-scale seasonality, driven by external (global) climatic conditions.

This study aims to investigate and extend the findings of previous studies, in particular the apparent seasonality signal in the laminar and dendrolitic microbialite facies. The

investigation focuses on a specimen from Wickwar, in Gloucestershire, England. The combined use of high-resolution clumped isotope and bulk isotope analyses backed by sedimentological observations provides further insights into the palaeoenvironmental conditions that facilitated development of the Cotham Marble microbialite. Unlike previous studies, the analyses and observations have been extended to facies of the Upper Cotham Member underlying the Cotham Marble to provide further sedimentological and geochemical context to the environmental conditions preceding development of the microbialites.

This thesis includes a literature review (Chapter 2) of previous studies on the Cotham Marble and on examples of modern microbialite analogues with features similar to those seen in the Cotham Marble. Chapter 3 describes the stratigraphic setting of the Late-Triassic at Wickwar, followed by description of the stable and clumped isotope geochemistry techniques used in the research. In Chapter 4, the results of the research are presented, including a description of new or undescribed sedimentological features and the results from the clumped isotope and bulk isotope analyses. In Chapter 5, the results are interpreted, followed by conclusions and suggestions for follow-up research.

CHAPTER 2

The Cotham Marble

2.1 Introduction.

The Cotham Marble is a microbialite association at the top of the Upper Cotham Member within the Lilstock Formation of the Penarth Group (Warrington et al., 1980; Mayall, 1983). The Cotham Member, formerly the Cotham Beds, have traditionally been regarded as Rhaetian in age (late Triassic) (Rhaetic Beds in Woodward, 1892; Hamilton, 1961) although work by Hesselbo et al. (2004), correlating globally significant carbon isotope spikes complicates this as discussed later (Chapter 5). The Cotham Member is about 1-3 m thick comprising blue to pale grey limestones and grey or greenish-grey mudstones, with ripple marks and desiccation cracks (Hamilton and Whittaker, 1977). The Cotham Marble has long been identified as a dark grey limestone of algal stromatolitic origin (Hamilton (1961). The term 'algal' is today related only to algae and not any longer to bacteria, therefore, in this thesis the term 'microbial' is used.

The Cotham Member is divided into lower and upper parts at the top of a prominent 'deformed bed' (Mayall, 1983) characterised by soft sediment deformation and identifiable over most of SW England and the southern margin of Wales. The top of the 'deformed bed' is characterised by a fissured surface with desiccation cracks up to ca 0.9-1 m deep (Mayall, 1983; Hesselbo et al., 2004). According to Mayall (1983), due to the large deep desiccation cracks, if the water depth was about 1 m the deformation was probably caused by earthquake activity and an associated uplift in the order of 1- 2 m in the north Somerset and south Wales area. The deformed bed has been interpreted as the result of seismic activity associated with the opening of the Atlantic Ocean (Swift and Martill, 1999) or deformation caused by an extra-terrestrial impact (Simms, 2003; 2007).

The Upper Cotham Member does not exhibit synsedimentary deformation (Ibarra et al., 2014) and Hesselbo et al. (2004) place a sequence boundary at the fissured bed. While the Lower Cotham Member is a shallowing upward succession, capped by a surface

characterised by desiccation cracks that reflect a dramatic fall in relative sea level, the Upper Cotham Member represents a coastal environment that was deposited during a subsequent relative sea level rise (Hesselbo et al., 2004), or stillstand, and was characterised by alternating periods of restriction and connection to the open ocean on a storm dominated ramp.

Although the Cotham Member is widespread in southwest England (Fig 2.1), the occurrence of the microbialite (Cotham Marble) is discontinuous (Wright and Mayall, 1981; Mayall and Wright, 2015; Ibarra et al., 2014, 2015). Microbialites are not present in the sections around the shores of the Bristol Channel, such as Lavernock Point and St. Audrie's Bay (Figure 2.1), but are present in the inner Bristol Channel area, the Mendips and around the city of Bristol (Ibarra et al., 2014). The Cotham Marble, where present, is in most places, overlain by mudstones and limestone of the Jurassic Blue Lias (Radley and Carpenter, 1998; Simms, 2007), but the picture is confused by local erosion surfaces present at this stratigraphic level.

In the Bristol and Mendip area the Cotham Marble microbialites show a surprisingly similar microstratigraphy, a cyclic mesomorphology consisting of alternating laminated and dendrolitic intervals of microbial origin (Ibarra et al., 2016). Generally, a number of outcrops (Manor Farm Quarry, Lower Woods Nature Reserve (Wickwar), Cotham House; Figure 2.1) show a similar morphology resulting from two cycles of alternating laminated and dendrolitic intervals, with specimens from localities even tens of kilometres apart showing very similar features. Specimens from other sites may show either three cycles or only one complete cycle of laminated and dendrolitic intervals.

The British Rhaetic (***sensu lato***) sedimentology broadly reflects a complex transgressive setting (Hesselbo et al, 2004) during which a low-relief coastal landscape was affected by mild tectonic activity (Wright and Mayall, 1981). The analysis of clay minerals suggests a broadly humid climate (Wright and Mayall, 1981). The palaeontology of the Cotham Member includes the branchiopod *Euestheria*, ostracods including *Darwinula* and the bryophyte *Naiadites* (Hamilton, 1977; Hamilton and Whittaker, 1977; Wright and Mayall, 1981). Such fauna probably indicates the presence of a shallow-water brackish or schizohaline lagoons (Wright and Mayall, 1981). Around Bristol specifically, Wright and Mayall (1981) note the presence of bivalve coquinas and Mayall (1979) identified *Modiolus* sp. Below the microbial horizon, suggesting lagoonal restricted-

marine conditions. Above the stromatolite the low biodiversity of the faunal association again indicates a restricted marine environment (Wright and Mayall, 1981).

2.2 Microbialite morphology.

Detailed investigations of the Cotham Marble in the Bristol area were first provided by Wright and Mayall (1981; Figure 2.2) and followed up more recently by Ibarra et al. (2014, 2016) and Petryshyn et al. (2020). These authors studied specimens that are very similar to the specimen investigated in this study; indeed, the Lower Woods (Figure 2.1) locality is immediately adjacent to the Wickwar site, north-east of Bristol, that provided the samples used in this study and can be regarded as the same locality. In all these studies from the Bristol area, five growth stages of microbialite were identified comprising three laminated (L1, L2, L3) and two dendritic (D1, D2) mesostructural elements that alternate (Figure 2.3). The following morphological descriptions are mainly based around the key papers of Wright and Mayall (1981) and Ibarra et al. (2014).

The overall morphology of the microbialites is characterised by rounded mammilated structures between 10 cm (near the edges) up to 16 cm thick, with a diameter of between 60 cm to 150 cm (Wright and Mayall, 1981). The microbialites are often developed over mounds surrounded by depressions that may contain clay-flake breccias. Vertical sections show alternations of flat or domal, laminated units (LI, L2, L3) with thicker units characterised by dendrolitic, arborescent structures (D1, D2) within a matrix of coarsely-laminated fine sediment (Wright and Mayall, 1981).

The basal (earliest) laminae are characterised by scour and fill structures, and cross-lamination often made by graded silt, which may indicate a broadly mechanical depositional origin (Wright and Mayall, 1981). The laminated stromatolite units are dominated by mm-scale micritic laminae with some microspar; occasional coarser laminae are composed of peloids (up to 500 microns long) within a microspar cement. Wright and Mayall (1981) identified a widespread presence of spongiostromid fabrics, consisting of irregular or finely tubular fenestrae, similar to filament mold fenestrae described in modern microbial mats.

The laminae become domal upward, probably Indicating an Increasing microbial influence. The laminated units also assume a domal shape when they grow over and drape positive relief such as dendritic structures. Occasionally the small domes develop in small columnar structures and their lamination may became angulate to cuspate (Wright

and Mayall, 1981). Wright and Mayall (1981) noted that this angulation may be associated with the formation of dark subvertical lineations (up to 7 mm long and less than 0.5 mm wide), which they compare morphologically to the 'axial zones' of *Conophyton* sp., characterised by laminae organised in a conical structure. At some localities echinoderm grains and pseudomorphs after lenticular gypsum have been noted in L1 (Ibarra et al., 2014).

Over the laminated unit of L1 the dendrolitic structures of D1 grow abruptly. Likewise, these arborescent structures are overlain abruptly (terminated) by re-established laminated stromatolites (L2). The laminated units drape underlying arborescent structures with synoptic relief of 2 cm, which according to Ibarra et al. (2014) indicates that some dendrolites formed a relief of about 2 cm above the sediment surface.

The arborescent structures grew upward to around 5 cm maximum hight. Wright and Mayall (1981) describe them as being composed of micrite laminae, up to 50 microns thick, coating tubes of the enigmatic microfossil *Microtubus communis* Flugel 1964. These tubes, up to 2 mm long, are usually filled with sparry calcite and sometimes also partially filled with fine sediment. The organism that formed these tubes may have been a small serpulid worm (Flugel 1964). As *Microtubus* can be horizontal or subvertical compared to the axis of dendrolite growth, its orientation may have controlled the form of the arborescent structures (Wright and Mayall, 1981). However, Ibarra et al. (2014) restrict their description of these tubes to sub-round shaped, spar-filled fenestrae and dispute the widespread presence and importance of *Microtubus.* They do, however, emphasise the presence of pyritised filamentous structures within the internal micritic fabric of the dendrolites, and pyritic rims around the whole dendrolitic structures.

In basal D1 there are dark microdigitate structures, about 2 mm thick, on the upper surface of L1, the 'hedges' identified by earlier researchers (Owen, 1754; Hamilton, 1961; Wright and Mayall, 1981). These hedges display bands of micritic mesh-like fabric over which micritic laminations develop (Ibarra et al. 2014) (Figure 2.4). The larger dendritic forms in D1 develop on some of these microdigitate structures.

The arborescent structures form polygonal shaped spaces and the 'fill material' between dendritic structures is characterised by clayey micritic laminae up to 1 cm thick, slightly concave upward (Wright and Mayall, 1981). Cavities left by the laminated drapes over the tops of arborescent structures were later filled with sparry calcite cement (Wright and

Mayall, 1981). In thin section this fill is dominated by microsparry and sparitic fabrics, some of which are clearly neomorphic. Within this fill Ibarra et al. (2014; 2016) identified clusters of spherical, organic-walled cells with diagonal sutures, identified as prasinophyte algal cysts that may belong to the green alga *Tasmanites* (Ibarra et al., 2014; 2016).

The overall morphology of the next cycle (L2 and D2) and the final laminated unit (L3) are broadly similar to the lower cycle (L1/D2) so in the following I highlight the main differences.

In L2 and L3, there are complex networks of mm-scale microdigitate structures interpreted as small metazoan burrows by Wright and Mayall (1981); larger burrows of a few millimetres, which intersect the domes, also occur. However, Ibarra et al. (2014) interpret these structures as constructional 'growth shapes' formed by microdigitate stromatolites (Figure 2.5). Mayall and Wright (1981) also identified tufted mat structures in L2 similar to those seen in recent oscillatoriacean-dominated stromatolite mats. Tufts structures are rarely found in ancient stromatolites because of their low preservation potential (Park, 1977). Consequently, their preservation in the Cotham Marble indicates very early lithification.

The transition from L2 to D2 Is abrupt and there are no 'hedge fabrics' as seen In D1. The D2 dendritic structures are more elongate and narrower at the top compared to those in the lower cycle, but with more branching (Wright and Mayall, 1981). The D2 'dendrolitic structures' have more thrombolitic fabric according to Ibarra et al. (2014). The draping of L3 fabrics over D2 is much less marked, the transition being texturally gradational. The matrix of D2 contains detrital grains and sand-size bioclastic fragments within a micrite matrix and fenestrae larger than in D1 (Ibarra et al., 2014). Bioclasts include bivalve shells, fish bones, gastropods and round organic-walled structures (*Tasmanites*) although fewer than in D1 (Ibarra et al., 2014; 2016).

While the Cotham Marble is not present at either St. Audrie's Bay or Lavernock Point (Figure 2.1), at the latter locality, in oolitic beds above the prominent fissured horizon (described above), Ibarra et al. (2016) identified mm-scale dendrolitic fabrics reminiscent of the microbialite dendrolites. Moreover at both localities abundant filamentous microfossils are present in rippled facies of the Upper Cotham Member (St Audrie's Bay)

and correlative heterolithic facies (Lavernock Point). Prasinophyte cysts assignable to the green alga *Tasmanites* were also discovered at St Audrie's Bay.

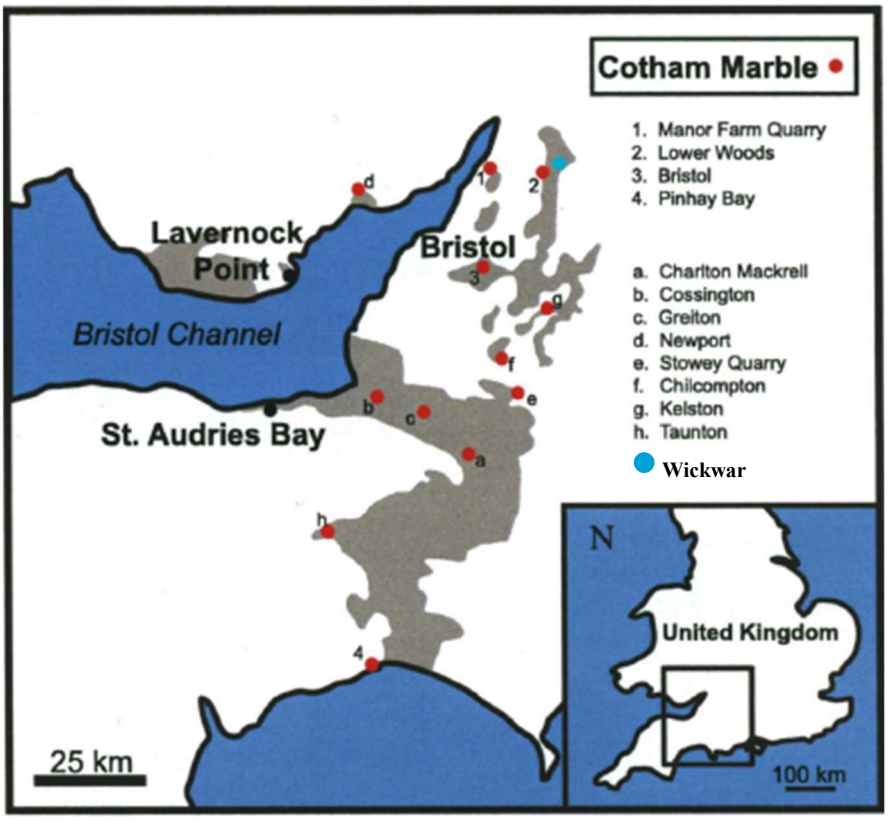

Figure 2.1 Distribution of known locations of the Cotham Marble. Locations 1 to 4 are those where specimens were investigated by Ibarra et al., (2014, 2016). The grey areas indicate Triassic-Jurassic strata. Figure adapted after Mander et al. (2008) and Ibarra et al. (2014).

Figure 2.2 Morphology of the vertical section of the stromatolite from Bristol investigated by Wright and Mayall (1981); laminated and domed units (A); arborescent units (B). Arrows point to microdigitate structures interpreted as burrows. Figure from Wright and Mayall (1981).

Figure 2.3 Cotham Marble specimen from Bristol investigated by Ibarra et al. (2014, 2016) and Petryshyn et al. (2020). Figure from Petryshyn et al. (2020).

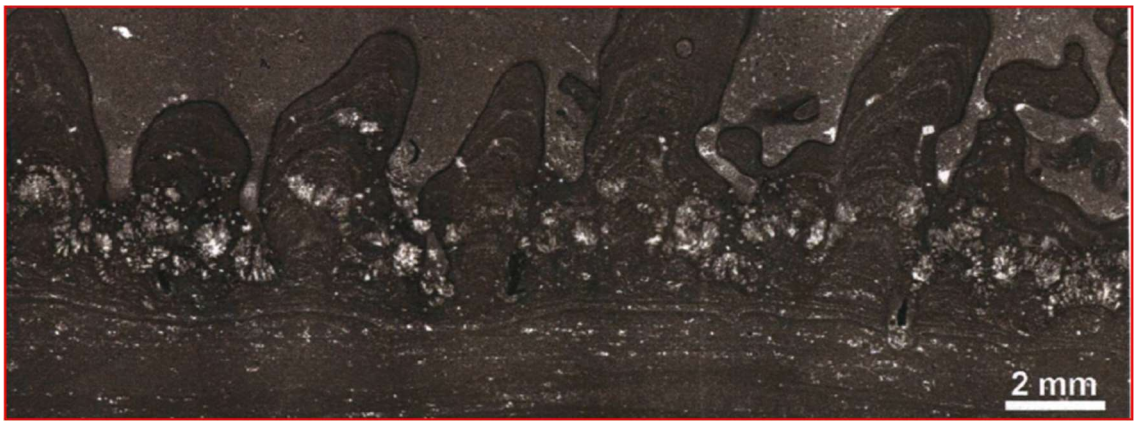

Figure 2.4 The hedges or microdigitate structures at the base of D1. Figure from Ibarra et al. (2014).

Figure 2.5 Laminae in L2 with microdigitate structures similar to burrows. Figure from Ibarra et al. (2014).

2.3 Morphogenetic reconstructions.

Wright and Mayall (1981) first discussed and interpreted the origin and development of the Cotham Marble in five stages.

Stage I refers to the basal sediment layers consisting of mechanically deposited and scoured sediments. Upward these layers show a passage to small domes of laminae of increasing thickness, which may indicate the colonisation of a filamentous microbial community, capable of binding sedimentary particles and therefore stabilizing the substrate. These small domes are replaced upward by tubular molds made of vertically growing microbial filaments. Stage I, thus, shows a community succession of increasing microbial influence from pioneering forms binding sediment to more consistent microbial colonisation (L1).

During Stage II there is formation of small crests or ridges out of the laminae, either abruptly or by clumping of microbial filaments with a narrowing of the lamina profile. This leads to the formation of polygonal patterns of ridges in plan view. In Stage III, the microbialridges provide a substrate for the development of the arborescent structures through the settling of *Microtubus* and the contemporary growth of microbes, in possible commensal association (Wright and Mayall, 1981).

During Stage IV, environmental stresses cause the disappearance of *Microtubus* and the reformation of microbial laminae draped over the arborescent structure in what is the next phase of laminated and domal growth (L2). In Stage V, the spaces between the ridges and arborescent structures are progressively filled with fine-grained sediment, forming a laminated deposit. Filling was completed in several stages during and after the growth of the arborescent structures, because the *Microtubus* structures appear buried at different stages of their development.

In their more recent morphogenetic interpretation, Ibarra et al. (2014) differ from the Wright and Mayall (1981) in some key areas. They downplay the importance (and largely the presence) of *Microtubus*, in the samples they examined from the Bristol area, (but countered by Mayall and Wright, 2015) interpreting round to elliptical structures as dendrolite three-dimensional branching, and in some cases ‘tubes’ formed by gas bubbles produced by the metabolism of microorganisms within the dendrolites. Similarly, they reject the identification of metazoan burrows and interpret the microdigitate fabrics as constructional ‘growth shapes’ formed by microdigitate stromatolites.

The overall growth environment was probably a coast marginal low-energy lagoon, impacted by some storms (micro cross laminae, detrital and biogenic grains) and some periods of desiccation that allowed gypsum precipitation at times. The presence of echinoderm fragments (Manor Farm samples) a few centimetres below D1 implies the presence of open seawater nearby because echinoderms are stenohaline organisms requiring normal marine salinity (Stickle and Diehl, 1987; Ibarra et al., 2014).

The botryoidal morphology of the external surface of the Cotham Marble, and the inference that the dendrolites had a relief of up to 2 cm, suggests that the dendrolites developed faster than the surrounding fill (Ibarra et al., 2014), which collected in depressions. The dendrolites probably formed a reticulate interconnected framework with 'honeycomb-style' depressions or tubes between. Early lithification of the reticulate structure clearly required lagoon waters supersaturated with respect to calcium carbonate.

Mayall and Wright (2015) disputed the down-played role of *Microtubus* in the formation of the microbialites argued by Ibarra et al. (2014, 2015). Mayall and Wright (2015) contend that *Microtubus*-stromatolite mounds from the Somerset coast, particularly east of Watchet Harbour, are constructed by an intimate association of *Microtubus communis* and laminar stromatolite. In some mounds, a second layer of *Microtubus*-laminar stromatolite starts to develop as seen in the 'landscape marble' but in a reduced form. Mayall and Wright (2015) also found common presence of tubular micrite-walled microfossils within the vertical digitate phase of growth in samples north of Bristol. In response, Ibarra et al. (2015) suggested that, although *Microtubus* is abundant in samples from Pinhay Bay, Dorset, and is present in northern outcrops, *Microtubus* is not necessary for the formation of the dendrolitic phases. They also argued that the 'reduced forms' in the mounds described by Mayall and Wright (2015) have a mesostructure different from the samples described in Ibarra et al. (2014), arguing that *Microtubus* may have inhibited the development of the dendrolite rather than promoting them in the mounds, hence the development of 'reduced forms'.

A major area of disagreement Is the regional distribution of the Cotham Marble in southwestern England and its significance for the end-Triassic mass extinction. Mayall and Wright (2015) disputed the assertion by Ibarra et al. (2014) that the Cotham Marble is present over an area of about 2,000 km^2, arguing that it only occurs locally around the

Bristol area. Mayall and Wright (2015) also contested the use of the term 'dead-zone' to describe the depositional environments above and below the Cotham Marble, because, firstly, the Late Triassic succession in SW Britain shows a number of abrupt faunal and facies changes likely associated with changes in salinity, substrate, oxygen levels and tectonic activity, and the sharp changes in facies observed within the Cotham Member is only one of such changes, rather than the product of a global event. Secondly, Mayall and Wright (2015) suggest that the low diversity biota is due to the likely brackish settings that characterise depositional environments positioned within a transgressive succession, between an underlying non-marine lagoonal sequence with a fauna of freshwater ostracods, brackish water bryophytes (*Naiadites*) and very limited bioturbation, and an overlying series of marls and limestones with abundant bioturbation and fully marine fauna.

Ibarra et al. (2015) agreed that, although discontinuous and patchy, similar Cotham Marble facies occur in localities about 100 km apart (e.g. Culverhole Point, Devon, and Lower Woods, Bristol). The authors argue that the identical microstratigraphy found about 100 km apart suggests that some facies of the Cotham Marble were deposited under identical regional-scale forcing and that non-local environmental factors were the dominant controls on the formation of the microbialite. Ibarra et al. (2015) assert that the Cotham Marble can be associated with the end-Triassic extinction event because of the combined manifestation of the following factors: a) its lateral extent, b) co-occurrence with a prasinophyte bloom also found in other coeval European sections, and c) occurrence at the same level as a negative stable isotope excursion in $\delta^{13}C_{org}$, which is a global marker of the end-Triassic extinction (Hesselbo et al., 2002, 2004). This latter point is considered further in Chapter 5.

2.4 Modern analogue microbialites.

Potential modern analogues to a number of the microbialite features of the Cotham Marble can be seen in specific modern microbial environments in the Persian Gulf, Australia, and California.

Microbialites of the coastal sabkhas of the southern shoreline of the Persian Gulf include both thrombolites and stromatolites. Although the presence of microbial features has long been known (Kendall and Skipwith, 1968), recent work by Paul et al. (2021) presents the

first detailed description of thrombolitic microbial structures from an intertidal pool, along with laminated stromatolitic sediments.

Thrombolites were found distributed within the pool as isolated domes or in discontinuous bands from decimetres to metres long, parallel to the pool margin (Paul et al., 2021). The thrombolite domes, characterised by a brown spongy fabric, are up to 20 cm in width and about 10 cm to 25 cm high above the pool hardground. A thin (1 mm) layer of bioclastic grains covers the upper surface of the thrombolites. Coccoid and filamentous forms of cyanobacteria were identified within the polygonal mats in the area. Marine brown and green algae are present at the outer margin of individual thrombolites and set the minimum water depth within the pool. During the measurement period, water temperatures in the pool ranged between 11.7°C and 46.8°C (Paul et al., 2021).

Each dome is characterised by two intervals: an upper thrombolite displaying radial laminations reflecting different microbial communities interlayered with bioclasts; and a lower laminated stromatolite up to 10 cm thick, attached to the pool hardground. Around the pool there are unlithified, finely-laminated, polygonal, microbial mats dominated by filamentous cyanobacteria. Elongate scours more than 1 m long and perpendicular to the shoreline interrupt the continuity of the polygonal mats (Paul et al., 2021).

Modern lithifying microbial mat communities are favoured in stressed environmental conditions that reduce or prevent colonisation from macroalgae and other eukaryotic organisms. In the case of the coastal sabkha in Abu Dhabi, in the uppermost intertidal zone, diurnal flooding maintains microbial growth, but exposure inhibits competition from grazing metazoans (Paul et al., 2021).

The formation of intertidal pools and their associated microbial communities mainly occurs under prevailing conditions of relative sea-level stillstand or, more likely, under the increasing hydrodynamic conditions associated with slow relative sea-level rise (Paul et al. 2021). Pool formation is initiated by high energy erosive events that remove any pre-existing binding microbial mat, exposing the underlying unconsolidated sediment. Consequently, scouring and coalescence of scours lead to pool development and widening by erosion of pool margins. Stromatolites then grow on occasionally exposed surfaces (Paul et al., 2021, Figure 14) with thrombolites growing over stromatolites along pool margins and on domes. Thrombolites seem to be restricted to growth on immersed surfaces. The alternation of high and low energy events and subsequent scouring leads

to the formation of isolated domes within the pool; low energy conditions favouring growth of microbial mats. Lithification by aragonite cement stabilises surfaces and limits further erosion during high energy events (Paul et al., 2021).

In Hamelin Pool, Shark Bay, Western Australia, Suosaari et al. (2018) have identified living dendrolitic microbial mats in intertidal, low energy environments which may be modern analogues for fossil dendrolitic microbialites. The Hamelin Pool dendrolites are formed by a community of microbes, dominated by filamentous cyanobacteria. Different microbial species have specific roles in building a shrubby morphology, either by forming a supporting 'trunk' framework or forming branches, rich in EPS (extracellular polymeric substances) and sediment grains. The dendrolites are not internally laminated and grow over stromatolite mats.

According to Suosaari et al. (2018), similar to pinnacle and tufted microbial mats identified in Shark Bay (Flannery and Walter, 2011), the morphology of the dendrolitic features in Hamelin Pool can be attributed to the mobile gliding ability of the microbes. However, unlike the predominantly sediment poor tuft mats, these dendrolitic features are rich in sediment grains and filamentous cyanobacteria are recognised to be better adapted to living in areas with higher sedimentation rates than coccoid cyanobacteria (Grotzinger and Knoll, 1999).

The growth of the dendrolitic structures is ephemeral, both spatially and seasonally, which may reflect fluctuating environmental pressures. These might include seasonal variations in sedimentation rate, water levels, influx of nutrient-rich or alkaline ground water, water temperature, salinity and other chemical parameters (Suosaari et al., 2018). The dendrolites were found only during warmer, late summer months (December to February: 22.3-30.8°C water temperature, Suosaari et al., 2016). It is possible that environmental stress and reduced nutrients may induce the formation of the shrub morphology by competition or collaborative microbial efforts to access nutrients and maintain optimal growth (Petroff et al., 2010). The fact that the dendrolites are not lithifying is attributed to declining calcium carbonate saturation in modern seawater (Grotzinger and Knoll, 1999; Suosaari et al., 2018).

Bradley et al. (2017) describe living (but ephemeral) dendrolitic microbialite cones in two metre-scale geothermal pools, in Little Hot Creek, Long Valley Caldera, California. The partially lithified cm-scale coniform structures with arborescent appearance and

mm-scale protrusions, are composed of intertwined microbial filaments and grains of calcium carbonate. Slightly different microbial communities characterise different parts of the dendrolites and the surrounding laminated mats. The dendrolites are not laminated and were growing over surrounding laminated microbial mats. The pool waters are warm (45.6°C and 34.1°C) and supersaturated with respect to calcium carbonate. The degree of carbonate mineralisation and grain content decreases from the base of the dendrolites to their tips. Measurements of ^{13}C-labeled bicarbonate and rates of autotrophic growth from samples, established that the microbes were actively fixing inorganic carbon in the dendrolitic cone tips and in the microbial mat.

2.5 Stable isotopes and clumped isotopes in the Cotham Marble.

Despite its interesting sedimentology and iconic microbial microfacies the Cotham Marble has attracted relatively little interest from geochemists until the work of Ibarra et al. (2016). This interest was prompted by the discovery of an initial organic carbon isotope excursion (I-CIE) of possible global significance, first observed in the St Audrie's Bay section of the Cotham Member (Hesselbo et al., 2004). The I-CIE has subsequently been used as a marker for the end of the Triassic and its associated mass extinction (Ward et al., 2001; Pálfy et al., 2001), although its origin and significance is now disputed (Fox et al., 2020; 2022; see also Chapter 5).

This background prompted Ibarra et al. (2016) to look for the I-CIE within the organic matter of the Cotham Marble, and they reported values between – 25.8‰ and – 29.6‰ VPDB. They claim these values span most of the range of the St. Audries I- CIE and use this as part of the basis for correlating (stratigraphically) the Cotham Marble with the position of the St. Audrie's I- CIE. In most of their samples (from around Bristol and Charton Bay (Bristol Channel)), the most negative $\delta^{13}C_{org}$ values occurred in the first dendrolitic phase (D1). Limited carbonate stable isotope data (n = 32; four locations) from the Cotham Marble was also presented (Ibarra et al. 2016; Figs. 2.6, 2.7, b) although not much commented on, other than to note the lack of correlation between $\delta^{13}C_{org}$ values and $\delta^{13}C_{carbonate}$. There was also no significant positive correlation between paired carbonate $\delta^{13}C$ and $\delta^{18}O$ that might otherwise have indicated evaporative/restriction effects (Talbot, 1990).

Stable isotope analyses were also made at UEA by Cushing (2018) on the specimen from Wickwar (Lower Woods) in a forerunner of this study. A total of 36 samples with a

resolution of 2 mm were taken through the lower stromatolite (L1, upper 2 cm), the lower dendrolite (D1), the middle stromatolite (L2), and the upper dendrolite, D2 (Figure 2.7, a).

The limited carbonate stable isotope work was the followed up by a few clumped isotope (Δ_{47}) measurements (Petryshyn et al., 2020) performed on the five growth phases of the Cotham Marble from Bristol. Values of carbonate stable isotopes and Δ_{47} temperatures were found to be consistent within growth phases (L and D) and distinguished between facies types. The dendrolitic layers formed at temperature of 13.1 ± 3.6°C (SD), while the laminated layers formed at 29.6 ± 4.7°C (SD), a difference of 16.5°C between layers (Figure 2.8). This difference was, on the face of it, consistent with GCM modelled seasonal palaeotemperatures for the UK end Triassic (July-September mean of 31°C, January-March mean of 14°C).

Critical reassessment of the clumped isotope data in Petryshyn et al. (2020) by Prof. P. Dennis (pers. comm., 2022) has cast significant doubt on the quality of this data, and has in part been an impetus for the present study described in this thesis.

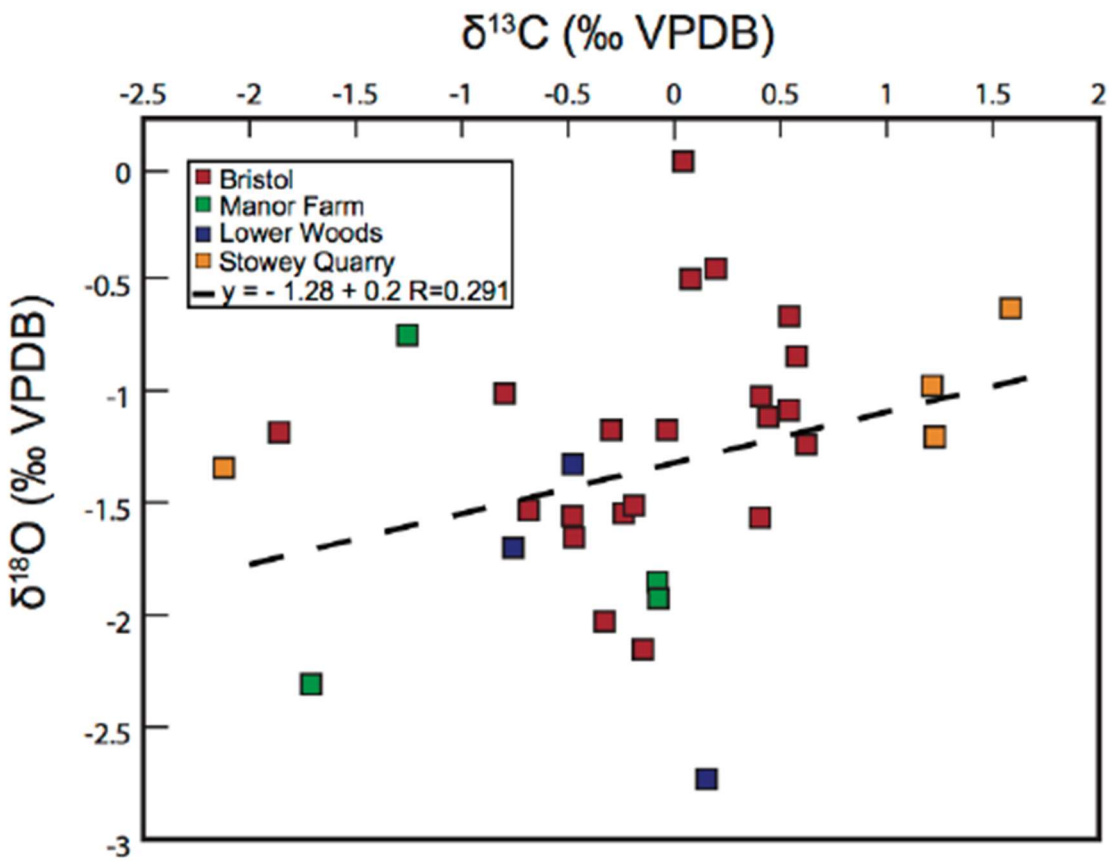

Figure 2.6 Stable carbonate isotope composition in Cotham Marble samples investigated by Ibarra et al., 2016 (Diagram from Ibarra et al., 2016).

Project Results

Sample Number	Microstratigraphy	$\delta^{18}O$ (vpdb)	$\delta^{13}C$ (vpdb)
1	L.L.	-0.97	0.93
2	L.L.	-0.61	0.76
3	L.L.	-1.23	0.07
4	L.L.	-1.14	0.48
5	L.L.	-1.25	-0.13
6	L.L.	-1.80	-0.32
7	L.L.	-1.65	-0.05
8	L.L.	-1.58	0.10
9	L.L. - L.A. Boundary	-1.34	0.46
10	L.A.	-1.44	0.71
11	L.A.	-1.44	0.98
12	L.A.M	-1.79	-0.18
13	L.A.M	-1.02	0.83
14	L.A.	-0.95	0.86
15	L.A.	-0.22	0.99
16	L.A.	-0.25	0.88
17	L.A.	-0.12	0.97
18	M.L.	-0.84	0.66
19	M.L.	-0.69	0.82
20	M.L.	-0.42	0.62
21	M.L.	-0.51	0.40
22	M.L.	-0.57	0.55
23	M.L.	-1.17	0.55
24	M.L.	-1.19	0.72
25	M.L.	-2.00	0.48
26	M.L. - U.A. Boundary	-1.25	0.84
27	U.A.	-0.88	1.26
28	U.A.	-0.93	1.12
29	U.A.	-1.20	0.46
30	U.A.	-1.08	0.47
31	U.A.	-1.83	-0.01
32	U.A.	-1.06	0.95
33	U.A.M.	-1.36	-0.12
34	U.A.M.	-1.25	0.15
35	U.A.M.	-2.13	-0.22
36	V.	-6.09	-4.26

Results of Ibarra *et al.*, 2015

Location	Microstratigraphy	$\delta^{18}O$ (vpdb)	$\delta^{13}C$ (vpdb)
Bristol	L.L.	-1.241	0.621
Bristol	L.L.	-1.015	-0.799
Bristol	L.L.	-1.119	0.442
Bristol	L.L.	-1.176	-0.033
Bristol	L.L.	-0.458	0.195
Bristol	L.L.	0.021	0.041
Bristol	L.L.	-1.185	-1.86
Manor Farm	L.L.	-1.926	-0.077
Lower Woods	L.L.	-1.33	0.477
Stowey Quarry	L.L.	-1.345	-2.122
Bristol	L.A.	-1.548	-0.237
Bristol	L.A.	-2.152	-0.146
Bristol	L.A.	-0.503	0.078
Bristol	L.A.	-1.176	-0.299
Bristol	L.A.	-1.088	0.541
Lower Woods	L.A.	-2.73	0.151
Stowey Quarry	L.A.	1.227	-1.207
Bristol	M.L.	-1.026	0.406
Bristol	M.L.	-1.567	0.402
Bristol	M.L.	-1.532	0.685
Manor Farm	M.L.	-2.308	-1.71
Stowey Quarry	M.L.	-0.633	1.584
Bristol	U.A.	-1.026	0.406
Bristol	U.A.	-1.655	-0.472
Bristol	U.A.	-2.028	-0.328
Bristol	T.L.	-0.847	0.576
Bristol	T.L.	-0.67	0.543
Bristol	T.L.	-1.512	-0.191

Legend	Notation
Lower Laminae	L.L.
Lower Arborescent	L.A.
Lower Arborescent Matrix	L.A.M.
Middle Laminae	M.L.
Upper Arborescent Matrix	U.A.M.
Upper Arborescent	U.A.
Cement Vein	V.
Top Laminae	T.L.

Figure 2.7 Stable carbonate isotope composition in Cotham Marble samples investigated by Cushing (2018) at Wickwar (a) and by Ibarra et al., 2016 (b) (adapted from Cushing, 2018).

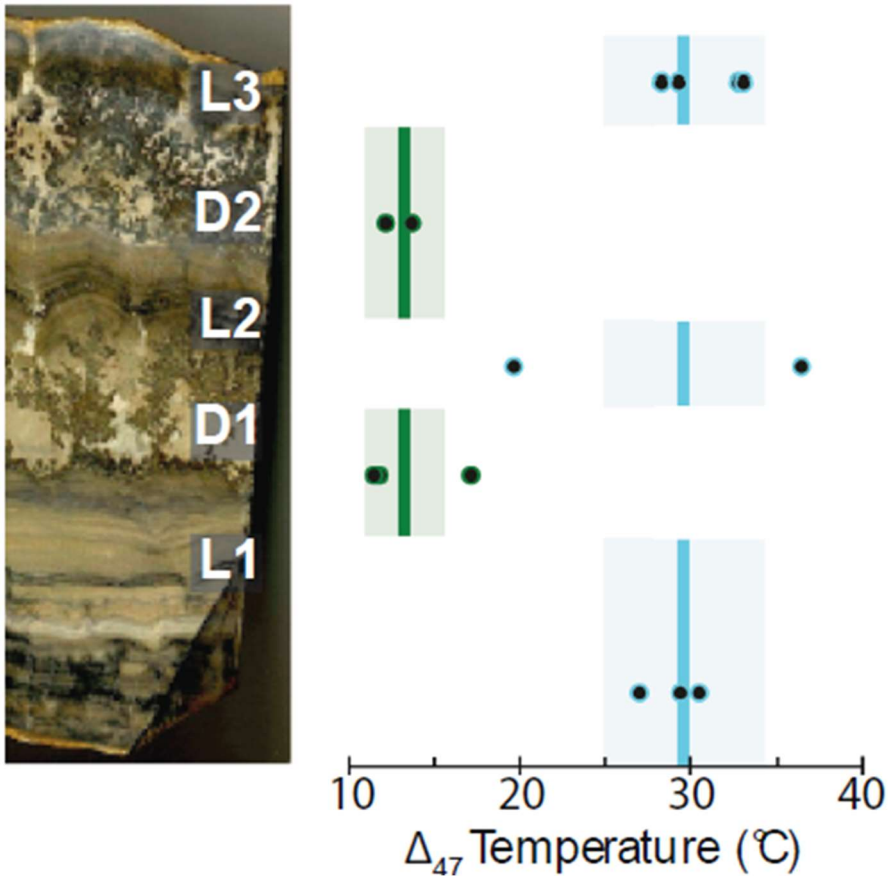

Figure 2.8 Temperature reconstructions from clumped isotope measurements in the respective facies of the Cotham Marble (Figure from Petryshyn et al., 2020).

CHAPTER 3

Materials and Methods

3.1 Introduction

Macroscopic observations were performed on slabbed surfaces cut from the specimen, while microfacies observations were made using thin sections representative of each microfacies identified within the specimen.

Stable carbon and oxygen isotopes and clumped isotopes were measured from a specimen of the Upper Cotham Member, including the Cotham Marble, collected at Wickwar (kindly donated to Prof. J E Andrews by Prof. Paul Wright). The specimen was cut and a slab representative of the various facies was polished to identify where to drill samples.

The description of laboratory processes, calculations and uncertainties in the sections related to the clumped isotope analyses in this chapter was sourced primarily from Paxton (2022) who was undertaking analyses at the same time the CM samples were run.

3.2 Local Stratigraphy of the Sampled Site

The sample was collected at Wickwar, in Gloucestershire, about 23 km northeast of Bristol. The site, also known as Wetmoor and Lower Woods, is one of the localities (Lower Woods) where Cotham Marble was investigated by Ibarra et al. (2014).

The Cotham Marble is Rhaetian (Upper Triassic) in age, found in the Cotham Member, which is part of the Lilstock Formation within the Penarth Group (Chapter 2 and Figure 3.1).

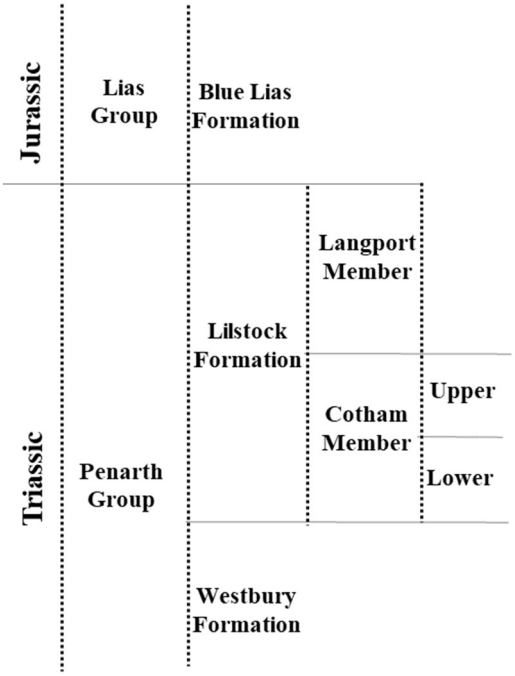

Figure 3.1 Stratigraphy of Upper Triassic.

The area around Wickwar is important for the study of the Cotham Marble, being one of very few places where it can be seen *in situ*. At the site there are good exposures of the Mercia Mudstone Group, and the Penarth Group, including the upper part of the Westbury and Lilstock Formations (Benton et al., 2002). The Cotham Member, exposed in a stream bank, is disconformably overlain by the basal (blue) Lias Group (Benton et al., 2002) indicating that the Langport Member has been locally removed by erosion.

A synthetic stratigraphic section is shown in Figure 3.2 based on information from the hand specimen investigated in this study and from broader descriptions in Benton et al. (2002) who included the stratigraphy of nearby Chase Hill (Richardson, 1904) and a generalised stratigraphy of the Wickwar area.

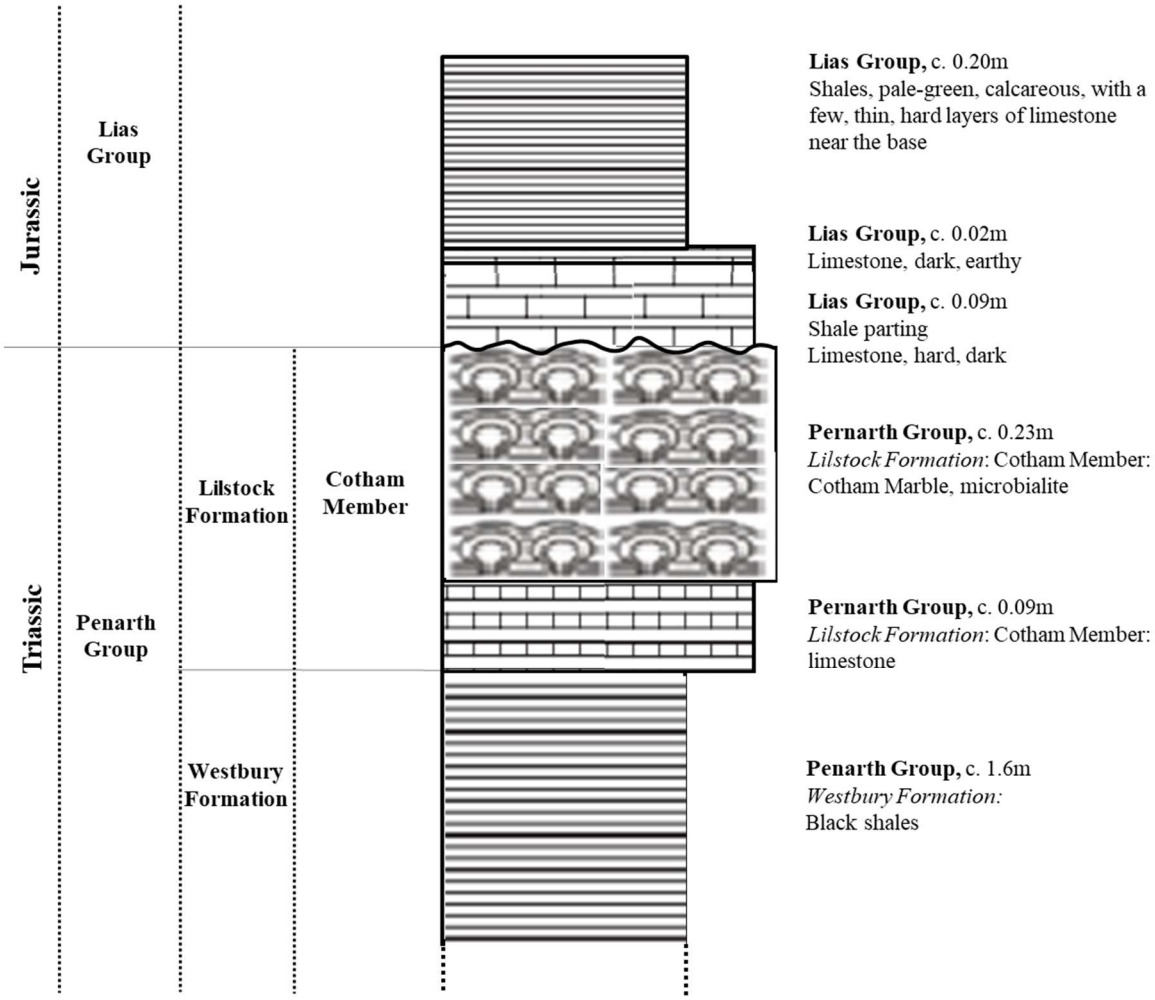

Figure 3.2 Stratigraphical summary of the site of the specimen investigated in this study. The Langport Member, usually present at the top of the Lilstock formation, is absent. The Lias Group directly overlays the Cotham Marble.

3.3 Bulk isotope analyses.

Samples were extracted from cm-long sections of stromatolite laminae and sediment layers along lines at approximately 250 µm up to 500 µm resolution, depending on the morphology of the target features. Samples were also extracted from patches within dendrolites and sediment between dendrolites, darker outer contours and replaced shells. The high resolution of sampling was designed to allow a comprehensive investigation of the facies variability.

Samples were drilled with a New Wave micromill, following pre-set drill patterns. In the case of line patterns, the micromill allows a sampling with a pre-determined distance between the middles of each drilled trace (e.g. 250 µm) and not between the border of traces. The drilled trace width and the volume extracted depends on the geometry of the drill bit and the drilling depth. Usually each drilled trace is much less than 50 µm wide,

therefore although the resolution of sampling is set at 250 µm the distance between drilled traces' borders is less than 250 µm. Powders were stored in foil wraps before analysis.

All bulk isotopic analyses were carried out on the ESIS (Europa Scientific Instrument Services) SIRA (Stable Isotope Ratio Analyser) interfaced to a common acid bath automated carbonate analysis system in the UEA Stable Isotope Laboratory. Approximately 60-120 µg of powder was used for each analysis. The powder was carefully weighed into stainless steel capsules, which were placed in the sample carousel. Reaction with 105% ortho-phosphoric acid was carried out at 90°C with the evolved carbon dioxide dynamically collected via cryodistillation into a cold finger at liquid nitrogen temperature (-196°C) via a water trap held at -100°C by liquid nitrogen. The cooling is controlled by an electronic temperature control system such that liquid nitrogen can be cooled to any temperature down to -196°C.

Mass spectrometric analyses were carried out in the dual inlet mode. Raw δ^{45} and δ^{46} data are Craig corrected for the 17-O contribution and reported as $\delta^{13}C$ and $\delta^{18}O$ with respect to VPDB. The representative precision of the analyses is reported as +/- 1 standard deviation of replicates of the internal standard (UEACMST – UEA Carrara Marble).

3.4 Introduction to clumped isotopes.

The carbonate clumped isotope thermometry concerns measurement of the preferential ordering and abundance of $^{13}C - ^{18}O$ bonds with the temperature of precipitation or recrystallisation of calcium carbonate, compared to the stochastic abundance of the $^{13}C - ^{18}O$ bonds. It is measured by the parameter Δ_{47} (Ghosh et al., 2006) and is expressed by the following equation (Eiler and Schauble, 2004):

$$\Delta_{47} = \left(\frac{R^{47}_{measured}}{R^{47}_{stochastic}} - 1 \right) \times 1000$$

Where $R^{47}_{measured}$ is the measured ratio of mass 47 to mass 44 and $R47_{stochastic}$ is the estimated stochastic ratio and determined using the measured $\delta^{13}C$ and $\delta^{18}O$ values.
Ordering occurs between the carbonate anions in a homogeneous system:

$$Ca\ ^{13}C\ ^{16}O_3 + Ca\ ^{12}C\ ^{18}O\ ^{16}O_2 = Ca\ ^{13}C\ ^{18}O\ ^{16}O_2 + Ca\ ^{12}C\ ^{16}O_3$$

This thermodynamically controlled ordering is independent of the isotopic composition of the ambient water from which the carbonate precipitates. Therefore, temperatures of precipitation can be derived by the sole measurements of Δ_{47}. The relationship between $\delta^{18}O_{CARBONATE}$ and temperature can then be used to calculate $\delta^{18}O_{FLUID}$ using traditional 'Urey' palaeotemperature relationships.

3.5 Clumped isotope analyses.

Clumped isotope analyses were performed on specific microfacies but with a much coarser resolution than bulk isotopes, given the larger mass of powder needed for the measurement. Sample powders of approximately 6 mg were used for each replicate for a total of three replicates in all facies but one, for which two replicates were processed. Samples were either obtained by hand filing samples or by drilling. As temperature and pressure caused by drilling can cause resetting/fractionation of C – O bonds (Eiler, 2011), care was taken to minimise both by gentle slow drilling and filing. Powdered samples were obtained, as far as possible, from areas showing micritic texture within each facies, while avoiding fractures and calcitic veins to prevent contamination from later diagenetic cements. This helps minimise apparent disequilibrium in Δ_{47} values due to nonlinear mixing effects between carbonates of different isotopic values (Defliese and Lohmann, 2015). One sample was obtained from a fracture hosted calcitic vein to help constrain temperatures and isotopic compositions of sparry cement phases.

3.6 Preparation line: Acid digestion and CO_2 purification.

For clumped isotope analyses, carbonate is acid digested to release CO_2 which contains the relevant C-O bonding linked to temperature. Samples are reacted in vacuo at 87°C for 30 min with ca. 105% ortho-phosphoric acid in a common acid bath. Stainless steel capsules with samples are dropped in the acid bath, where a stirrer facilitates acid digestion and dispersal of powder from the capsule. During digestion other gases and water vapour may be released with the CO_2 which may cause mass spectral interference with the cardinal CO_2 masses (44 to 49) in the mass spectrometer leading to erroneous values. Therefore, the gas produced goes through a preparation line to eliminate contaminants and allow pure CO_2 to be measured within the MIRA mass spectrometer.

The gas preparation line has been adapted over time to Improve purification of CO_2 and to capture contaminant gases that were released by the acid digestion of both carbonate and non-carbonate compounds, with the aim of improving results with better replicates

and internal precision. The main components of the preparation line include a vessel for the acid digestion, a series of traps for various contaminants, cold fingers held at different low temperatures by either liquid nitrogen or ethanol and valves to trap the gas at various stages and to allow the pumping of non-condensable gas out of the line (Figure 3.3).

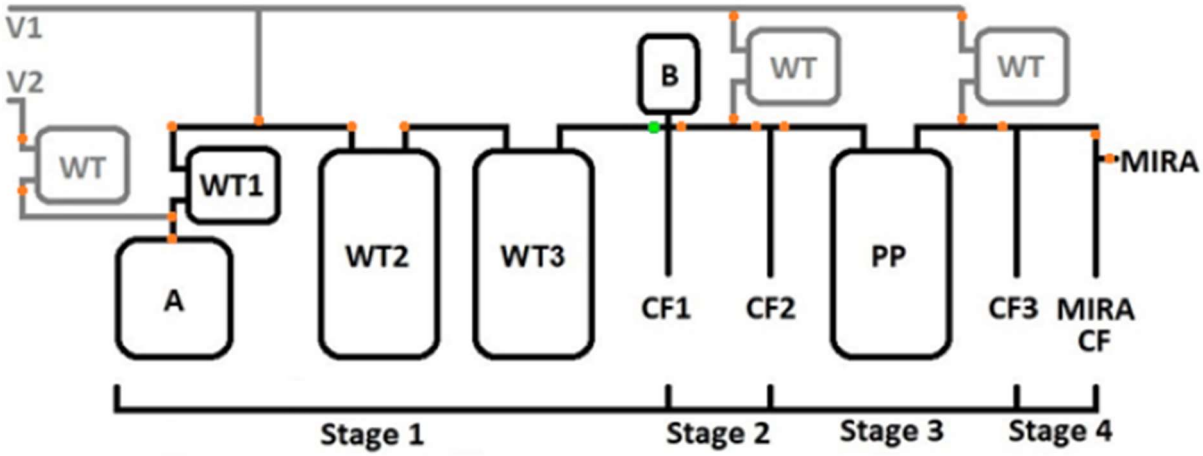

Figure 3.3 Schematic of the preparation line used for clumped isotope analyses. A = common acid bath; WT = water trap; B = Barocel; CF = Cold finger; PP = Porapak Q trap; MIRA = Multi-Isotopologue Ratio Analyser mass spectrometer; V= Vacuum line (From Paxton, 2022).

At the time of the processing of the Cotham Marble samples, the preparation line included four main stages:

Stage 1: in a vessel for the acid bath, about 6 mg (for carbonate-rich samples) is digested at 87°C for 30 minutes; the resulting gas is trapped by liquid nitrogen (LN) in a spiral water trap WT1 immersed in liquid nitrogen at −196°C to allow freezing of CO^2 and water vapour. Non-condensable gases (NC) are pumped through acid vacuum for over a minute, until the pressure gauge indicates that they have been removed.

Stage 2: the gas undergoes 20-minute sublimation from WT1, through WT2 and WT3 into CF1 (Barocel cold finger). The sublimation is obtained by removing the liquid nitrogen from WT1 and replaced with ethanol cooled to -90°C; WT2 and WT3 are held at -115°C. At the end of the process, NC are removed through a valve (V1) while the pressure measured by the barocel indicates their elimination.

Stage 3: the gas is transferred within 5 minutes to a second cold finger (CF2), followed by the removal of NC for 20 seconds.

Stage 4: the gas is transferred for 30 minutes through a Porapak Q trap held below -20°C, frozen with LN into CF3. Upon completion, NC are removed through V2 for 20 seconds. The Porapak Q is a sorbent material which sequesters hydrocarbons.

Stage 5: the gas is transferred within 5 minutes from CF3 to the MIRA cold finger. NC are removed through V2 upon completion for 20 seconds.

Acid is pumped for ~50 minutes between digestion of samples to eliminate 'memory effects' (CO_2 from previous sample) between samples. When the sample is dropped into the acid, some powder spillage towards the walls of the vessel or the dropping carousel can occur; this prevents the full digestion of the sample with consequent reduction of the CO_2 gas needed for a standard measurement and potential cross-contamination with the following sample. Although the system is designed to minimise these spillages, when they occur, the analyses are monitored to observe any anomalous results.

Samples and standards are loaded into the carousel at the end of every day, and the acid is evacuated hot for >1 hour in the evening (with a spinner on) and pumped cold overnight (spinner off). WT1 is heated up to 80°C between samples and overnight.

3.7 The MIRA mass spectrometer.

Clumped isotope measurements are taken on the MIRA (Multi-Isotopologue Ratio Analyser) mass spectrometer, where the sample CO_2 is analysed for δ^{45}-δ^{49}. The MIRA is a dual-inlet isotope ratio mass spectrometer (IRMS) with a 120° magnetic sector and a high sensitivity ion source. The magnetic field strength is monitored and adjusted manually to maintain peak centring at ~8000 volts. Analyses are made at a major beam (m/z = 44) intensity of 7.5×10^{-8} A with simultaneous data acquisition for each cardinal mass of the CO^2 molecule (m/z = 44–49). Each measurement consists of four acquisitions, each of 20 reference–sample gas pairs, with a 20 second integration period for each sample or reference cycle, after a 10 second change over delay time. Before an analysis and between acquisitions, the sample and reference gas volumes and signal strengths are balanced to within 1% of each other. Bulk $\delta^{45} - \delta^{49}$ values of the sample are calculated with respect to the reference gas. $\Delta^{18}O$ (VSMOW), $\delta^{13}C$ (VPDB) and $\Delta_{45\text{-}49}$ are calculated using the calibrated composition of the working reference gas values for $R_{13/12}$, $R_{18/16}$ and $R_{17/16}$ of VPDB and VSMOW. For standard measurement cycles, precision of measured Δ_{47} is ±0.008‰ (Dennis et al., 2014).

3.7.1 Reference gas

The reference gas is produced in the SIL at UEA by reacting the Carrara Marble in an orthophosphoric acid bath at 87°C. The gas obtained is then equilibrated with Norwich tap water (NTW) for over six months before undergoing cleaning through the gas preparation line to obtain purified CO_2. The gas is equilibrated with NTW to produce a reference gas close in bulk isotopic composition to most of the carbonates measured at the SIL and to allow the reference gas to reach a clumped isotope equilibrium at lab temperature (Paxton, 2022). NTW has an oxygen isotopic composition of approximately -7‰ VSMOW, while the CO_2 equilibrated with NTW at 25 °C will have an oxygen isotope composition of approximately +33‰ VSMOW, close to typical marine carbonates (Paxton, 2022).

The reference gas is stored in a 500 mL stainless steel cylinder, which is attached to the MIRA on the reference gas side of the dual inlet. During the majority of the clumped isotope measurements, at the beginning of each working day the reference gas from previous data acquisitions is evacuated and a new small aliquot of reference gas is expanded, via a metering volume, into the reference inlet. Between 15 April and 15 June 2021, one aliquot of reference gas was used for several weeks at a time, held within the mass spectrometer reference bellows. It was discovered, through the examination of the Δ_{49} values of the standards, that during these periods of use the reference gas had become gradually contaminated, thus affecting values of Δ_{47} (P. Dennis, pers. comm. 2021; in Paxton, 2022). The data measured during this period were corrected with an interpolation method. Only a few measurements reported in this study (the calcite vein and the upper laminae of L1 replicas) were acquired during this period and as such were corrected. The majority of samples were measured while changing the reference gas daily.

3.8 Data Processing.

3.8.1 Instrument linearity.

Most mass spectrometers require data to be corrected for ‘non-linearity’, an instrument dependent artefact, for which measured Δ_{47} values differ from true Δ_{47} values with variations in the bulk isotopic composition of δ_{47} (Huntington et al., 2009). Values are corrected by using linear regression of a ‘heated gas line’, composed of different gases of known bulk composition equilibrated at a common temperature, where the measured values of Δ_{47} are plotted against δ_{47} values and the intercept of this line is taken as the true Δ_{47} values.

However, MIRA does not display such linearity issues (Dennis, 2014; Dennis et al., 2014) and, therefore, no correction for non-linearity was required for the clumped isotope data in this study.

3.8.2 Acid fractionation Δ_{47} correction.

The reporting of Δ_{47} data is based on acid digestion at 25°C. Therefore, a correction factor has to be applied to Δ_{47} values obtained by reaction at different temperatures. In accordance with Guo et al. (2009), a 1°C change in temperature from 25°C is equivalent to 0.001‰ difference in Δ_{47} and therefore the Δ_{47} of a sample acid digested at 87°C should have a difference of -0.062‰ compared to the value measured at 25°C. An offset of 0.062‰ was obtained from measurements of samples at UEA using both offline reaction at 25°C and online reaction at 87°C, which demonstrates an excellent agreement with the theoretical acid fractionation reported by Guo et al. (2009).

Therefore, for acid digestion at 87°C, a correction factor of 0.062‰ is added to the Δ_{47} values of each sample.

$\Delta_{47}(\text{CDES@25}) = \Delta_{47}(\text{CDES@87}) + 0.062‰$

where CDES is the Carbon Dioxide Equilibrium Scale.

3.8.3 Δ_{47} standardisation.

There are lab specific mass spectrometric artefacts arising from processes such as scrambling in the ion source that require Δ_{47} raw data conversion in order to ensure that reported data are comparable between labs (Dennis et al., 2011). Raw Δ_{47} values, named Δ_{47} (LRF)' for 'local reference frame', are converted to the carbon dioxide equilibrium scale of Bernasconi et al. (2018), named 'Δ_{47} (CDES-25)'. CDES-25 stands for Carbon Dioxide Equilibrium Scale reference frame and refers to an acid digestion temperature of 25°C. A correction is required for Δ_{47} values when digestion takes place at different temperatures, as it is discussed in 3.8.2.

For the conversion, an empirical transfer function is created in each lab using a set of common carbonate standards (Bernasconi et al., 2018). The Δ_{47} (CDES-25) transfer functions are created by projecting Δ_{47} (LRF) measurements of ETH1 and ETH3 carbonate standards (Bernasconi et al., 2018) and the UEA Carrara Marble standard (UEACMST), against the UEA derived 'Δ_{47} (CDES@87)' values of the same standards.

Transfer functions are calculated from acid digestion of standards at 87°C and therefore a correction is performed to allow comparison of data at 25°C, as discussed in 3.8.2.

An example of a transfer function used during the processing of data is:
Δ_{47} (CDES@87) = 1.1867× Δ_{47} (*L*RF@87) + 0.8105

The UEA empirically derived Δ_{47} (CDES@87) values of the standards used are as follows:

- ETH1 = 0.218‰
- ETH3 = 0.613‰.
- UEACMST = 0.322‰

The above values were measured at an acid digestion temperature of 25°C against a suite of heated gasses and corrected to represent reaction at 87°C using the UEA empirically derived acid fractionation correction value (-0.062‰; see Section 3.8.2) for comparison with Δ_{47} (LRF@87) values.

UEA derived ETH values are close to those provided by a recent interlaboratory comparison (Bernasconi et al., 2021). The difference between the ETH Δ_{47} (CDES-90) values in Bernasconi et al. (2021) and Δ_{47} values derived at UEA and corrected for reaction at 90°C is lower than measurement precision for samples between 0-100°C.

Transfer functions are not constant and were calculated for several time periods when data was collected. As such several transfer functions were used to derived data in this study.

The standards ETH1, ETH2, ETH4, ETH3 are carbonates precipitated or modified in laboratory, while UEACMST is Carrara Marble: these standards have significantly different precipitation temperatures. Measurements of ETH2 and ETH4 were also used to monitor instrument linearity, and data show that linearity was maintained throughout the duration of analysis (P. Dennis, pers. comm. 2018; in Paxton, 2022).

3.8.4 Temperature calculation.

The carbonate formation temperature of each sample is calculated using an equation that was empirically derived at UEA (Kirk, 2017; Dennis et al., 2019):

$$\Delta_{47}(CDES\ @25) = (0.0389\times10^6)/T^2 + 0.2139 \qquad \text{Equation (3.1)}$$

Where T = Temperature (Kelvin).

3.8.5 $\delta^{18}O_{CARBONATE}$ derivation.

In addition to Δ_{47}, MIRA provides a value of the $\delta^{18}O_{(VSMOW)}$ of the analysed CO_2 gas that can be converted in $\delta^{18}O_{CARBONATE(VSMOW)}$ using the following equation:

$$\delta^{18}O_{CARBONATE(VSMOW)} = (1000 \times \delta^{18}O_{CO2\,(VSMOW)})/1.0084 - 1000$$

where the constant 1.0084 is the acid fractionation factor (Swart et al., 1991), which corrects for the fractionation caused by the conversion of the carbonate sample into CO_2 at 87°C.

To allow comparison with published data, The $\delta^{18}O_{CARBONATE}$ values are converted with respect to VPDB with the following equation:

$$\delta^{18}O_{(VPDB)} = (\delta^{18}O_{(VSMOW)} - 30.86)/1.03086$$

3.8.6 $\delta^{18}O_{FLUID}$ derivation.

Using the calculated values of T (K) and $\delta^{18}O_{CARBONATE}$, it is possible to calculate an approximation of the original oxygen isotopic composition of the fluid from which the carbonate precipitated. The equation of Kim and O'Neil (1997) was chosen for calcite samples, as it is appropriate for inorganic calcite:

$$1000 \ln \alpha_{CARBONATE\text{-}FLUID} = 18.03(10^3\,T^{-1}) - 32.42$$

where T is in Kelvin.

$$\alpha_{CARBONATE\text{-}FLUID} = (\delta^{18}O_{CARBONATE(VSMOW)} + 1000)/(\delta^{18}O_{FLUID(VSMOW)} + 1000)$$

3.8.7 Additional corrections: Reference gas corrections.

As mentioned in section 3.7.1, between 15/04/21 and 15/06/21, a test was run to investigate the effects of using the same aliquot of gas over periods of time between 4 and 14 days, instead of replacing the reference gas in the mass spectrometer each day. It was observed that an incremental contamination of the reference gas affected masses 47-49 and resulted in a depletion of Δ_{47} over time for any sample and standard.

The daily measurements of the standards UEACMST, ETH1 and ETH3 allowed the observation of the linear trend of Δ_{47} depletion. Δ_{47} (LRF) of the standards were plotted against the time lapsed (n_{days}) of measurements since the replacement of gas reference to determine the gradients for the depletion trends. A correction factor was created, using an average of the gradients for the standards, and applied to all samples and standards measured during the tests:

Δ_{47} (LRF corrected) = Δ_{47} (LRF uncorrected) + (n_{days} x 0.00907)

The corrected results show closer values to measurements undertaken while replacing the reference gas daily.

The Δ_{47} (LFR corrected) values for standards were subsequently used to create the Δ_{47} (CDES-25) transfer function for this period.

3.8.8 General data uncertainties.

It can be assumed that each measurement may be affected by operator-induced changes in preparation, as well as differences in performance of the components of the preparation line and in performance of the mass spectrometer itself. These differences may occur within one day of measurements or more likely and to a greater extent between different days.

To account for uncertainties and variabilities, usually labs report measurements as standard deviation or standard error. Excluding no cumulative and/or systematic biases (usually depicted as cumulative contamination of reference gas, where a trend of increasing or decreasing results might be observed), data from many repetitions of measurements of the same sample might be expected to produce a normal distribution around a mean value, for which the standard deviation would be a reliable representation of variability, including sample heterogeneity and any non-systematic measurement differences.

Clumped isotope analyses require several hours to prepare and run a single measurement, and therefore many repeat analyses are not feasible. The number of repetitions of measurements for each sample is usually limited to 3, and 3 repetitions are likely not to represent the true mean or distribution of the sample; therefore, the standard deviation may misrepresent the true uncertainty of the data (Fernandez et al., 2017).

A more reliable representation of uncertainty and repeatability, the pooled standard deviation (s_{pooled}) of samples of similar composition was calculated for $\delta^{13}C$, $\delta^{18}O_{CARBONATE}$ and Δ_{47} measurements. This parameter represents the spread of the standard deviations of different groups from the same population and can be applied to repeated analyses as low as 2.

$$S_{pooled} = \sqrt{\frac{(n_1-1)s_1^2+(n_2-1)s_2^2+\cdots+(n_k-1)s_k^2}{n_1+n_2+\cdots+n_k-k}}$$

where n_x is the number of measurements made for sample x; s_x is the standard deviation of the repeated measurements of sample x; and k is the total number of samples.

This method was used to estimate the reproducibility of similar samples and to track the long-term reproducibility within the lab. For example, the pooled standard deviation of the three standards, UEACMST, ETH1 and ETH3, provides an indication of the reproducibility over long time periods. Standard deviation of standards calculated in specific time periods can also be used to monitor repeatability.

3.8.9 Sample derived contamination.

Samples release contaminant gases in addition to CO_2 during acid digestion. If not removed, when entering the mass spectrometer, contamination can affect measurements of Δ_{47} because of isobaric interferences at the cardinal masses of the CO_2 isotopologues, particularly pronounced at mass 47 (Eiler and Schauble, 2004).

The preparation line is designed to remove common contaminant gases, such as water vapour, hydrocarbons, halocarbons, etc. However, samples particularly rich in compounds other than carbonate, such as organic matter and clay minerals, may release contaminants that may not be captured in the preparation line. At UEA, measurements of Δ_{48}, and occasionally Δ_{49}, are used to distinguish contaminated samples from non-contaminated ones. Δ_{48} in particular is sensitive to the presence of contaminant gases (Eiler and Schauble, 2004; Huntington et al., 2009).

Samples from the Cotham Marble are not particularly rich in organic matter or other non-carbonate compounds, and therefore the presence of these types of contaminants is likely to be very low. Furthermore, measurements were carried out after May 2021, after issues with water vapour had been identified and resolved.

3.8.10 Limitations with clumped isotope analysis.

Data processing and comparisons between labs.

It is important to know the limitations of the methodology used in clumped isotope data processing especially when comparing data from different labs.

One source of uncertainty is the calibration of Δ_{47} measurements to the CDES-25 reference frame to allow data to be comparable between labs. Since Δ_{47}(CDES-25) is

related to an acid digestion at 25°C, a correction is required when the digestion temperature is different. The acid reaction correction factor varies in the literature and therefore different corrections are applied for the same digestion temperature between studies. These variations in data processing calculations can affect the comparability of reported results. The correction factor used at UEA, as described in section 3.8.2, was derived empirically within the lab but is also in agreement the theoretical fractionation relationship determined by Guo et al. (2009).

Another source of uncertainty for data comparison comes from the calculation of the carbonate formation temperature from Δ_{47} (Equation 3.1 – section 3.8.4). A variety of temperature equations are used by different workers to determine the formation temperature of a carbonate, which in turn affects the calculation of the corresponding $\delta^{18}O_{FLUID}$. Therefore, even if the results have identical Δ_{47} (CDES-25) values, the calculated temperatures may be different. Such differences can be in the range of several degrees: as an extreme example, the same Δ_{47} value would determine a temperature of 24.1°C if calculated using Equation 3.1 (Kirk, 2017; Dennis et al., 2019) and a temperature of 39.8°C if calculated using Equation 9 of Dennis et al. (2011).

The UEA temperature equation (Section 3.8.4) is within measurement uncertainties identical to the calibration of Anderson et al. (2021), which was calibrated to carbonate standards and was in agreement with several other studies. As such, the use of the UEA temperature equation is justified as its similarity of formulation and results with other labs gives confidence on the consistency of the results.

CHAPTER 4

Results

4.1 Description of the Wickwar Upper Cotham Member.

The specimen examined in this study is a limestone collected from the Upper Cotham Member at Wickwar, a locality about 20 km NE of Bristol. The sample is about 20-25 cm thick and in its upper 16-20 cm comprises the Cotham Marble with three laminated layers (L1, L2 and L3) and two dendrolitic layers (D1 and D2) (Figure 4.1, a), broadly similar to the specimens described by Wright and Mayall (1981) and Ibarra et al. (2014). In its lower 5-6 cm the sample contains the limestone layers below the Cotham Marble proper (Figure 4.1), layers that have not typically been described by others.

In the following section I describe meso- and micro-features in the Wickwar sample concentrating on those that largely have not been described by previous authors (layers below L1) or have been described differently.

4.1.1 Limestone microfacies below layer L1 of the Cotham Marble.

The limestone layers below the Cotham Marble proper are about 5-6 cm thick in two main layers (Figures 4.1, b; 4.2). The top layer, 5-10 mm thick, underlying L1 of the Cotham Marble is composed of grey-olive green micrites with thrombolitic fabrics (Figure 4.2, a). Beneath this there is a layer of laminated sediments (mbt in Figure 4.1b) (Figure 4.2, b) grading into layers of disarticulated, thin shells in a fine micritic matrix (Figures 4.2, c, d) (SLb in sections 4.3.1 and 5.2.1; Figure 4.9), adjacent to and underlain by more massive grey micritic layers (Figures 4.1, b) (SLc in sections 4.3.1 and 5.2.1; Figure 4.9). A further micritic layer with abundance of shells close the sequence of the Upper Cotham Member in the specimen (SLa in sections 4.3.1 and 5.2.1; Figure 4.9).

The thrombolite textures appear to be patches embedded in a fine grey micritic sediment (Figures 4.1 b, and 4.2, a). The thrombolites may be in growth position, but it is equally possible they are fragments deposited within the micritic matrix (Figures 4.3, a, b). In thin section the thrombolites contain darker areas, corresponding in hand specimen to

olive green patches, while more peloidal textures correspond in hand specimen to lighter green patches; light green areas in hand sample are largely micritic matrix (Figures 4.3, a, b).

The top of the thrombolitic layer appears undulose (probably eroded), and the boundary is emphasised by a dark, stylolitic, seam caused by burial pressure-dissolution (Figure 4.2, a). This upper contact is in places barely distinguishable from the overlying L1 fabrics, whereas in other places it is overlain by a very thin layer of fine grey micritic sediment which may thicken into small pillows (mat in Figure 4.1b).

a b

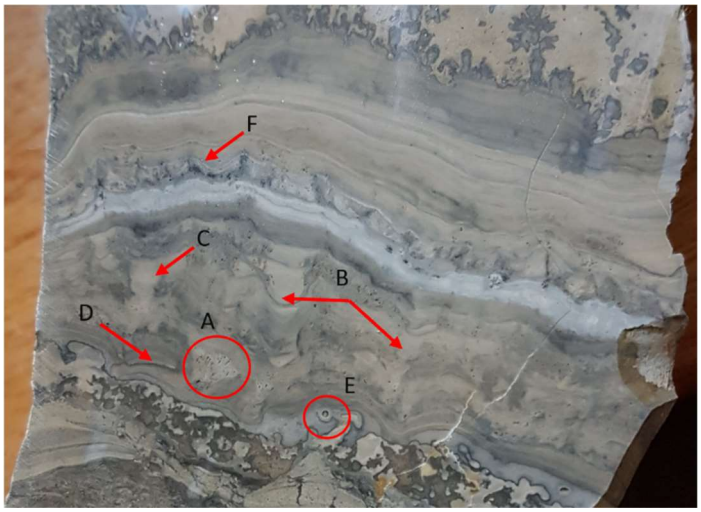

c

Figure 4.1 a) The facies of the Upper Cotham Member in the specimen from Wickwar (b); detail of the lower unit of the facies of the Upper Cotham Member underlaying the first stromatolite phase, L1, of the Cotham Marble; L1 gl: grey set of laminae in L1; mat: micritic layer above thrombolites; mbt: micritic layer below thrombolites; blue bar is 1 cm; (c) close up of L1, with (A) possible bubbles, (B) bioturbation or loading structures, (C) bioturbation, (D) desiccation surface, (E) *Microtubus communis*, (F) tufts.

The sediment layer (mbt) between the thrombolite and the shelly layer appears laminated with grey to grey-blue colours (Figures 4.2, b, c; and 4.3, a). The laminae appear depositional (mechanical) rather than microbial and dark grains of pyrite are common.

The underlying shelly layer (SLa in sections 4.3.1 and 5.2.1) has a distinct light-grey to grey-blue colour compared to the grey colour of the overlying lamina, but the transition upward is gradational (Figures 4.2, c, d). The shells, from about 3 up to 10 mm long, could belong either to ostracods, such as *Darwinula* spp., or small bivalves, although according to Swift and Martill (1999), *Darwinula liassica* present in the Penarth Group are 0.6-0.1 mm, therefore, smaller than in the specimen. Given the abundance of sub-horizontal, disarticulated shells, the shelly horizon may be a storm deposited lag around and through which, micritic sediment has infiltrated (Figures 4.3, c, d). A few of the shells remain articulated and there are traces of gastropod shells. It is likely that the shells mainly belong to the same species (Figures 4.3, c, d), suggesting a low diversity fauna.

In thin section the original shell carbonate is replaced by a sparry calcite cement, which usually indicates the shells were originally composed of aragonite (e.g. Scoffin 1987, Figure 9.19), more soluble than the encasing calcitic matrix (Figures 4.3, c, d). In the shelter cavities of articulated shells, the original open space includes micritic ‘floor deposits’ followed by a sparitic pore-filling cement with drusy texture (Figures 4.3, c, d).

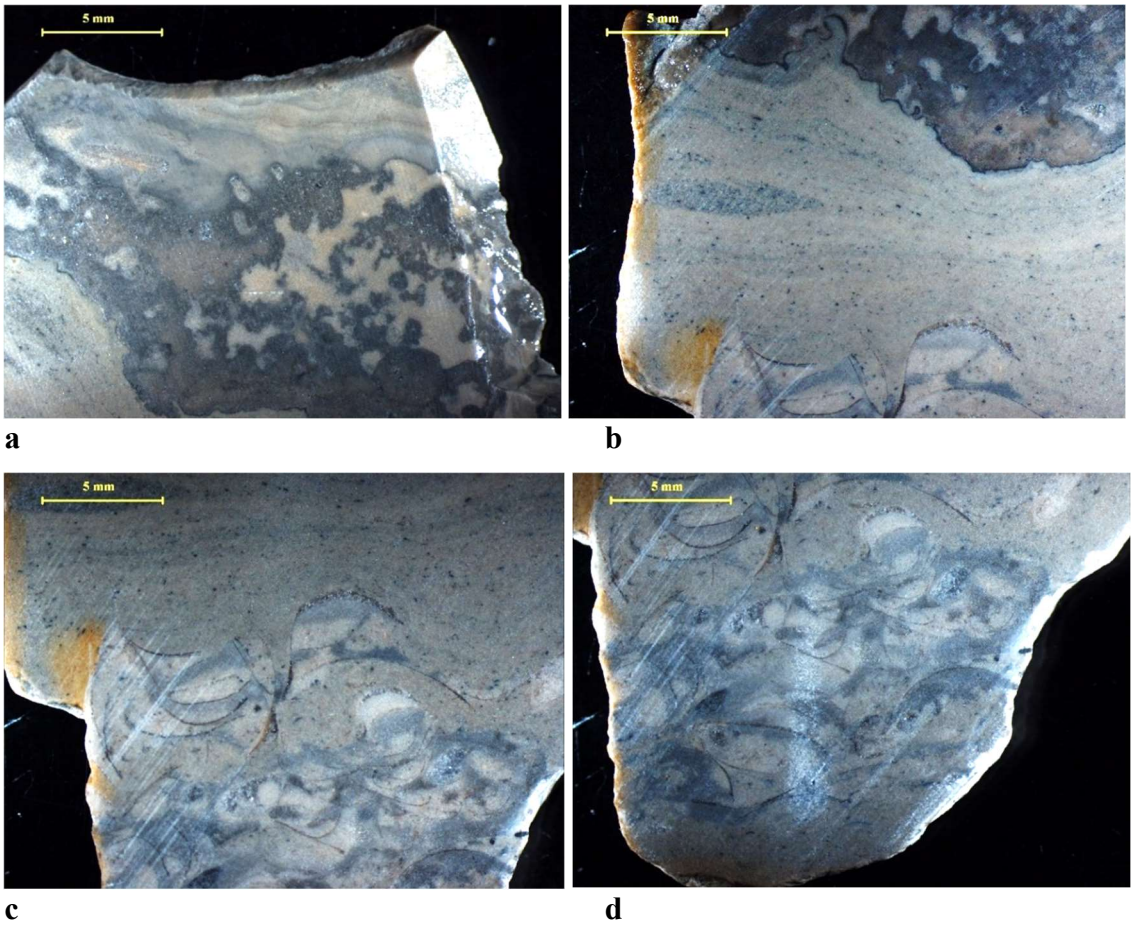

Figure 4.2 Lower facies of the Upper Cotham Member: thrombolite layer (a); thrombolite with laminated sediment layer (b); (c) and (d) Layered Shell lag interspersed with micritic sediment levels in the lower part of the specimen.

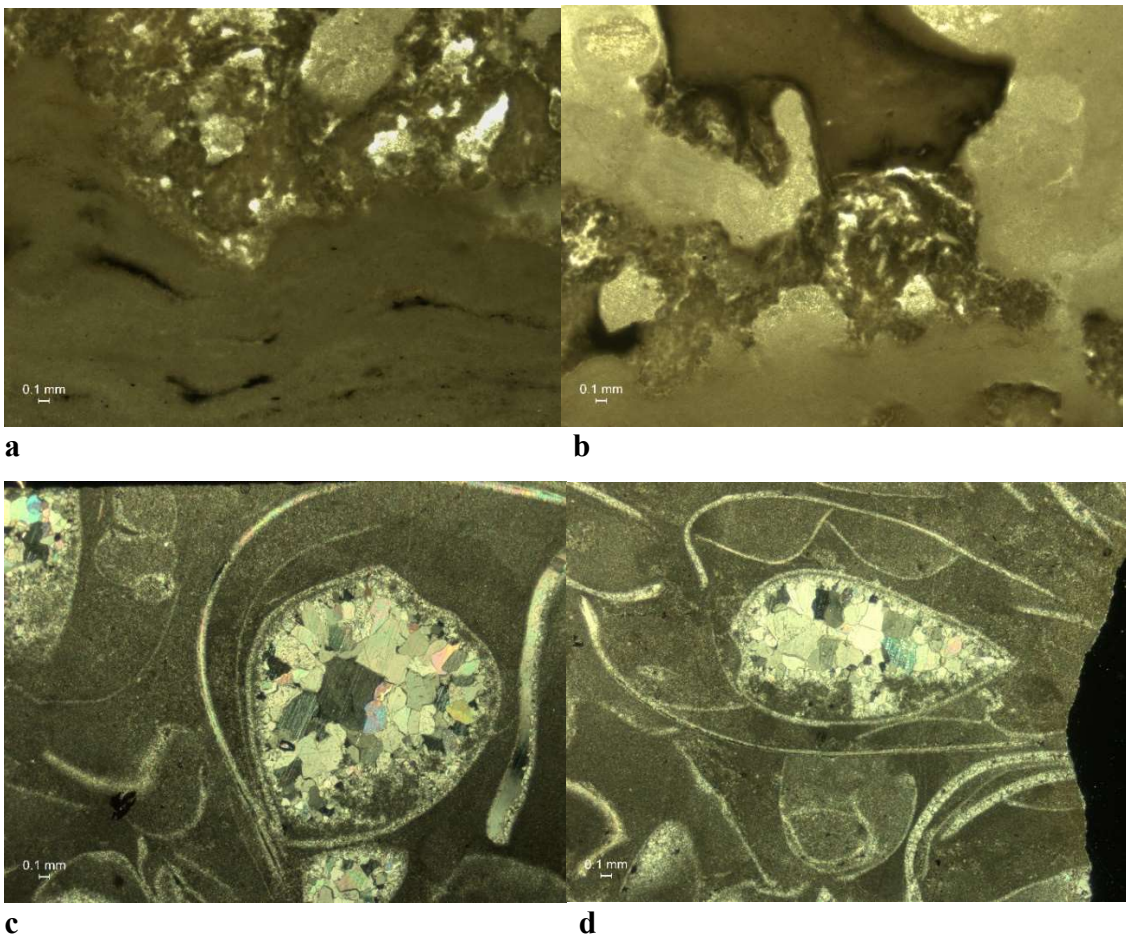

Figure 4.3 Photomicrographs of the Upper Cotham Member below the Cotham Marble: contact of thrombolite with laminated micritic sediment with inclusion of possible dark pyrite grains (a); thrombolite texture (b); micritic layer with shells (c, d).

4.1.2 Cotham Marble facies.

The fabrics and microfacies of the Cotham Marble have been described by previous authors (Chapter 2) and broadly apply to the main L and D fabrics seen in the Wickwar sample. Here I emphasise obvious differences or points of detail.

1- The first laminated phase (L1) features mainly subparallel laminae, which can be subdivided by the presence of blue-grey laminae in a lower set of subparallel laminae, and an upper set of almost horizontal laminae. In the lower set, the laminae seem to have been disturbed by syndepositional deformation, probably due to bioturbation, bubbles, loading, and desiccation, which disrupted their continuity (see Figure 4.1, c, for evidence of these structures). At the base of this lower unit there are rounded features that may be *Microtubus communis*. Above the regular blue-grey laminae there are small darker features a few millimetres in size, and similar to tufts, which can interrupt the regularity of laminae. Above

this, brown laminae appear very regular throughout the upper part of L1 (Figure 4.1, c).

2 - The lower dendrolites (D1) occur abruptly on the L1 stromatolites in the shape of small, rounded lobes, or hedges, of dimensions of a few millimetres. D1 is composed of dark dendrolitic structures with even darker outer edges that abut the surrounding laminated fine sediment fill. These concave laminae appear draped between the dendrolite structures, presumably banked against the dendrolitic 'highs'. The tops of the dendrolites are about 1-2 cm higher than the fill.

3 - In thin section the texture of the hedges, small tuft-like structures growing above the L1 laminae, shows accretions of mm-scale sparitic pillow-like areas (Figure 4.4, a).

4 - The laminae of L2 drape over the top of the D1 dendrolites with a near constant thickness that is inherited from the relief (synoptic relief) of the underlying dendrolites. As such, although they appear subparallel and regular, these laminae are not horizontal. Their shape is characterised by depressions, that in some cases present as an interruption of laminae; the interruption spaces are filled by sediment, similar to the fill of the inter-dendrolite areas.

5 - The upper dendrolites, D2, are formed of darker micrites within a matrix of fine grey sediment, largely as in D1. The contact with the underlining stromatolite laminae is distinct and abrupt. Unlike D1, the massive dendrolites do not evolve from hedges, but appear separated fom ther upper surface of L2 by a fine sediment cemented by microspar with irregular contacts with the underlying L2 laminae (Figure 4.4, c, d).

6 - Small scours are present in the upper surface of L2 (Figure 4.4, c, d). Moreover, unlike the arborescent shape of the dendrolites in D1, the base of D2 is characterised by an initial 'cloud' of dendrolite masses similar to shrubs (ribbon-like texture in Figure 4.4, c, d), above which, discrete dendrolite structures develop separated by fine sediment fill (Figure 4.5). The relief of the dendrolites over the fill is smaller than in D2, up to 1 cm.

7 - In places, the dendrolites appear to be made of ribbon-like microbial laminae, which can form convoluted lumps (Figure 4.4, b). Another common dendrolite and stromatolite lamina texture seen in thin section is layers of peloidal grains, e.g. laminae in L2 (Figure 4.4, b).

8 – In the upper dendrolites, there are clear stylolites partially cemented by pyrite which are sub-vertical and largely aligned with fractures that host vein calcites.

9 – In general, there is a low presence of *Microtubus communis*, as noted by Ibarra et al. (2014) although rounded features that may be *Microtubus communis* appear at the base of L1 (Figure 4.1b). Several regular rounded features appear in thin sections amongst the ribbon-like texture of the lower dendrolite shrubs in D2 (Figure 4.4, c, d).

10 – The laminae of L3 grow abruptly, draping the top of D2 dendrolites in a subparallel manner, resulting in a consistently thick layer that inherit the relief of the dendrolites underneath (as observed in L2).

4.1.3 General observations.

- In thin sections stained with combined Alizarin red S and potassium ferricyanide, all micrites and microspars have red colour, indicating that the calcites are depleted in Fe. Some spars show slight mauve coloration indicating a slight increase in Fe content, but even late spars in fractures are not strongly ferroan.

- Cathodoluminescence (CL) shows that late spars in veins and filling large areas of void space (including aragonite fossil moulds) have a dull brown CL colour and may be co-eval. All micrites have bright orange luminescence as do micrite fills, similar to Jurassic stromatolites discussed by Andrews (1986).

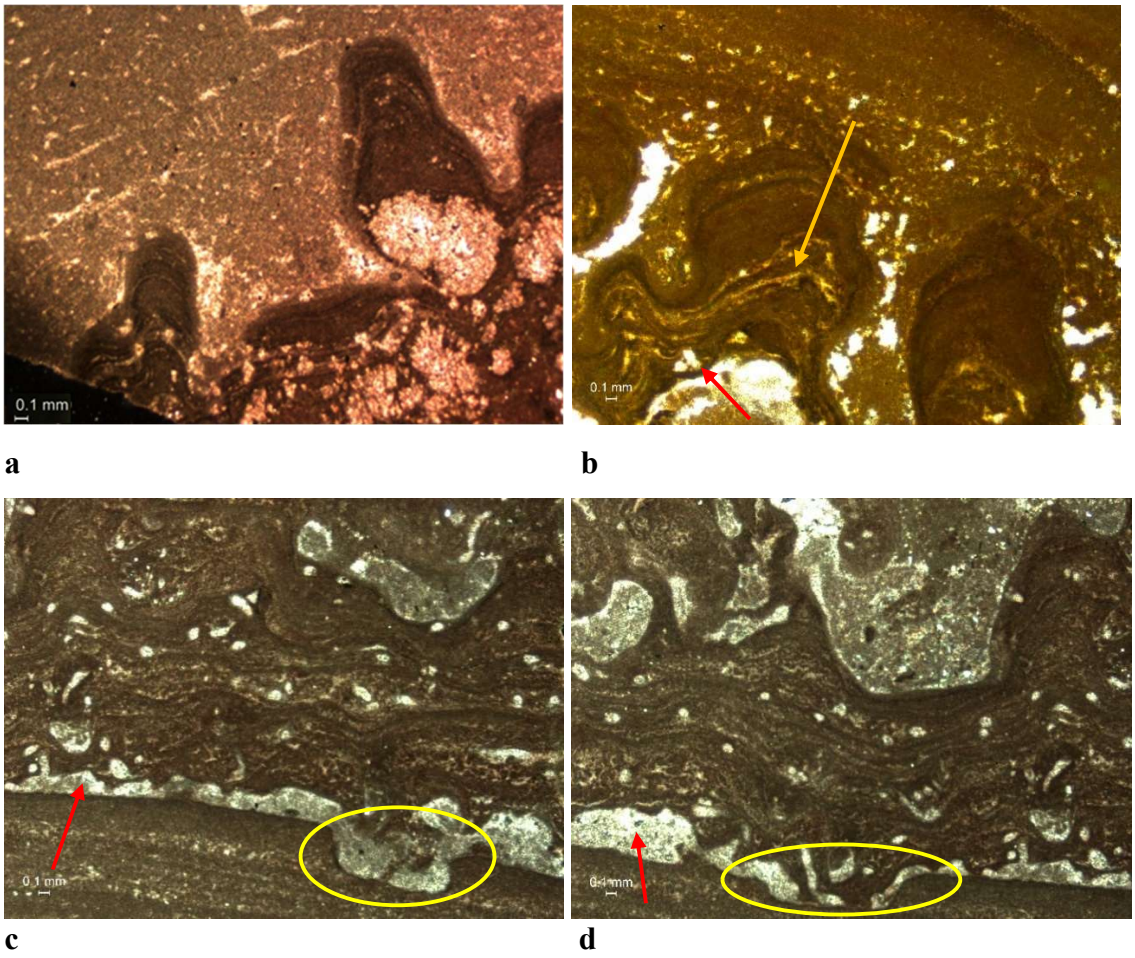

Figure 4.4 Photomicrographs of stained thin section of D1: hedges with spherulitic sparitic pillow-like fabric (red arrows) (a); upper contact of D1 dendrolites with base laminae of L2, with ribbon-like texture of dendrolites (red arrow) and rounded features that may be evidence of *Microtubus communis* (yellow arrow) (b); ribbon-like texture of dendrolites in D2 with rounded features that may be *Microtubus communis*; the top of L2 laminae appears scoured (yellow oval circles in c, d); sediment fill separates the D2 dendrolites from the base of L2 (red arrows in c, d).

- Millimetre-scale microdigitate structures are present in both L2 and L3. The macroscopic appearance is that of small burrows or depressions (Figure 4.5). In both L2 and L3, these depressions seem to form below a single specific lamina which appears darker than the surrounding laminae (Figure 4.5).

- In thin section, some laminae appear to bend around former empty spaces now filled by sparry calcite cement. In other places the voids appear to cut through laminae (Figure 4.6) and, in other cases, open tubes are more complex and bend inside laminae as small tunnels (Figures 4.6, b, c, f).

- The presence of distinct surfaces is particularly evident in L3, where there is peloidal debris in some depressions (Figure 4.6, d-f) and the sediment of the laminae overlaying these structures appears coarser with a ‘weathered/altered’ peloidal texture compared to the finer texture of the laminae below; pockets of debris contain coarser sediment and shell fragments (Figures 4.6, b-f). The top of L3 also has a further level of small tube-like narrow depressions, a few millimetres above the first level. These depressions are filled with coarser grains and biogenic fragments. The sediment above these burrows has a lighter colour and may be microsparitic muddy/silty matrix (Figure 4.7, a, b).

Figure 4.5 From base to top, phases D1, L2, D2 and L3 with subvertical interdigitate structures in both L2 and L3. The base of D2 is characterised by an initial 'cloud' of dendrolite masses similar to shrubs (red circle) (e.g. see ribbon-like texture in Figure 4.4, c, d), above which, discrete dendrolite structures develop separated by fine sediment fill.

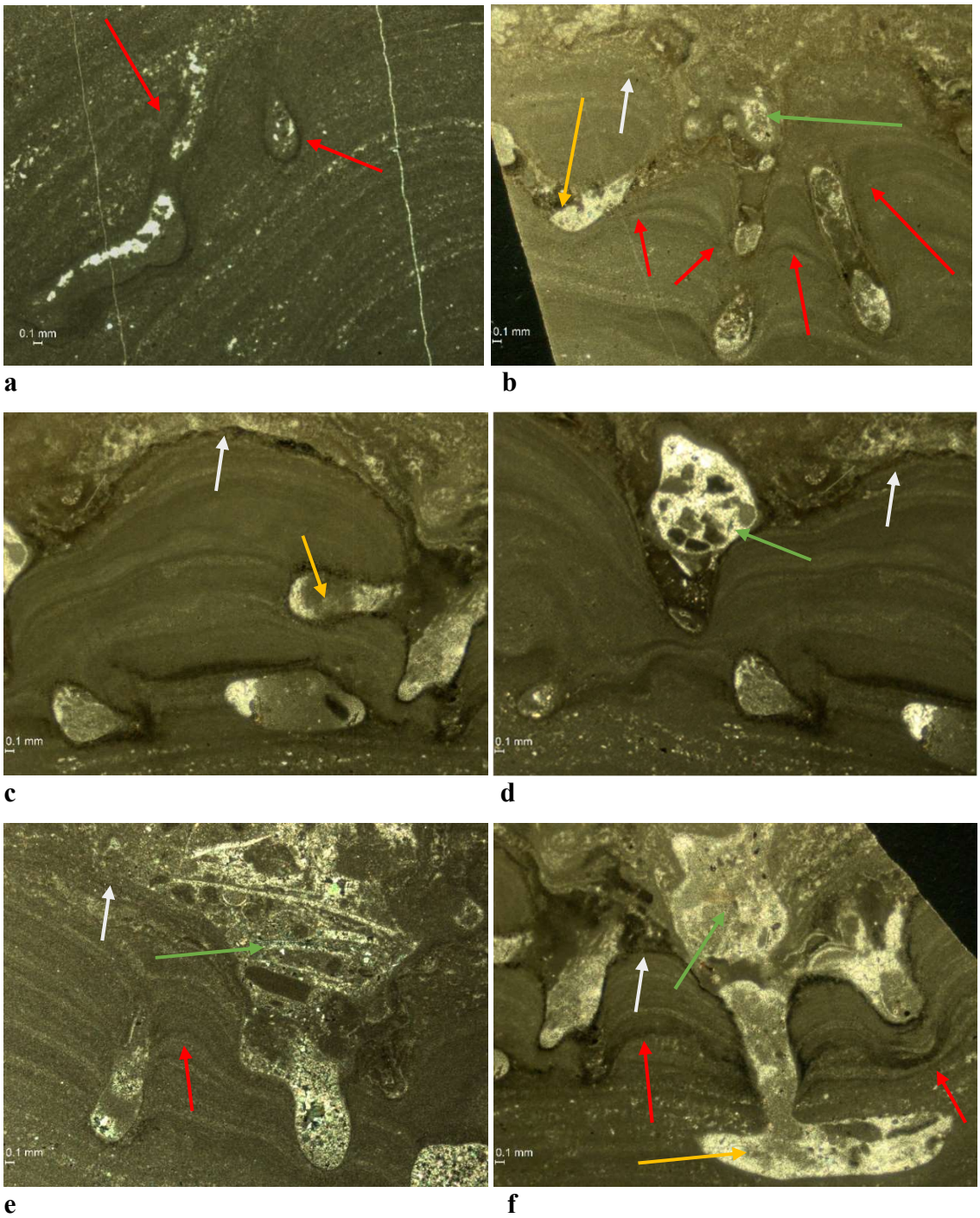

Figure 4.6 Photomicrographs of microdigitate/depression structures in stromatolite laminae of L2 (a) and L3 (b-f); (a) arrows show that laminae are cut through from void spaces and not bent; (b), I, (f) red arrows point to laminae bent and cut through from void spaces; yellow arrow points to a tunnel-like void space; (b), (c), (f) yellow arrows show tunnel-like void spaces; (b), (d) I, (f) green arrows show pockets of debris; (b-f) white arrows indicate surfaces separating overlaying laminae with a 'weathered/altered' peloidal texture compared to the finer texture of the laminae below.

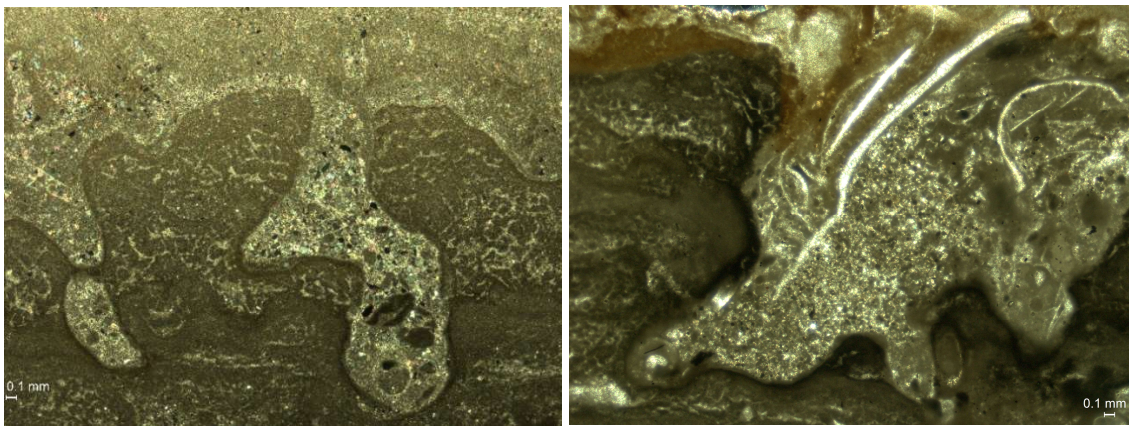

a **b**

Figure 4.7 Photomicrographs of depression structures filled with debris of coarser grains and biogenic fragments at the top of stromatolite laminae in L3 (a, b).

4.2 Clumped isotope measurements

The clumped isotope measurements were performed on sixteen samples on the major mesostructures of the specimen from Wickwar: laminar stromatolites L1, L2 and L3, dendrolite structures and the micritic fills of D1 and D2, micritic layers underlying L1 including the thrombolite and shelly layers, and a sparry calcite vein that crosscuts (postdates) the depositional layers (Figure 4.8 and Table 4.1).

For the base, the micritic layer below the shelly horizon has a Δ_{47}-derived temperature of 8 ± 4.7°C and a persistent grey layer below the thrombolite has a Δ_{47}-derived temperature of 11.5 ± 4.7°C. The olive green thrombolites formed at Δ_{47}-derived temperature of 9.4 ± 4.7°C and a thin grey layer above the thrombolites at 4.4 ± 5.8°C.

Three areas of the lower stromatolites (L1) were measured. The lower laminae formed at a Δ_{47}-derived temperature of 15.1 ± 4.7°C, the middle set of blue-grey laminae, formed at 12.9 ± 4.7°C and the upper set of laminae below the hedges formed at 26.7 ± 4.1°C. Laminae from the second (L2) and third (L3) stromatolitic phases were formed at Δ_{47}-derived temperatures of 25.5 ± 4.7 °C and 20.7 ± 4.7°C respectively.

For dendrolitic phase D1, fabrics from two different dendrolite structures gave Δ_{47}-derived temperatures of 17.8 ± 4.7°C and 19.1 ± 4.1°C, respectively while the micritic sediment fill formed at 14.6 ± 4.7°C. In dendrolitic phase D2, a dendrolite structure returned a Δ_{47}-derived temperatures of 24.8 ± 4.1°C, while the micritic sediment fill formed at 23.0 ± 4.7°C. A second micritic sediment fill sample from D2 gave a different Δ_{47}-derived temperature of 15.2 ± 4.1°C.

The crosscutting sparry calcite vein precipitated calcite at Δ_{47} derived temperature of 33.7 ± 13.3°C.

In summary, the lowest temperatures are in the lower limestone layers below the Cotham Marble, between 4.4 ± 5.8°C (9.8) and 11.5 ± 4.7°C. The laminated stromatolite fabrics (L1-3) mainly formed at temperatures between 12.9 ± 4.7°C and 26.7 ± 4.1°C. The dendrolites seem to have formed at temperatures between about 17.8 ± 4.7°C and 24.8 ± 4.1°C, while the micritic fills within the dendrolitic phases formed at temperatures between about 14.6 ± 4.7°C and 23.0 ± 4.7°C. Overall the non-microbial micritic fabrics gave cooler temperatures than the microbial calcites.

The $\delta^{18}O_{FLUID}$ composition returned values between –3.8 ± 1.0‰ and –2.3 ± 0.1.0‰ for the facies below the Cotham Marble and values between –1.3 ± 1.0‰ and 1.7 ± 0.8‰ for the facies of the Cotham Marble. The only exception is a sample of the micritic fill of the upper dendrolitic phase which returned a composition of –3.6 ± 0.8‰; the clumped isotope values for this sample seem anomalous compared to those of the other facies, in particular compared to the Cotham Marble facies and this will be discussed in Chapter 5. The calcitic vein returned a $\delta^{18}O_{FLUID}$ composition of –3.6 ± 1.0‰.

Table 4.1 Clumped isotope data of facies in the specimen.

Sample		N	$\delta^{13}C$ (‰, VPDB)		$\delta^{18}O_{CARBONATE}$ (‰, VPDB)		Δ_{47} (CDES-25)		$T(\Delta_{47})$ (°C)	$\delta^{18}O_{FLUID}$ (‰, VPDB)
CM-Vein	Calcitic vein	3	-2.24	**–2.24 ± 0.02**	-7.589	**–7.62 ± 0.08**	0.586	**0.629 ± 0.015**	**33.7 ± 5.6**	**–3.6 ± 1.00**
			-2.20		-7.600		0.640			
			-2.29		-7.675		0.661			
CM-L3A	L3 laminae	3	0.43	**0.48 ± 0.02**	-1.142	**–0.99 ± 0.08**	0.655	**0.666 ± 0.015**	**20.7 ± 4.7**	**0.5 ± 0.96**
			0.47		-0.879		0.688			
			0.53		-0.950		0.656			
CM-D2f	D2 sediment fill	4	-1.55	**–1.57 ± 0.02**	-3.94	**–3.87 ± 0.07**	0.630	**0.684 ± 0.013**	**15.2 ± 4.1**	**–3.6 ± 0.83**
			-1.58		-3.83		0.731			
			-1.58		-3.89		0.683			
			-1.57		-3.84		0.690			
CM-D2f	D2 sediment fill	3	0.49	**0.49 ± 0.02**	-0.70	**–0.72 ± 0.08**	0.639	**0.659 ± 0.015**	**23.0 ± 4.7**	**1.2 ± 0.96**
			0.47		-0.75		0.683			
			0.49		-0.71		0.656			
CM-D2D	D2 dendrolite	4	-0.02	**0.05 ± 0.02**	-1.77	**–1.60 ± 0.07**	0.610	**0.654 ± 0.013**	**24.8 ± 4.1**	**0.7 ± 0.83**
			0.05		-1.74		0.682			
			0.07		-1.71		0.622			
			0.10		-1.18		0.702			
CM-L2A	L2 laminae	3	-0.58	**–0.59 ± 0.02**	-1.64	**–1.66 ± 0.08**	0.642	**0.625 ± 0.015**	**25.5 ± 4.7**	**0.8 ± 0.96**
			-0.59		-1.62		0.619			
			-0.62		-1.72		0.695			
CM-D1F	D1 sediment fill	3	0.45	**0.41 ± 0.02**	-0.40	**–0.47 ± 0.08**	0.670	**0.686 ± 0.015**	**14.6 ± 4.7**	**–0.3 ± 0.96**
			0.37		-0.49		0.711			
			0.42		-0.50		0.675			
CM-D1D	D1 dendrolite	3	0.40	**0.41 ± 0.02**	-1.21	**–1.17 ± 0.08**	0.639	**0.675 ± 0.015**	**17.8 ± 4.7**	**–0.3 ± 0.96**
			0.39		-1.23		0.726			
			0.42		-1.07		0.661			
CM-T1	D1 dendrolite	4	0.55	**0.56 ± 0.02**	-1.03	**–0.91 ± 0.07**	0.651	**0.671 ± 0.013**	**19.1 ± 4.1**	**0.2 ± 0.83**
			0.55		-1.06		0.699			
			0.57		-1.04		0.637			
			0.56		-0.50		0.698			
CM-L1up	L1 laminae	4	-0.84	**–0.81 ± 0.02**	-1.04	**–0.97 ± 0.07**	0.662	**0.649± 0.013**	**26.7 ± 4.1**	**1.7 ± 0.83**
			-0.80		-1.08		0.626			
			-0.84		-1.12		0.632			
			-0.77		-0.64		0.676			
CM-gl	L1 laminae	3	0.00	**–0.01 ± 0.02**	-1.04	**–1.05 ± 0.08**	0.665	**0.691 ± 0.02**	**12.9 ± 4.7**	**–1.3 ± 0.96**
			-0.01		-1.05		0.726			
			-0.02		-1.07		0.682			
CM-L1low	L1 laminae	3	-0.42	**–4.13 ± 0.02**	-1.07	**–1.04 ± 0.08**	0.681	**0.684 ± 0.02**	**15.1 ± 4.7**	**–0.8 ± 0.96**
			-0.42		-1.06		0.678			
			-0.40		-0.98		0.692			
CM-c	Layer above thrombolite (lat)	2		**0.72 ± 0.02**		**–1.40 ± 0.10**		**0.715 ± 0.018**	**4.4 ± 5.8**	**–3.5 ± 1.18**
			0.73		-1.63		0.702		9.8	
			0.71		-1.16		0.740		–0.8	
CM-TR	Thrombolite	3	0.40	**0.47 ± 0.02**	-1.44	**–1.42 ± 0.08**	0.697	**0.703 ± 0.015**	**9.4 ± 4.7**	**–2.4 ± 0.96**
			0.55		-1.39		0.704			
			0.44		-1.42		0.683			
CM-af1	Layer below thrombolite (lbt)	3	0.38	**0.34 ± 0.02**	-1.97	**–1.79 ± 0.08**	0.709	**0.696 ± 0.015**	**11.5 ± 4.7**	**–2.3 ± 0.96**
			0.32		-1.68		0.696			
			0.32		-1.71		0.718			
CM-b	Micritic layer	3	-0.47	**–0.45 ± 0.02**	-2.53	**–2.48 ± 0.08**	0.718	**0.708 ± 0.015**	**8.0 ± 4.7**	**–3.8 ± 0.96**
			-0.47		-2.48		0.721			
			-0.43		-2.44		0.685			

All ± values represent one standard error of the pooled standard deviation of groups, as described in Section 3.8.8. Data in bold are average values.

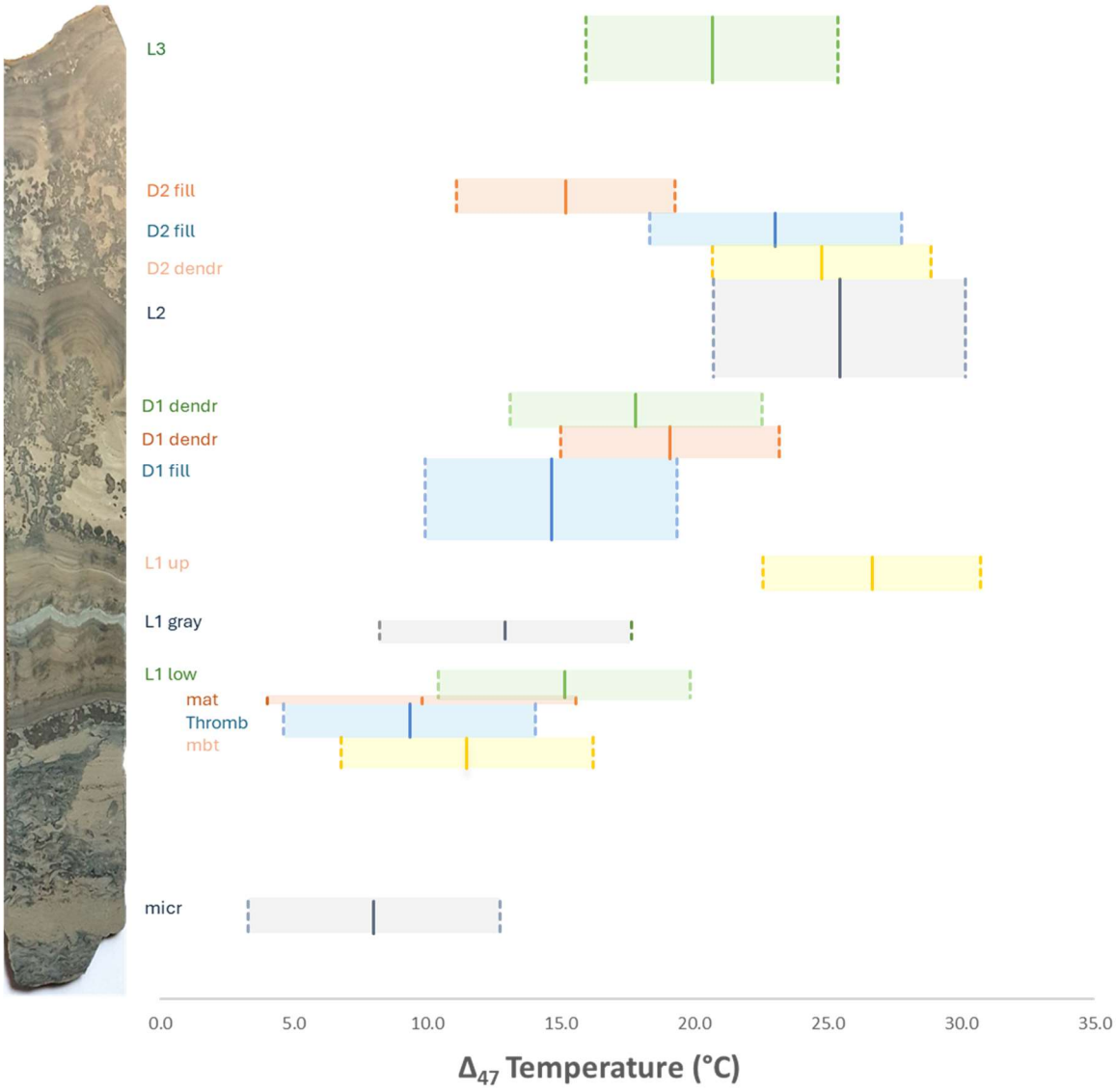

Figure 4.8 Clumped isotope measurements and reconstructed Δ47 temperatures in major facies: average temperatures (solid vertical lines) and standard errors (dotted lines and transparent bars) for each facies type. mat: layer below thrombolites; mbt: layer below thrombolites; Thromb: thrombolites; dendr: dendrolite structure; fill: sediment filling the space between dendrolites.

4.3 Stable isotope: bulk measurements

Stable isotope bulk measurements were made throughout the Wickwar samples, the density of samples reflecting the depositional textures and mesostructures. For example, samples from stromatolite layers were taken along laminae with a resolution of 250-300 μm. Samples from the layers below the Cotham Marble were extracted along horizontal transects, or identifiable laminae, with a resolution of 250-500 μm depending on mesostructures present. Samples from dendrolites were extracted mainly from patches of the dendrolites and, separately, the micritic sediment fills between dendrolites.

The total range in $\delta^{18}O$ is about 7.5‰ (between (0.0 and –7.5‰ VPDB), although most of the values are between –2.5 and –0.5‰ VPDB. Within the Cotham Marble facies $\delta^{18}O$ and $\delta^{13}C$ values below ca. –2 and –1 ‰ VPDB respectively can be considered 'outlier points. In the Upper Cotham Member below the microbialites, the data distribution suggests that $\delta^{18}O$ and $\delta^{13}C$ values of outlier points may be lower, below ca. –3 and –0.5 ‰ VPDB respectively. The significance of these values is discussed in section 5.2.

4.3.1 Lower layer with shells

The lower micritic layer with shells is the lowest part of the Upper Cotham Member within the specimen. Samples (SLa in Figure 4.9) were taken from lines and patches according to the presence of shells.

The $\delta^{13}C$ values range from –1.1‰ VPDB to 0.1‰ VPDB (average = –0.1 ± 0.2‰ VPDB), but mostly (27 samples) between –0.2‰ VPDB and 0.1‰ VPDB. Only 6 samples have positive $\delta^{13}C$ values and two have 0.0‰ VPDB, so 27 samples have negative $\delta^{13}C$ values. The $\delta^{18}O$ values of all 35 samples are negative and limited between –2.3‰ VPDB and –3.9‰ VPDB ($\delta^{18}O$ average value = –2.6 ± 0.3‰ VPDB), although most of them (27 samples) are grouped between –2.3‰ VPDB and –2.8‰ VPDB (Figure 4.9).

4.3.2 Mixed layer with shells.

Above the lower micritic layer with shells there is a layer with unlaminated micritic matrix mixed with other parts rich in fossils, mainly bivalves. The part partially including shells was sampled at 500-1000 μm (SLb). A vein of massive micritic matrix was sampled separately at 1000 μm (SLc) (Figure 4.9a).

Both sets of data (SLb and SLc) show increasing values of both oxygen and carbon isotope data from the stratigraphically lower samples upwards, apart from some exceptions and overlaps (Figures 4.9, 4.10, 4.11). Shell samples and patches of darker matrix largely seems to have values close to their stratigraphically equivalent samples. $\Delta^{13}C$ values range between –1.2‰ VPDB and 1.1‰ VPDB (SLb $\delta^{13}C$ average value = 0.1 ± 0.5‰ VPDB, SLc $\delta^{13}C$ average value = 0.6 ± 0.5‰ VPDB). $\Delta^{18}O$ values are all negative between –4.0‰ VPDB and – 1.4‰ VPDB (SLb $\delta^{18}O$ average value = – 2.2 ± 0.5‰ VPDB, SLc $\delta^{18}O$ average value = – 2.0 ± 0.5‰ VPDB).

4.3.3 Thrombolite layer.

The thrombolite data are from 6 samples extracted from patches and show similar values (Figure 4.9a). Carbon isotope values vary little around 0.9‰ VPDB ($\delta^{13}C$ average value = 0.9 ± 0.0‰ VPDB). Oxygen isotope values are all negative between –1.7‰ VPDB and –1.2‰ VPDB ($\delta^{18}O$ average value = –1.5 ± 0.1‰ VPDB) (Figures 4.9, 4.11).

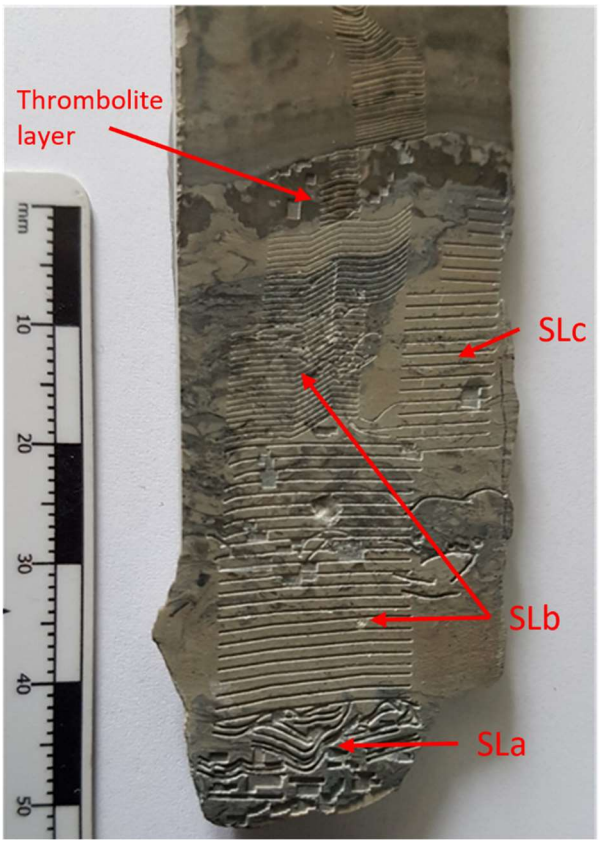

a

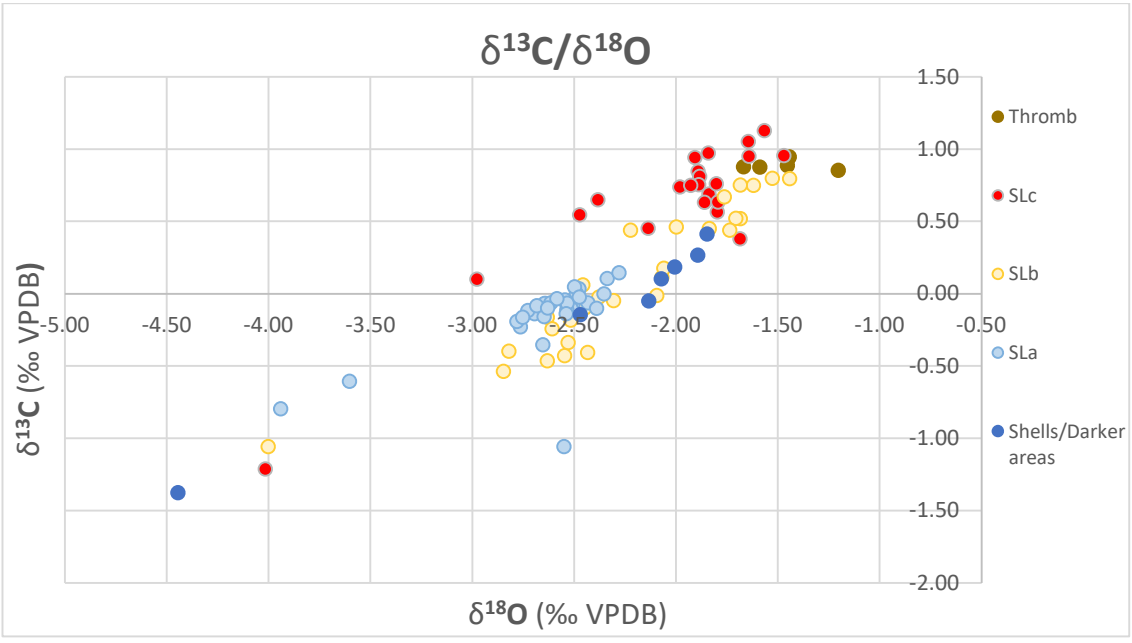

b

Figure 4.9 (a) Microdrill traces for the extraction of samples over the lowest part of the Upper Cotham Member, the thrombolitic layer and part of the first stromatolitic phase. Samples for bulk measurements are SLa: lower micritic layer with shells; SLb: mixed layer partially including shells; SLc: vein of massive micritic matrix; (b) Stable isotope composition for oxygen and carbon of the layer within the Upper Cotham Member below the Cotham Marble. Different colours indicate different layers, shells, darker areas and the thrombolite layer, according to their stratigraphic position;

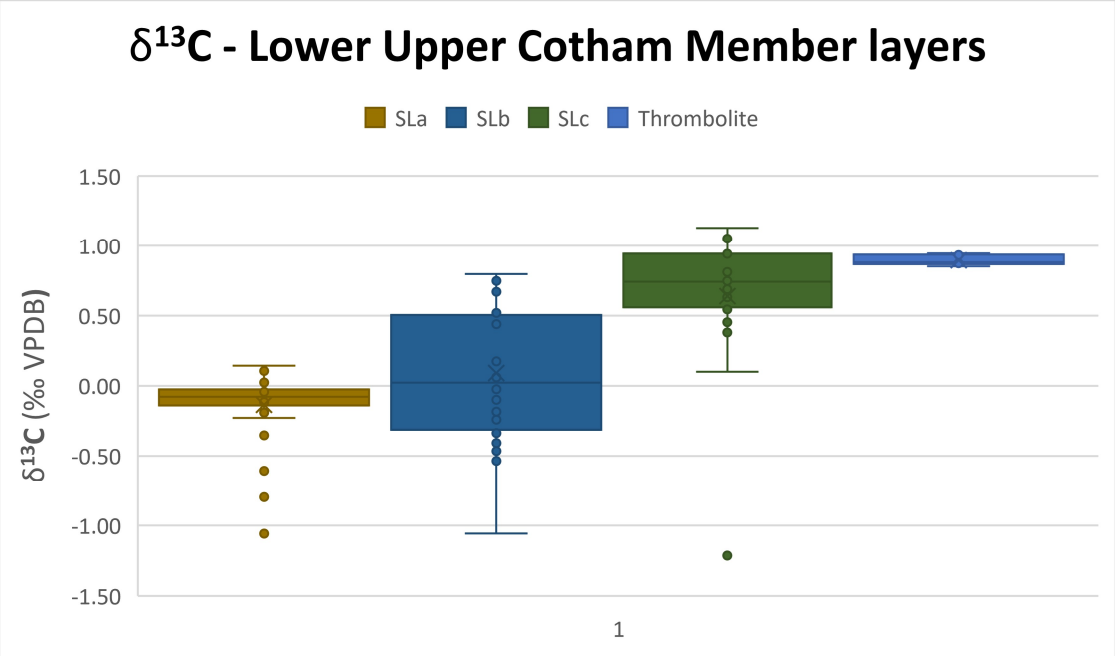

Figure 4.10 Box and whisker plot of the lower layers in the specimen studied in this study. Whiskers and box boundaries indicate from bottom: minimum, first quartile, median (segment inside box), mean (x), third quartile (upper box segment) and maximum values. The data outside the minimum and maximum are outlier data (statistically excluded by the Excel algorithm).

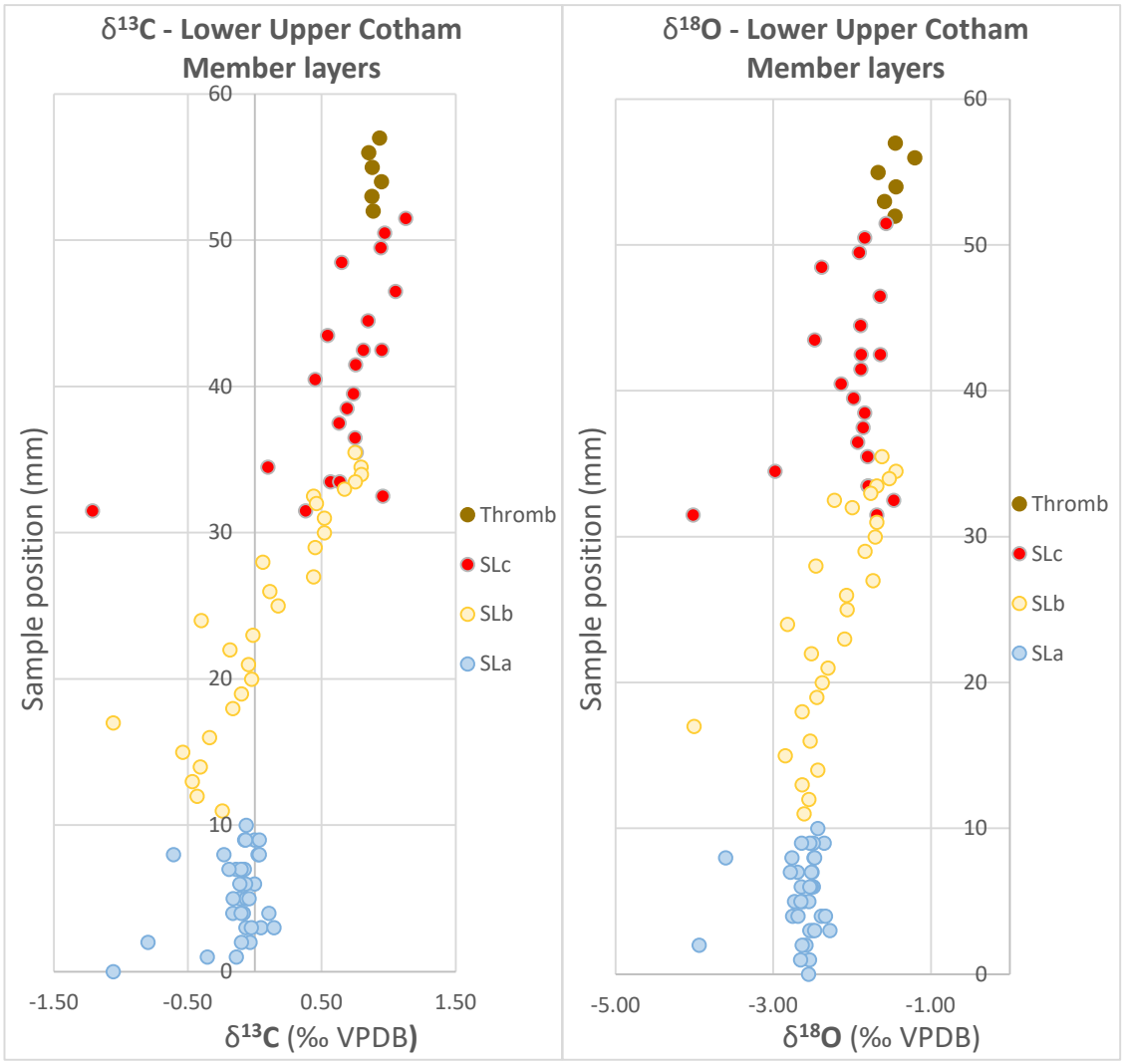

Figure 4.11 Stable isotope composition for carbon and oxygen, according to the sample stratigraphic position, of the layers within the Upper Cotham Member below the Cotham Marble. Different colours indicate different layers according to their distance from the base of SLa.

4.3.4 Lower stromatolite laminae, L1.

Samples from the lower stromatolite, L1, were extracted with a resolution of 250-300 μm. In figures, different colours indicate sets of laminae from the base to the top of L1. For comparison in Figures 4.12 and 4.13 are the data from the thrombolite below the base of L1.

The $\delta^{13}C$ data range from –2.1‰ VPDB to 0.6‰ VPDB, but mostly between –0.9‰ VPDB and 0.6‰ VPDB ($\delta^{13}C$ average value = –0.2 ± 0.5‰ VPDB). The samples that have the most negative $\delta^{13}C$ values are along the middle (L1g) of L1, while the most positive $\delta^{13}C$ values are the lowest (L1a), and at the top (L1n, L1m). The $\delta^{18}O$ values are limited between –2.4‰ VPDB and 0.0‰ VPDB, but most of them are between –1.3‰ VPDB and –0.6‰ VPDB ($\delta^{18}O$ average value = –1.0 ± 0.3‰ VPDB) (Figure 4.12b, 4.13). There is no correlation between carbon and oxygen isotope data ($R^2 = 0.04$).

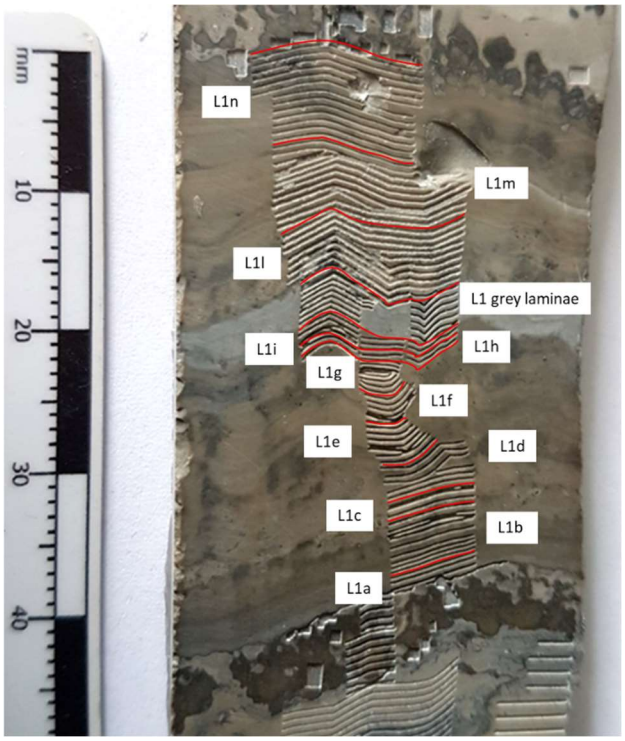

a

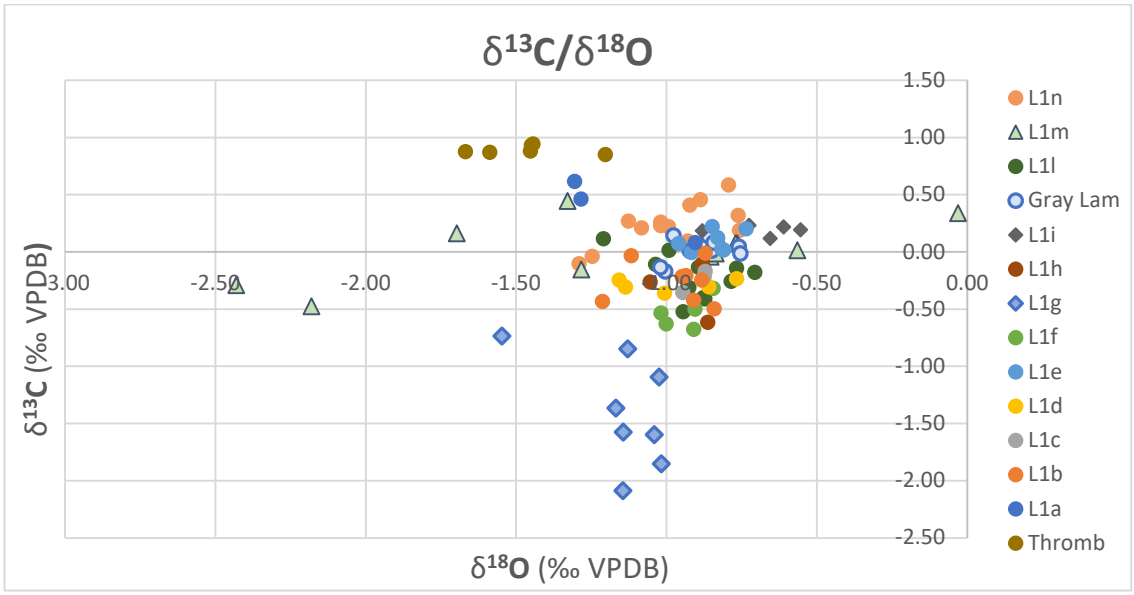

b

Figure 4.12 (a) Microdrill traces for the extraction of samples over L1 and labelled groups of samples; (b) Stable isotope composition for oxygen and carbon of the laminae of the lower stromatolite, L1. Groups include sets of different width. Different colours for groups of samples indicate the position of the laminae from the base of L1 and of the thrombolite layer.

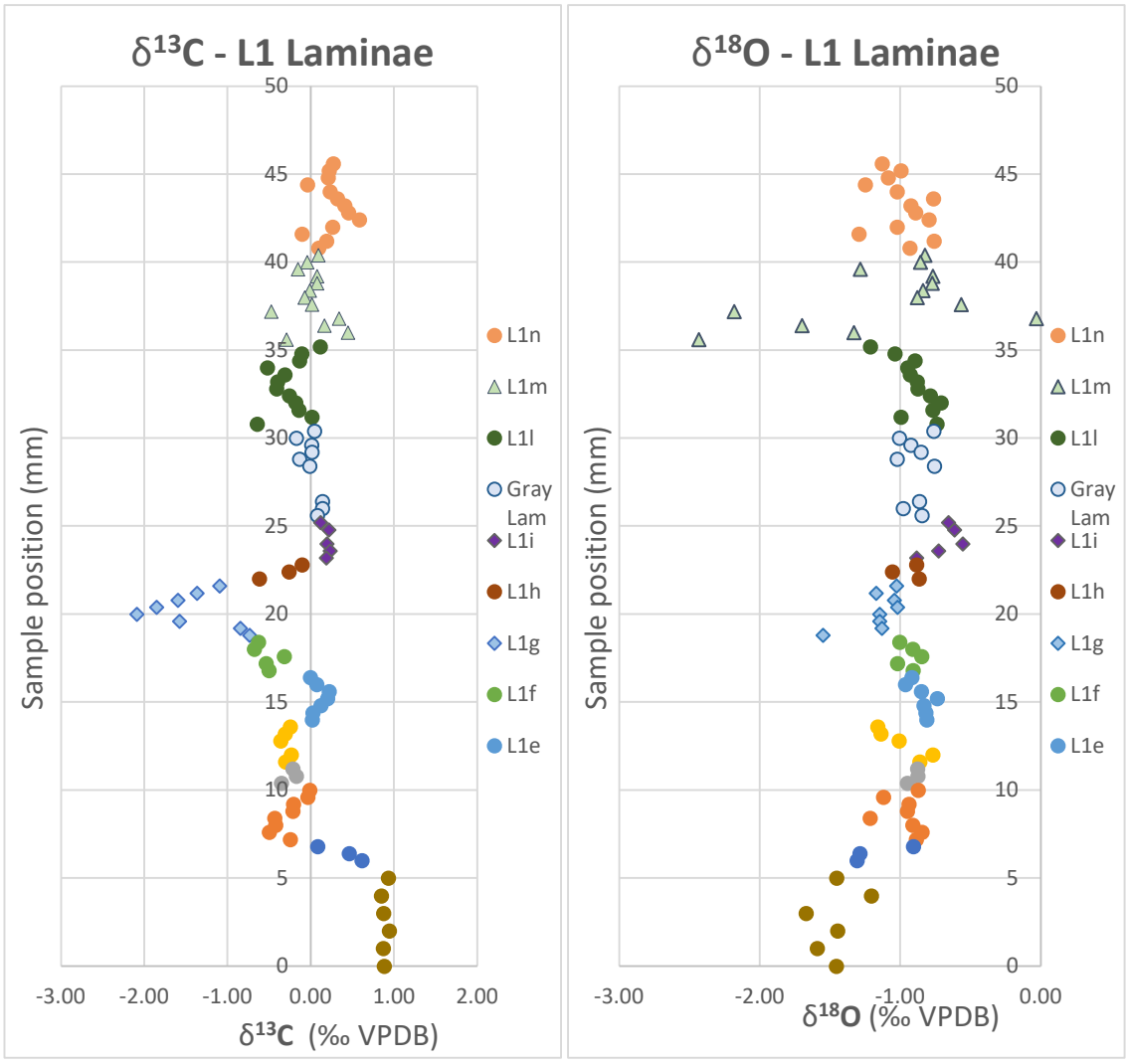

Figure 4.13 Stable isotope composition for carbon and oxygen, according to the sample stratigraphic position, of the thrombolite and stromatolite L1 of the Cotham Marble. Different colours indicate different set of laminae according to their distance from the base of thrombolites.

4.3.5 Lower dendrolite, D1.

Samples were extracted from patches within the lower dendrolites (Figure 4.14a). To distinguish the trend of the stable isotope values according to the stratigraphic position of the samples from the base of the dendrolite layer, in Figures 4.14 b and 4.15 both dendrolite and sediment fill samples have been divided in four groups each representing about 10 mm(Figure 4.14a).

The carbon isotope values for the dendrolite structures are between –2.3‰ VPDB and 0.8‰ VPDB ($\delta^{13}C$ average value = 0.3 ± 1.0‰ VPDB), but most samples have positive values between 0.5‰ VPDB and 0.8‰ VPDB. $\Delta^{13}C$ values for the sediment fill range between –2.6‰ VPDB and 0.9‰ VPDB ($\delta^{13}C$ average value = 0.1 ± 0.7‰ VPDB) but vary mostly between – 0.8‰ VPDB and 0.9‰ VPDB.

The oxygen isotope values for the dendrolite structures vary between –7.1‰ VPDB and – 0.8‰ VPDB, but most values vary between –1.7‰ VPDB and –0.8‰ VPDB ($\delta^{18}O$ average value = –1.6 ± 1.6‰). The oxygen isotope values for the sediment fill range between –7.5‰ VPDB and –0.4‰ VPDB, although most of the data are within –2.5‰ VPDB and –0.4‰ VPDB ($\delta^{18}O$ average value = –1.7 ± 1.3‰).

Carbon and oxygen isotope data show a high correlation, R^2=0.78 for the sediment fill and R^2=0.99 for the dendrolite structures.

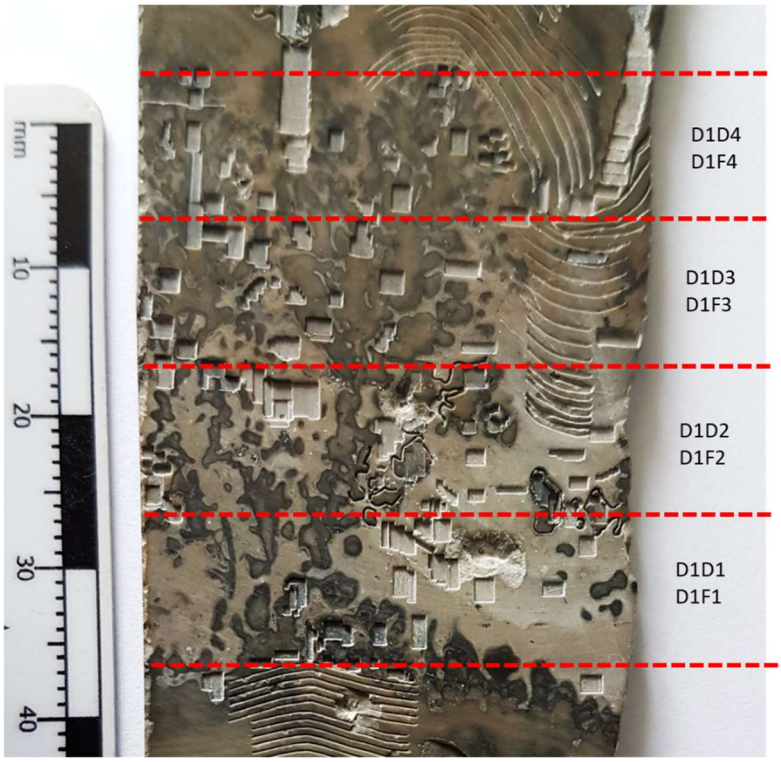

a

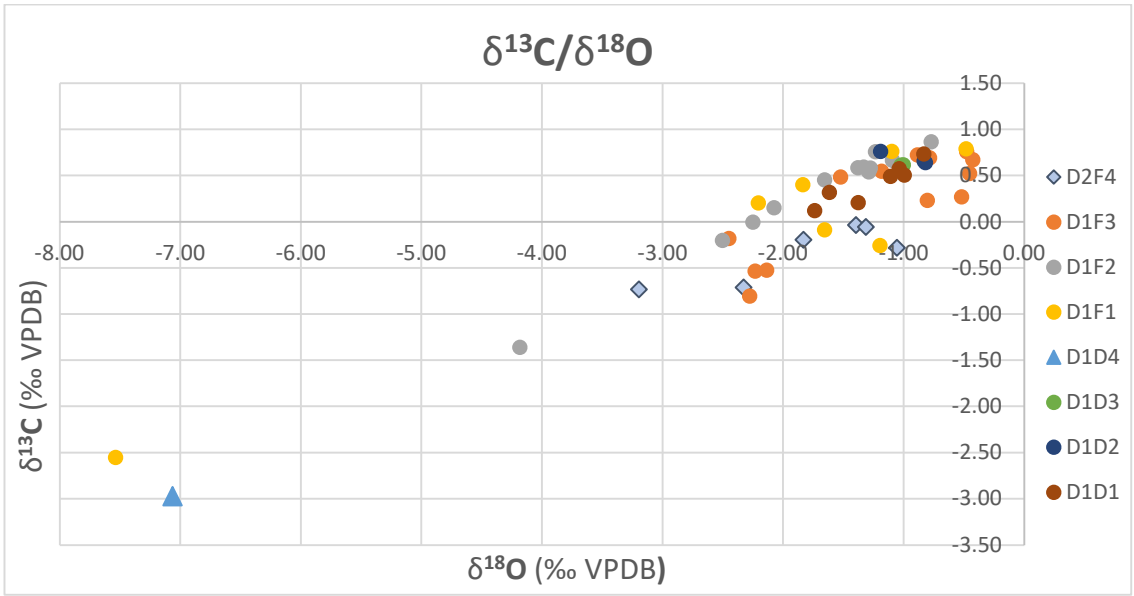

b

Figure 4.14 (a) Microdrill traces for the extraction of samples over D1 and respective labelled areas of extraction of the lower dendrolite structures, D1Dn, and related sediment fill, D1Fn; (b) Stable isotope composition for oxygen and carbon of the lower dendrolite structures, D1Dn, and related sediment fill, D1Fn. Different categories indicate the position of the samples from the base of D1. Each group, denoted by n, indicates samples within 10 mm, i.e. D1D3 and D1F3 indicates respectively samples from dendrolite structures and sediment fill within 31-40 mm from the base.

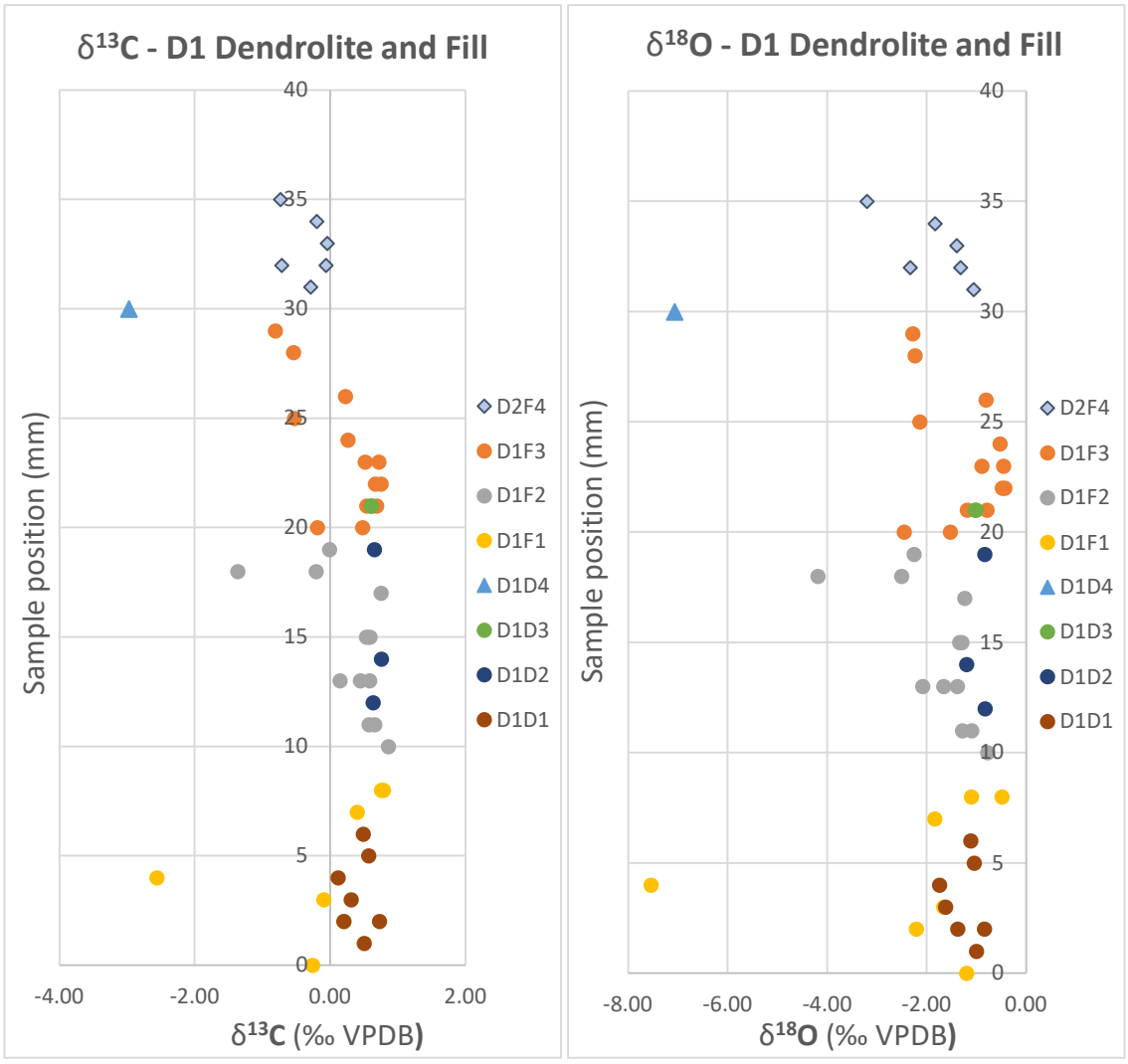

Figure 4.15 Stable isotope composition for carbon and oxygen, according to the sample stratigraphic position of lower dendrolite structures, D1Dn, and related sediment fill, D1Fn. Different categories indicate sets of samples according to their distance from the base of D1. Each group, denoted by n, indicates 10 mm, i.e. D1D3 indicates samples within 31-40 mm from the base.

4.3.6 Middle stromatolite laminae, L2.

Samples were taken from laminae about 250-300 μm apart (Figure 4.16a). The data show that the samples appear divided in two groups according to their stratigraphic position (Figures 4.16, 4.17).

The carbon isotope data for the lower and middle laminae range from 0.0‰ VPDB to 0.7‰ VPDB, with a general trend of increasing values throughout the L2 low and L2 mid. The carbon isotope data for the upper laminae range from 0.1‰ VPDB to 0.5‰ VPDB and are scattered but show a general trend of values decreasing upwards. $\Delta^{13}C$ average value for all L2 laminae is 0.3 ± 0.2‰ VPDB.

The oxygen isotope values for the lower and middle laminae are mostly limited between – 1.3‰ VPDB and –0.7‰ VPDB. The oxygen isotope values for the upper laminae are limited between –2.1‰ VPDB and –1.4‰ VPDB. The $\delta^{18}O$ average value for all L2 laminae is –1.3 ± 0.4‰ VPDB.

The data show a low correlation (R^2=0.53) between carbon and oxygen isotope data within L2.

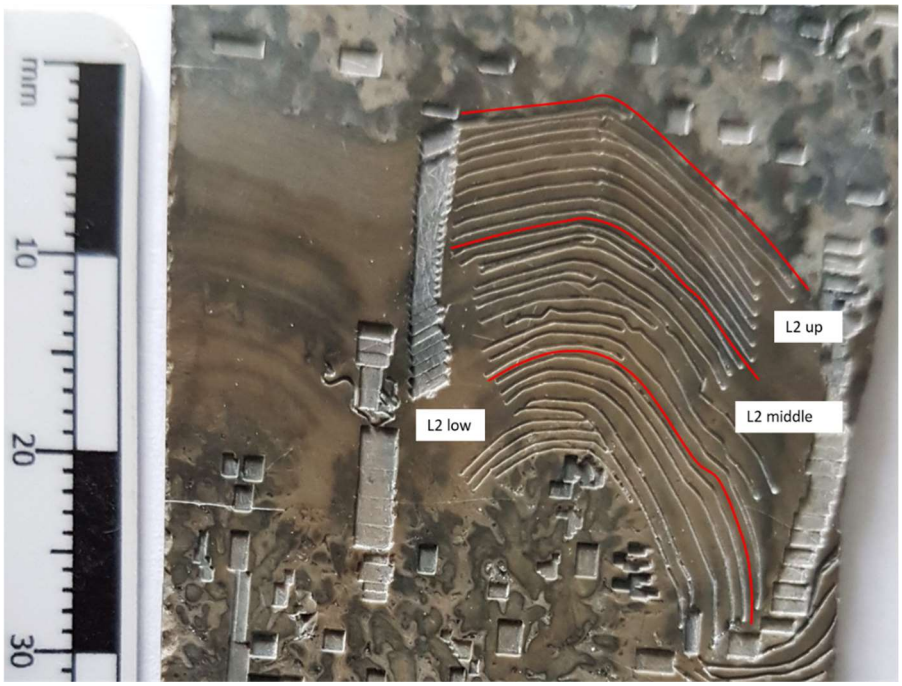

a

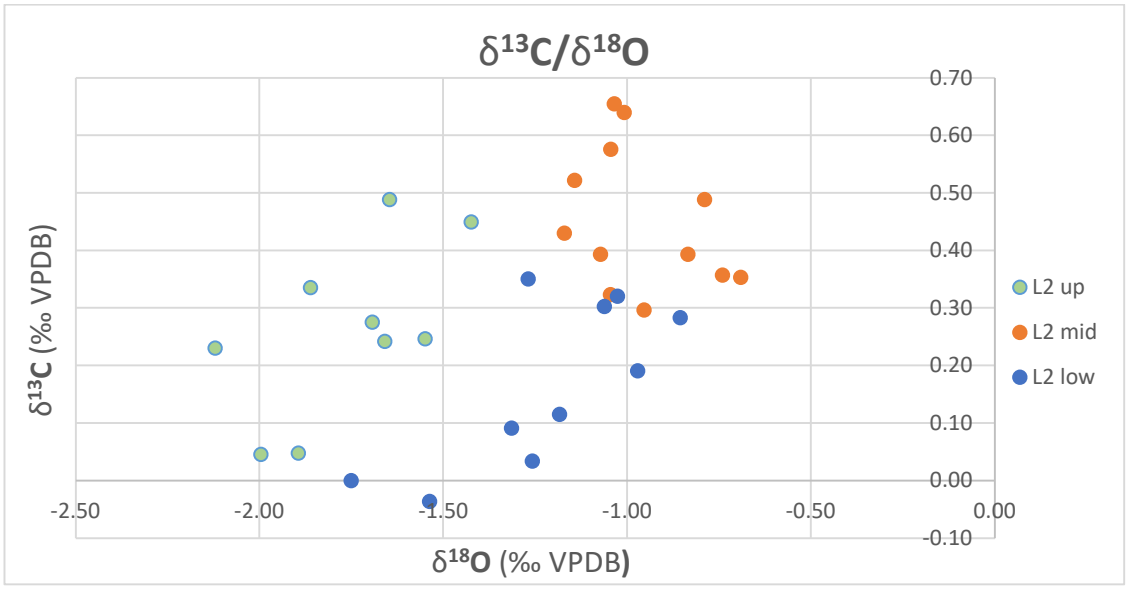

b

Figure 4.16 (a) Microdrill traces for the extraction of samples over L2 and labelled groups of samples; (b) Stable isotope composition for oxygen and carbon of laminae of the middle stromatolite, L2. Different categories indicate the position of the laminae within L2.

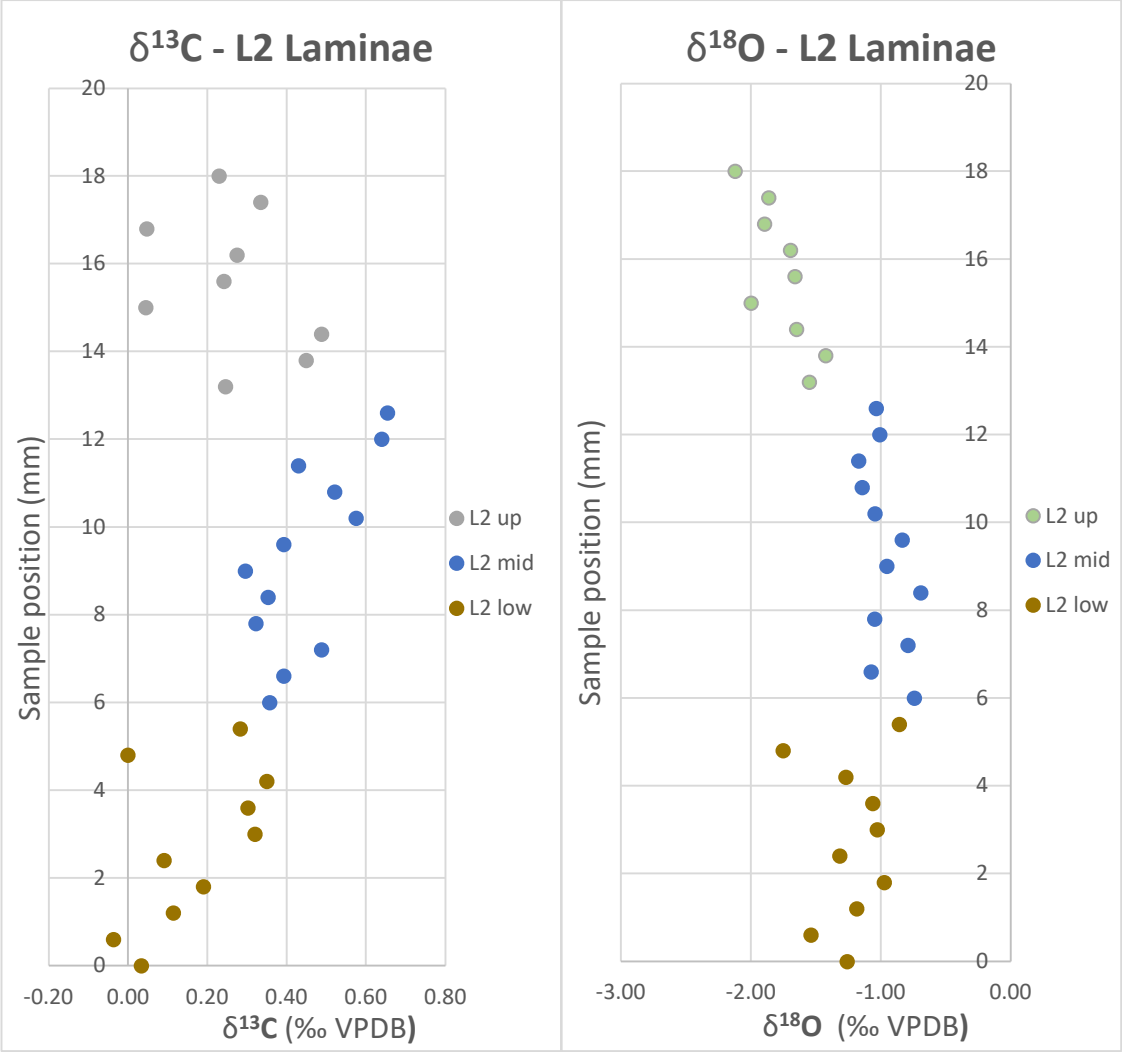

Figure 4.17 Stable isotope composition for carbon and oxygen, according to the sample stratigraphic position, of the stromatolite laminae within L2. Different categories indicate different set of laminae according to their distance from the base of L2.

4.3.7 Depressions within L2.

Three series of samples were taken from two depressions within the L2 laminae (Figure 4.18a). Although the series were taken in areas of discontinuity of the laminae, only the third, L2Dep C, seems to be filled with sediment. The first two series are adjacent, a few millimetres apart within the same depression, and the top samples of the first series, L2Dep A, overlap stratigraphically with the lower samples of the second series, L2Dep B. The samples stratigraphically overlapping have been taken from the laminae with the microdigitate or burrow features.

The carbon isotope values for the first and second series are mostly between –1.7‰ VPDB and 0.6‰ VPDB (L2Dep A $\delta^{13}C$ average value = –0.3 ± 0.4‰ VPDB; L2Dep B $\delta^{13}C$ average value = 0.0 ± 0.4‰ VPDB). The carbon isotope values for the third series are mostly between –2‰ VPDB and 0.4‰ VPDB ($\delta^{13}C$ average value = –0.4 ± 0.8‰ VPDB).

The oxygen isotope values for the first and second series are mostly between –2.1‰ VPDB and –0.8‰ VPDB (L2Dep A $\delta^{18}O$ average value = –1.6 ± 0.8‰ VPDB; L2Dep A $\delta^{18}O$ average value = –1.6 ± 0.4‰ VPDB). The oxygen isotope values for the third series are mostly between –4.1‰ VPDB and –1.1‰ VPDB (L2Dep C $\delta^{18}O$ average value = – 2.3 ± 0.9‰ VPDB) (Figures 4.18b and 4.19).

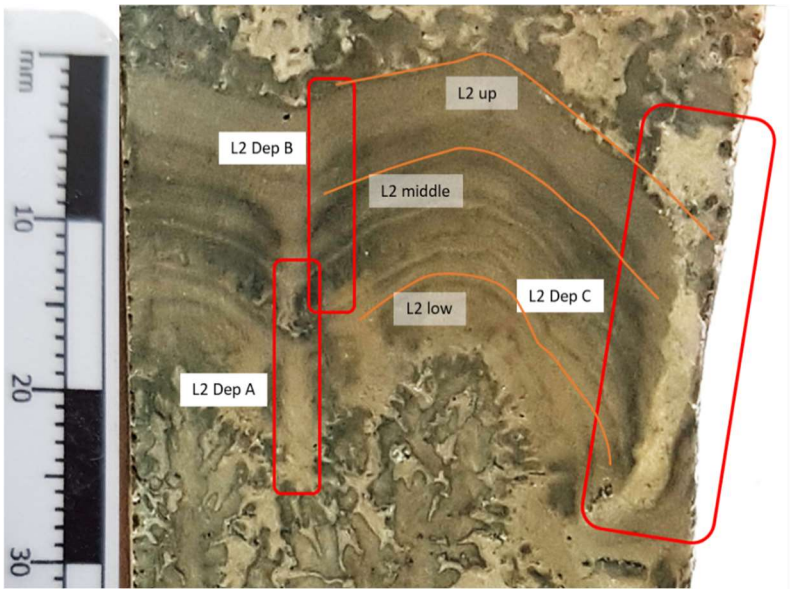

a

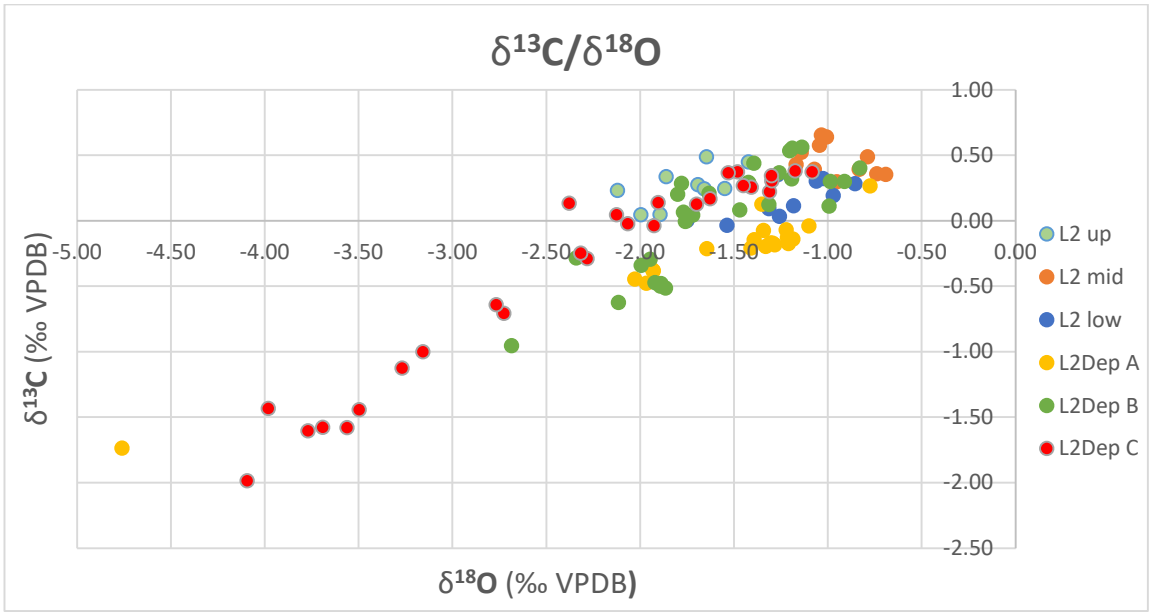

b

Figure 4.18 (a) Areas (red circles) where the samples were extracted for the depressions compared to L2 groups (orange lines) and labels for respective groups of samples; (b) Stable isotope composition for oxygen and carbon of the stromatolite laminae, L2, and depressions within stromatolite laminae, L2. Different categories indicate the stratigraphic position of the samples from the base of L2.

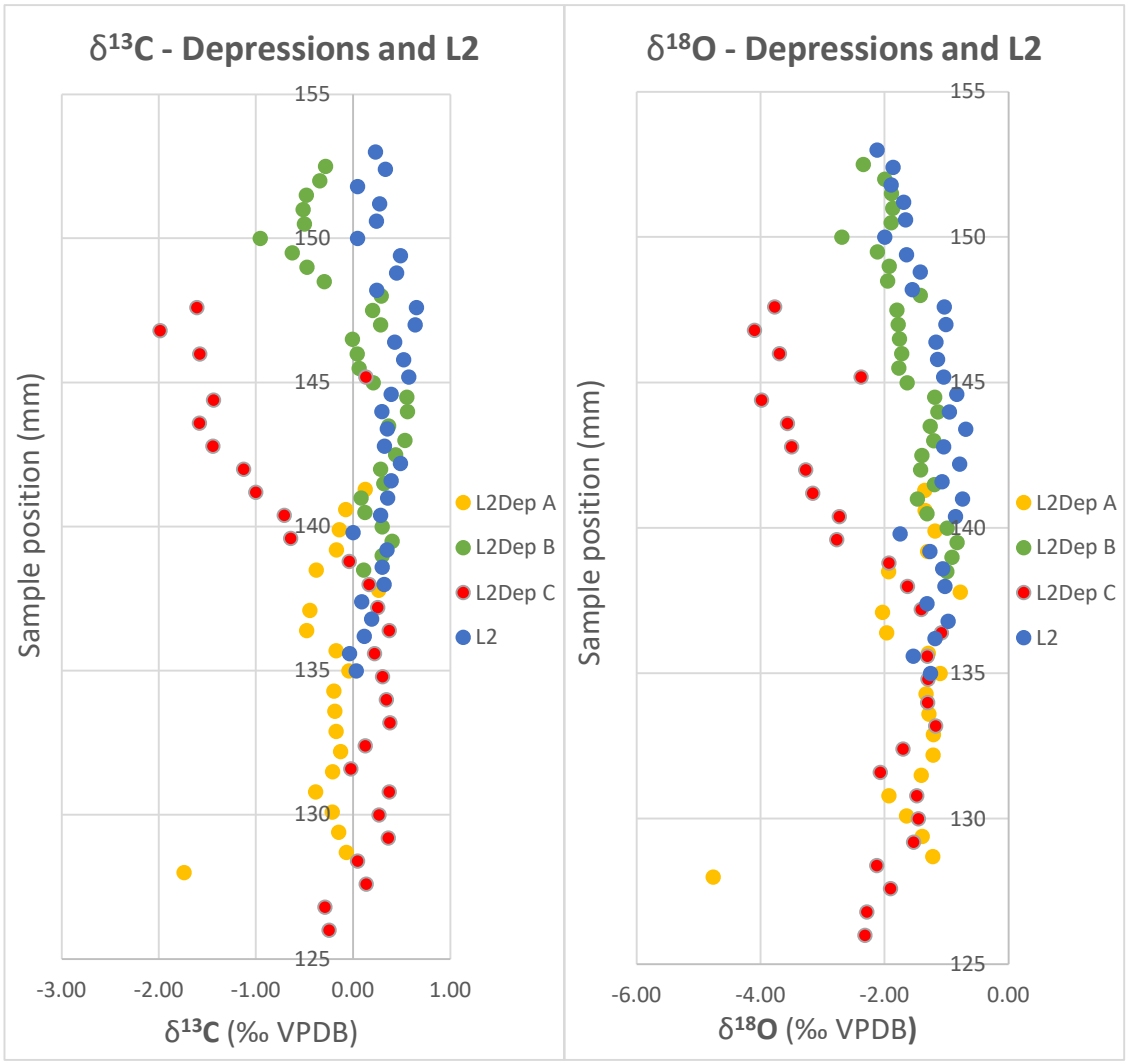

Figure 4.19 Stable isotope composition for carbon and oxygen, according to the sample stratigraphic position, of the stromatolite laminae within L2. Different categories indicate series of samples within depressions and laminae of L2 according to their distance from the base of the specimen.

4.3.8 Upper dendrolite, D2

Samples were extracted from patches (Figure 4.20a). In Figures 4.20 b and 4.21, each category represents 10 mm of both dendrolites (D2Dn) and sediment filling the space between dendrolites (D2Fn) to better relate samples to their stratigraphic position.

The carbon isotope values of the sediment fill vary between –0.9‰ VPDB and 1.0‰ VPDB ($\delta^{13}C$ average value = 0.5 ± 0.4‰ VPDB). The oxygen isotope values of the matrix vary between –2.6‰ VPDB and –0.2‰ VPDB ($\delta^{18}O$ average value = – 1.2 ± 0.7‰ VPDB).

The carbon isotope values of the dendrolite vary between –0.6‰ VPDB and 0.8‰ VPDB ($\delta^{13}C$ average value = 0.5 ± 0.3‰ VPDB), while the oxygen isotope values of the dendrolite vary between –2.3‰ VPDB and –0.6‰ VPDB ($\delta^{18}O$ average value = – 1.4 ± 0.4‰ VPDB).

The carbon and oxygen isotope values show higher correlation (R^2=0.63) in the sediment fill than in the dendrolites (R^2 = 0.40).

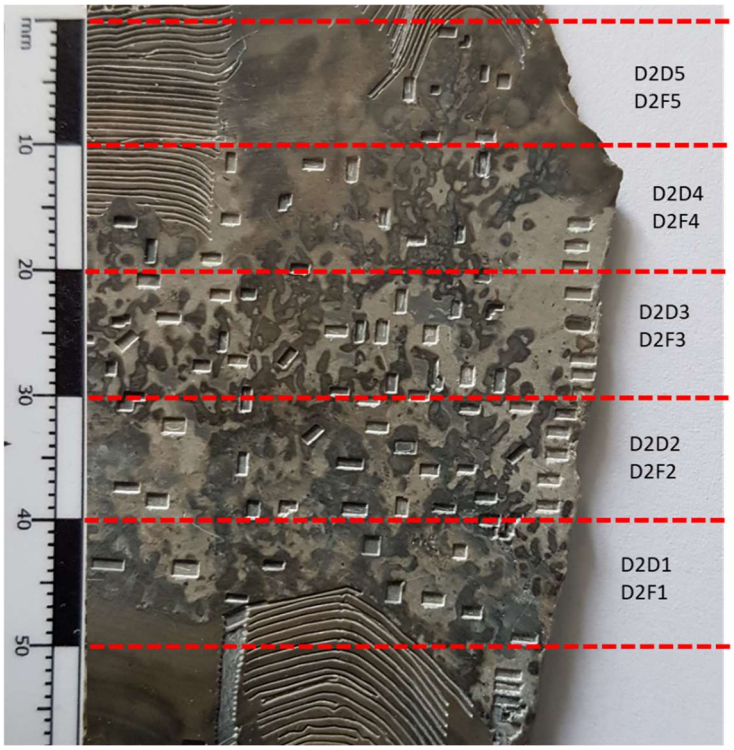

a

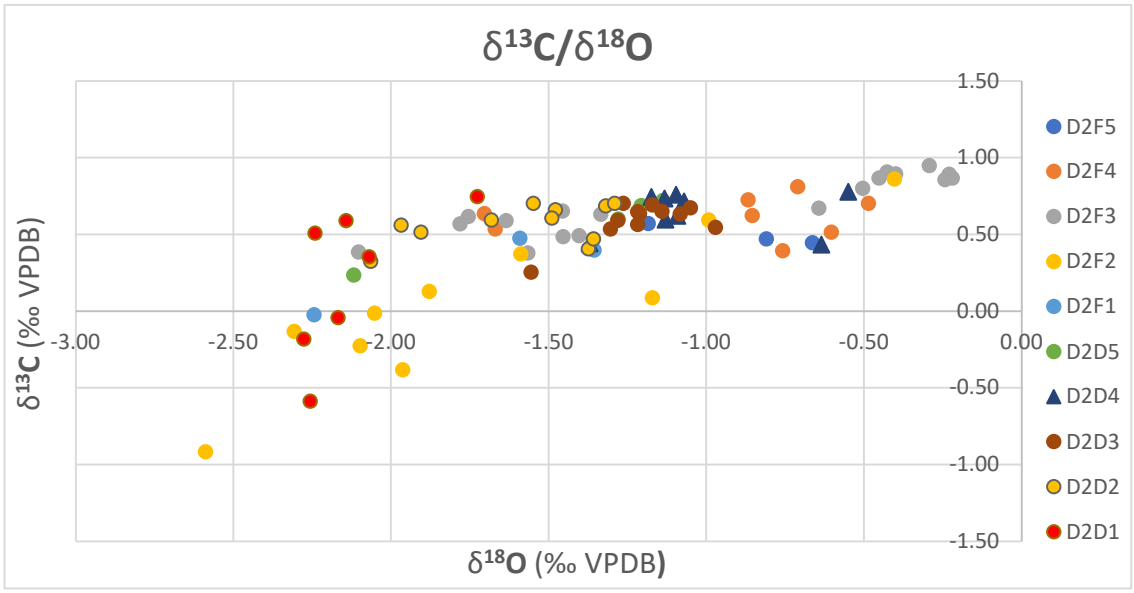

b

Figure 4.20 (a) Microdrill traces for the extraction of samples over D2 and respective labelled areas of extraction of the lower dendrolite structures, D2Dn, and related sediment fill, D2Fn; (b) Stable isotope composition for oxygen and carbon of the upper dendrolites and sediment fill, D2. Different categories indicate the position of samples within the sediment fill, D2Fn, and the dendrolites, D2Dn. Each group, denoted by n, indicates samples within 10 mm, i.e. D2D3 and D2F3 indicates respectively samples from dendrolite structures and sediment fill within 31-40 mm from the base.

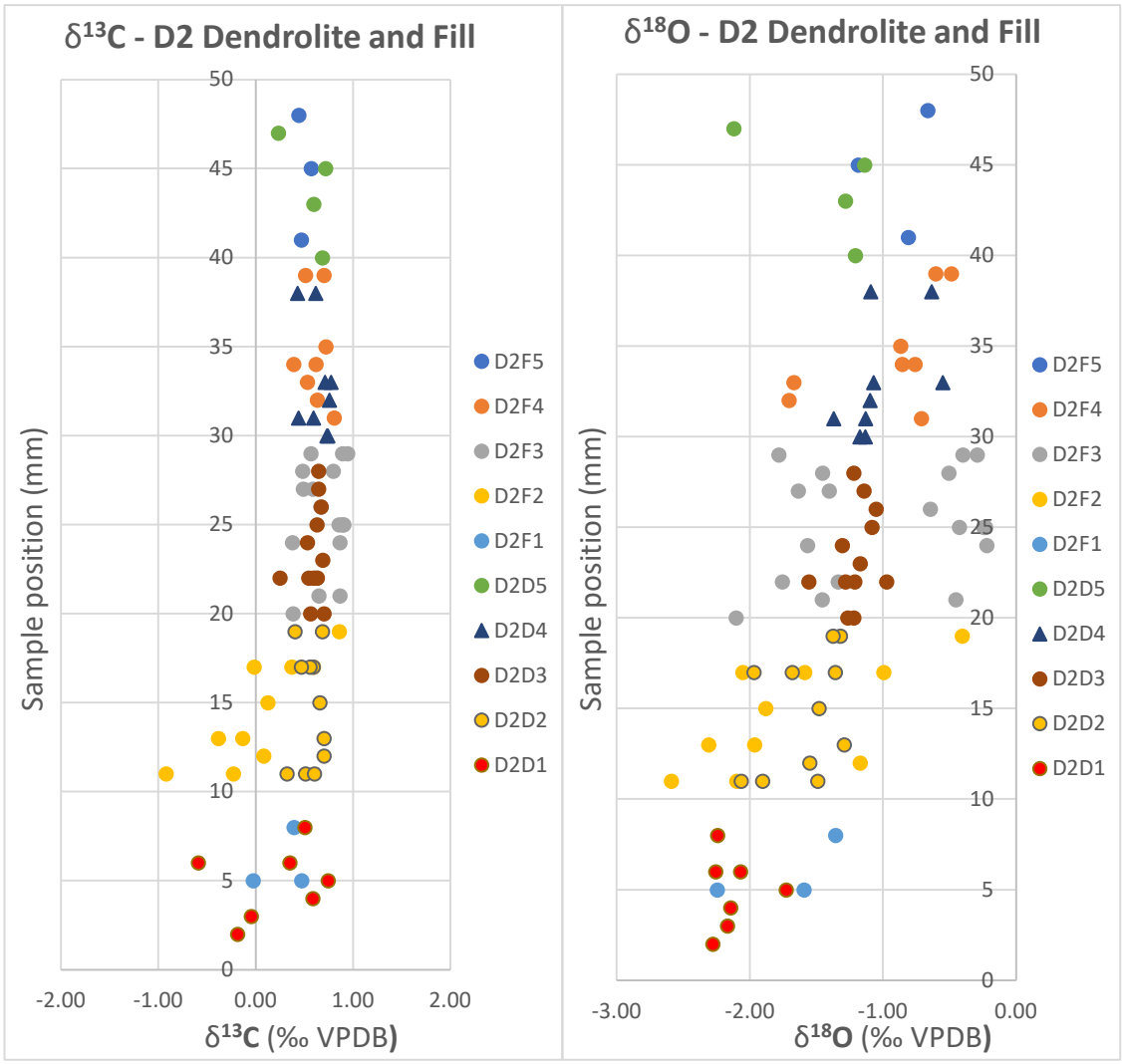

Figure 4.21 Stable isotope composition for carbon and oxygen, according to the sample stratigraphic position of upper dendrolite structures, D2Dn, and related sediment fill, D2Fn. Different categories indicate sets of samples according to their distance from the base of D2. Each group, denoted by n, indicates 10 mm, i.e. D1D3 indicates samples within 31-40 mm from the base.

4.3.9 Upper stromatolite laminae, L3.

Samples were taken from the upper stromatolite about 250-300 μm apart along two adjacent series, L3 low and L3 up, and L3 low b, which only covers the lower part of the laminae within L3.

The carbon isotope data for the lower laminae range from 0.2‰ VPDB to 0.6‰ VPDB. The carbon isotope data for the upper laminae range from 0.2‰ VPDB to 0.7‰ VPDB. Only one sample in L3 low b has carbon and oxygen isotope values very far from the range outlined above. The $\delta^{13}C$ average value for all L3 laminae is 0.5 ± 0.1‰ VPDB (Figures 4.22 and 4.23).

The oxygen isotope values for the lower laminae are limited between –1.3‰ VPDB and – 0.6‰ VPDB. The oxygen isotope values for the upper laminae are limited between – 2.4‰ VPDB and –1.4‰ VPDB. The $\delta^{18}O$ average value for all L3 laminae is – 1.3 ± 0.5‰ VPDB.

There is no correlation between carbon and oxygen isotope values.

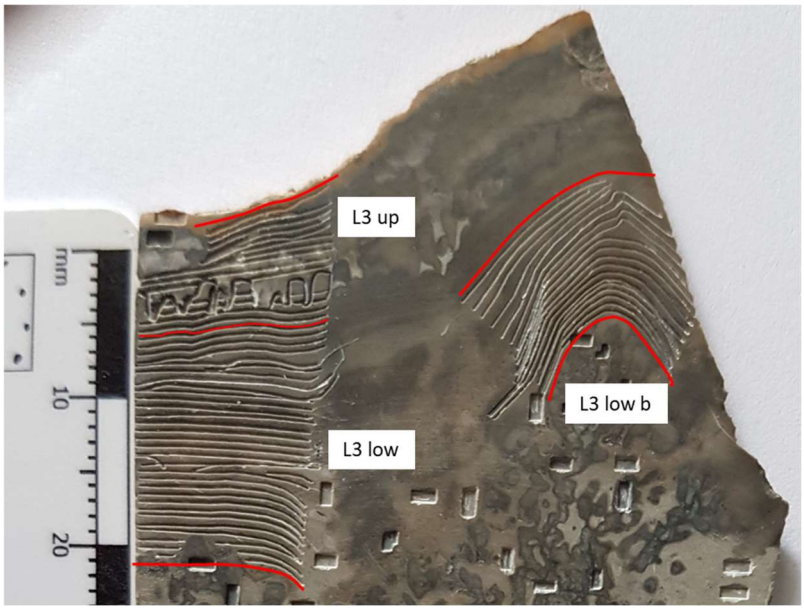

a

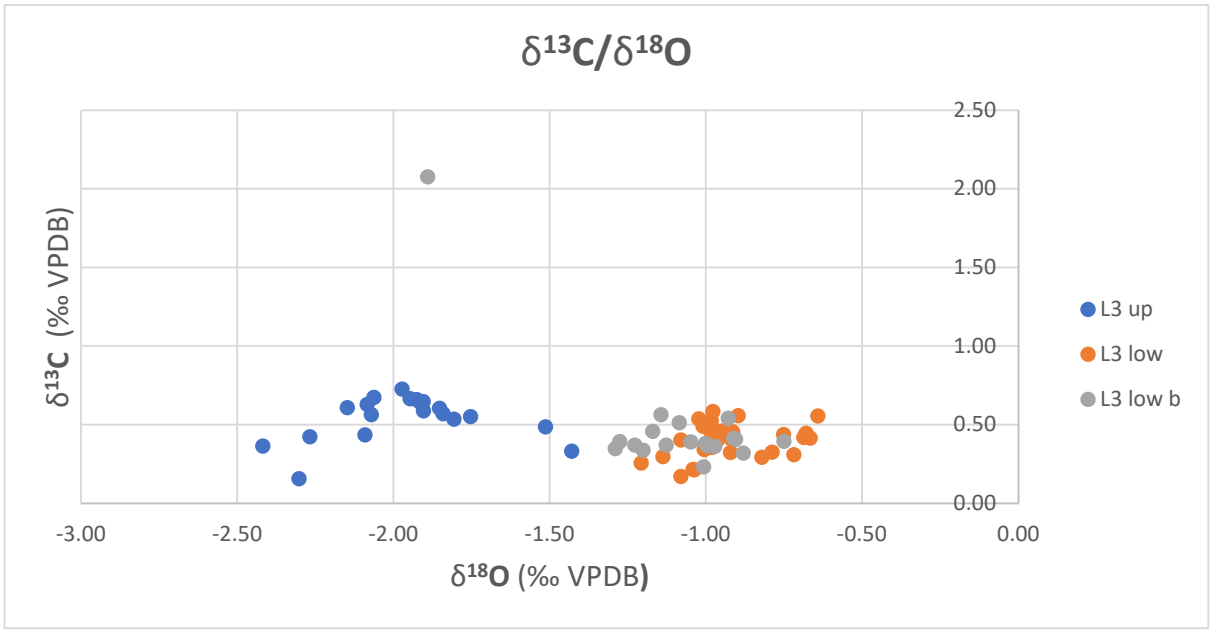

b

Figure 4.22 (a) Microdrill traces for the extraction of samples over L3 and labelled groups of samples; (b) Stable isotope composition for oxygen and carbon of laminae of the upper stromatolite, L3. Different categories indicate the position of the laminae within L3. Data are from two adjacent series, with the first series including L3 low and L3 up, and the second series, L3 low b, including only the lower part of the laminae within L3.

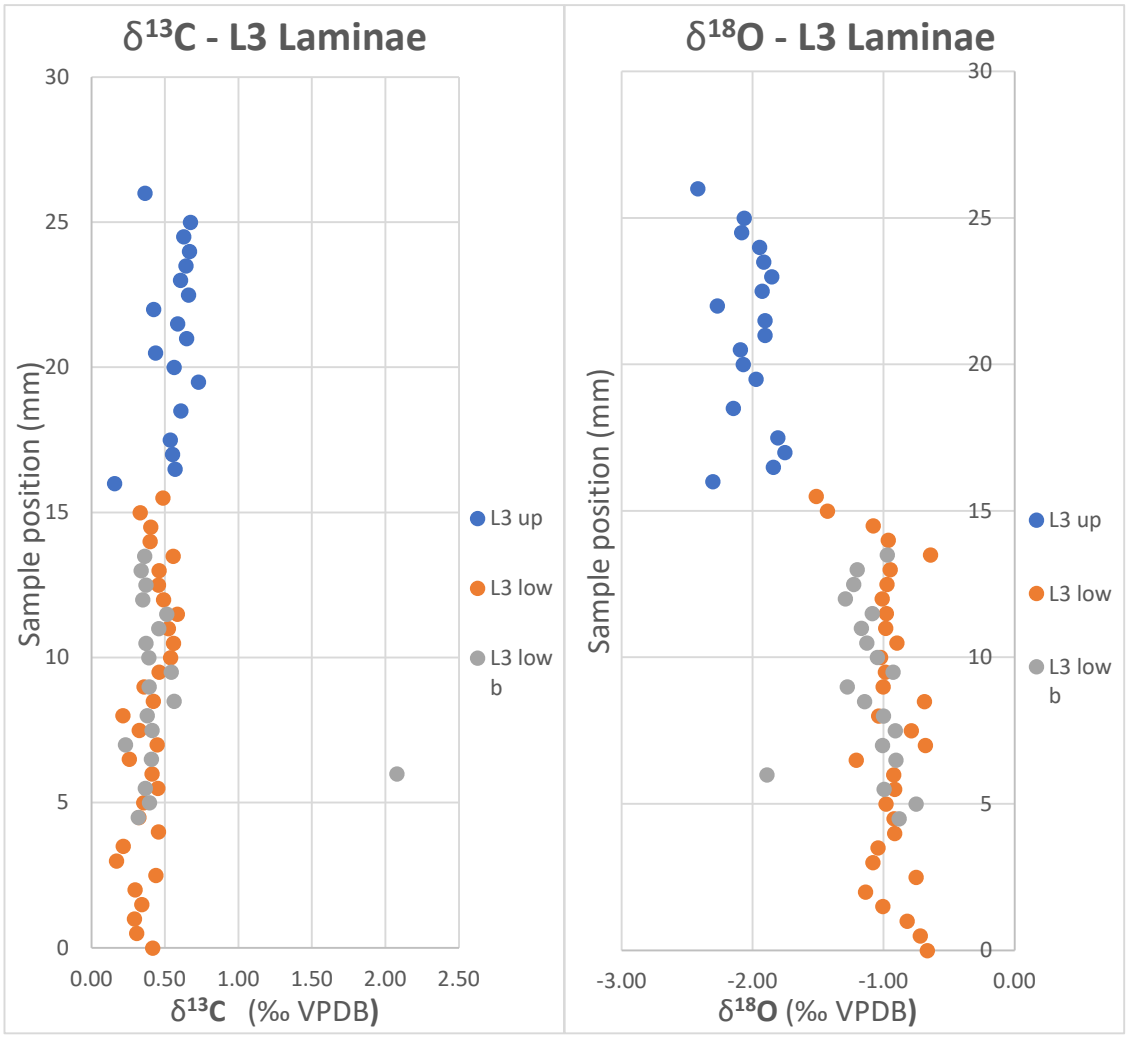

Figure 4.23 Stable isotope composition for carbon and oxygen, according to the sample stratigraphic position, of the stromatolite laminae within L3. Different categories indicate different set of laminae according to their distance from the base of L3. L3 low b indicates a separate set of laminae covering only the lower part of L3.

4.3.10 Summary of carbon and oxygen isotope values within the specimen.

Figures 4.24 a, b summarise, respectively, the ranges of carbon and oxygen isotope values for all main facies within the specimen. Figure 4.25 and Figure 4.26 show, respectively, the carbon and oxygen isotope values of all facies of the specimen. Figure 4.27 and Figure 4.28 show, respectively, the carbon and oxygen isotope values of all facies of the specimen with a moving average trendline with data averaged over five samples to show trends more clearly.

The total range of carbon isotope values is about 4‰ VPDB, although most of the data are within 2‰ VPDB (–1‰ to 1‰ VPDB). The highest carbon isotope values are found in the thrombolite layer, below L1, and in the upper micritic layer below the thrombolites, where the maximum value measured is 1.1‰ VPDB. The minimum value measured for carbon isotopes is –3.00‰ VPDB within the dendrolite structures of D1, followed by – 0.6‰ VPDB within the correspondent sediment fill. L1 is the facies with the widest and lowest carbon isotope values. Low values of $\delta^{13}C$ were also found in the third depression series of L2, up to –2.0‰ VPDB.

The total range of oxygen Isotope values Is about 7.5‰ VPDB, although most of the data are within 2.5‰ VPDB (Figure 4.26). The oxygen isotope values are all negative and the highest value was close to 0.0‰ VPDB found in L1. The lowest oxygen isotope values were found within the sediment fill of D1, –7.5‰ VPDB, and –7.1‰ VPDB of the dendrolites of D1.

Carbon isotope values have a positive trend in the lower facies of the Upper Cotham Member up to the thrombolites. Oxygen isotope values have a positive trend in the lower facies of the Upper Cotham Member up to the lower stromatolite laminae, L1. Within the Cotham Marble facies, L1 and L2 tend to have lower carbon and higher oxygen isotope values (in particular the median values) than the subsequent dendrolitic facies, respectively.

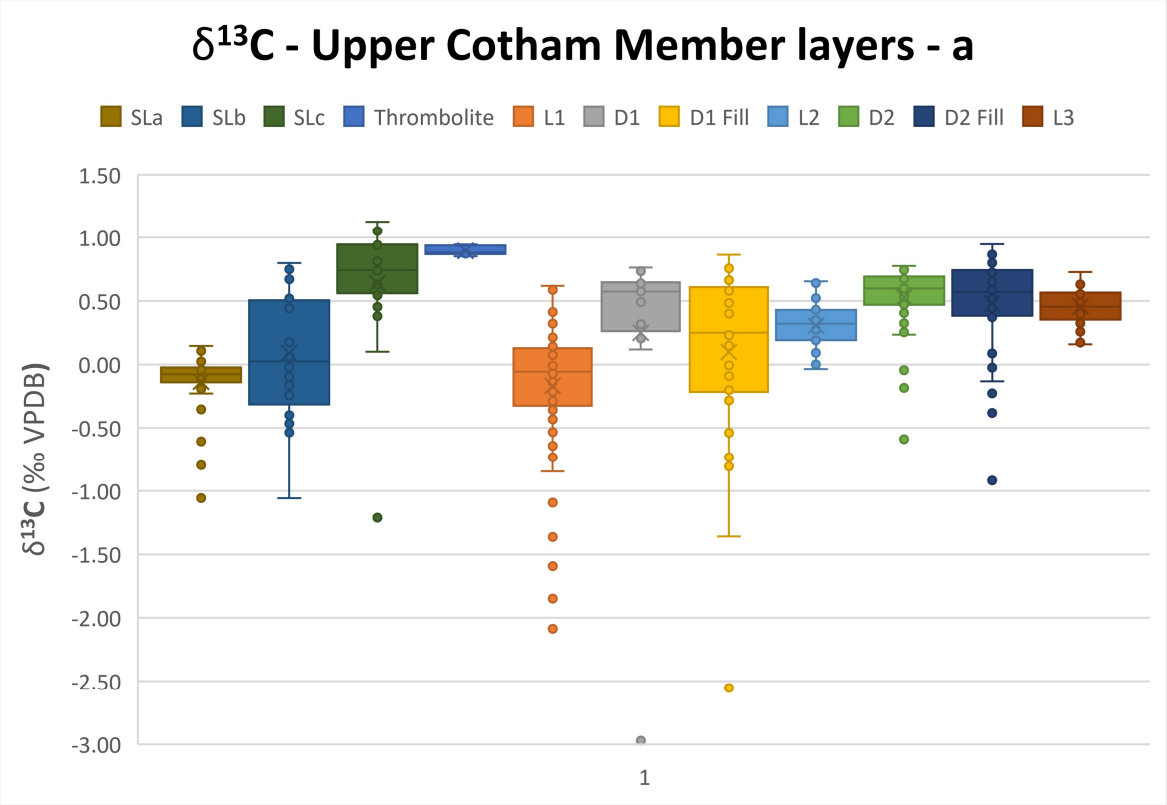

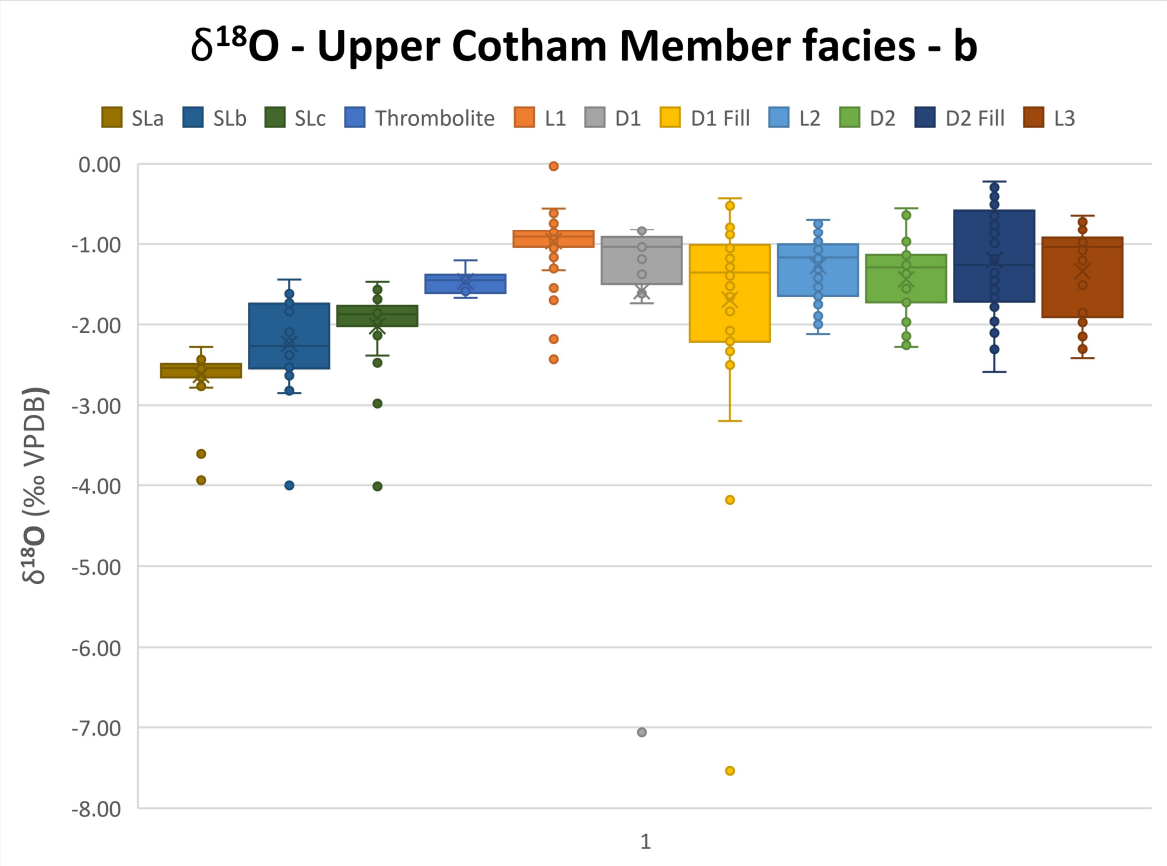

Figure 4.24 Box and whisker plot for carbon (a) and oxygen (b) isotope values of all facies in the specimen. Whiskers and box boundaries indicate from bottom: minimum, first quartile, median (segment inside box), mean (x), third quartile (upper box segment) and maximum values. The data outside the minimum and maximum are outlier data (statistically excluded by the Excel algorithm).

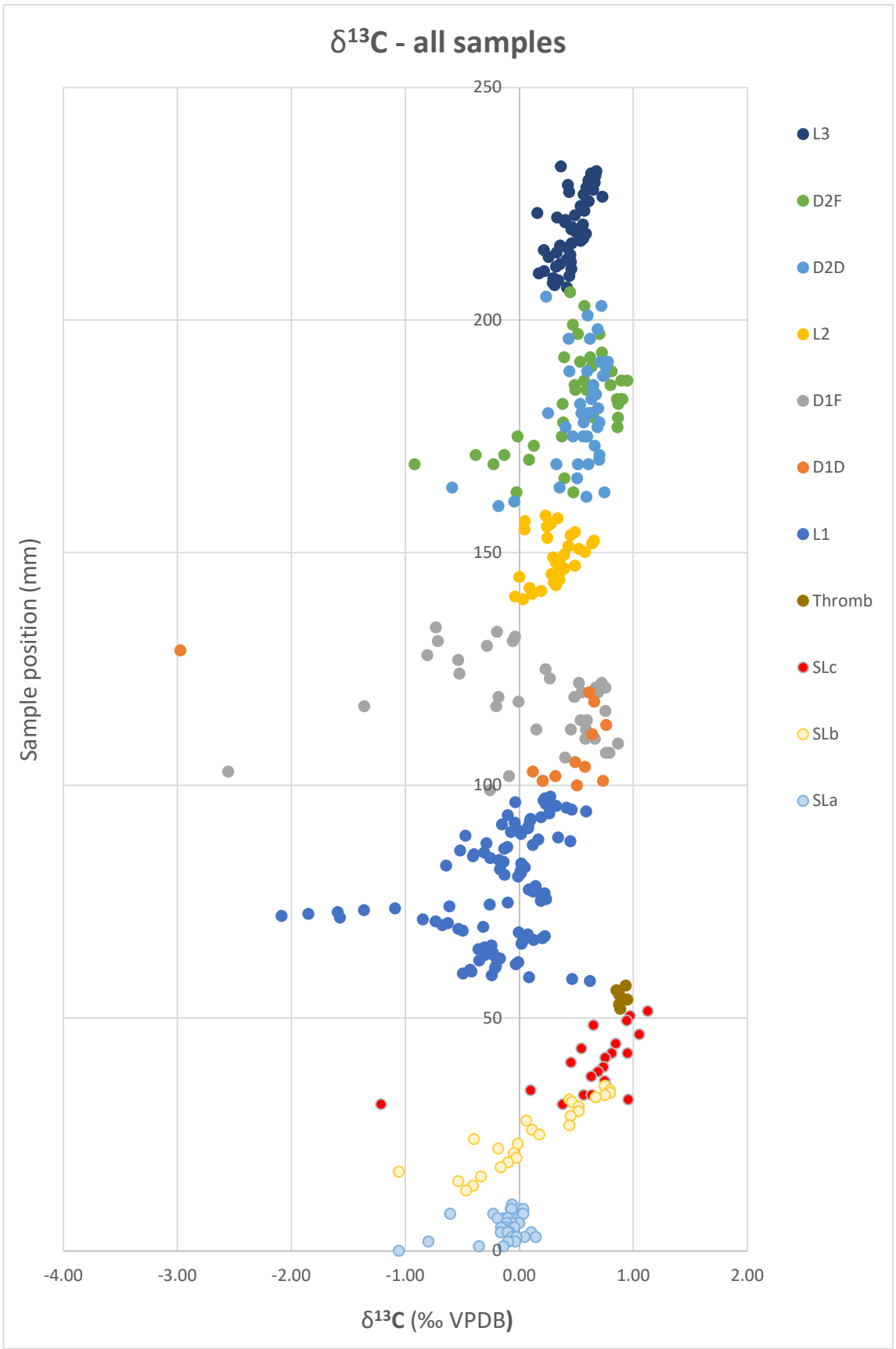

Figure 4.25 Stable isotope composition for carbon according to the sample stratigraphic position of all facies.

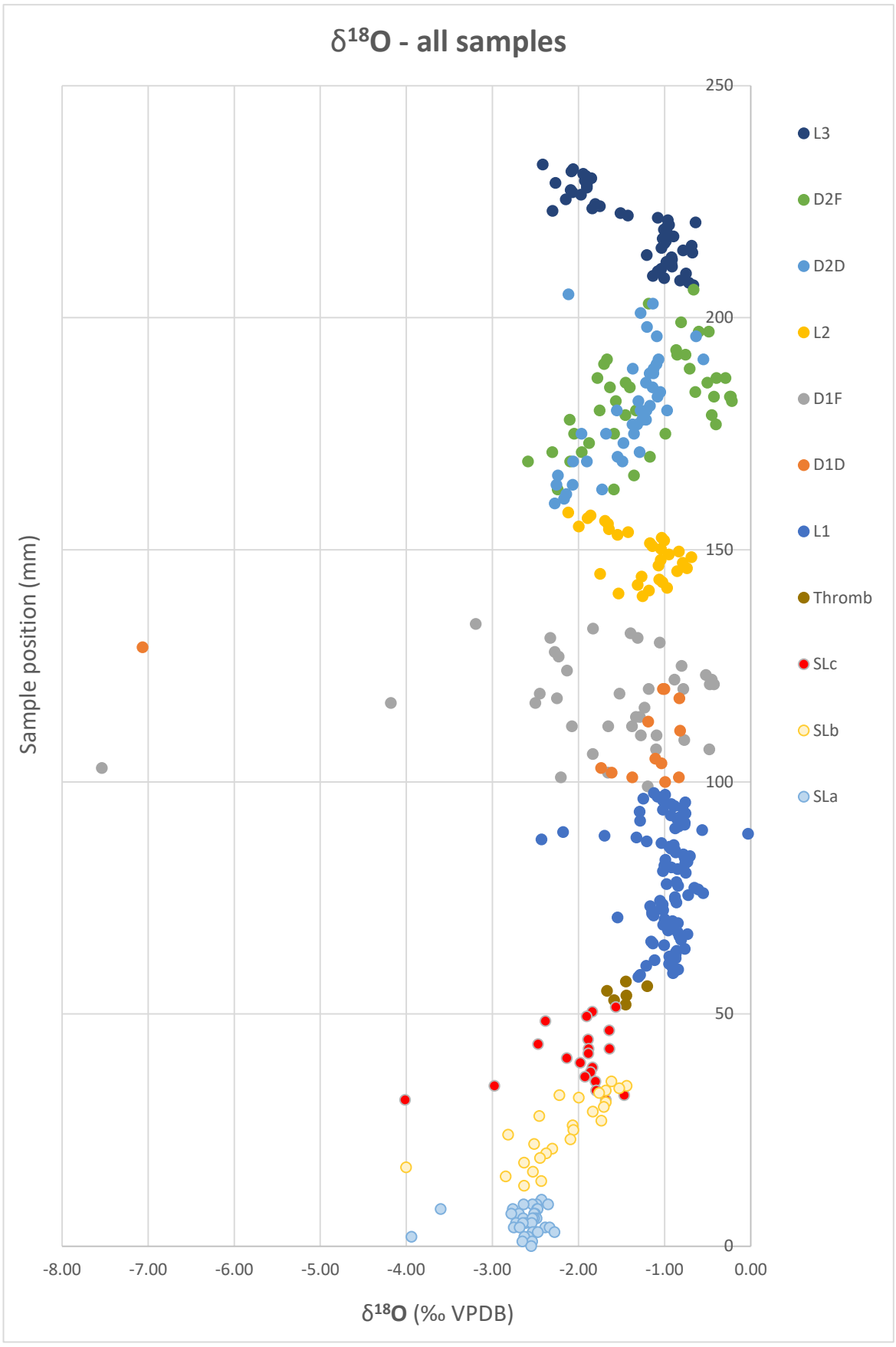

Figure 4.26 Stable isotope composition for oxygen according to the sample stratigraphic position of all facies.

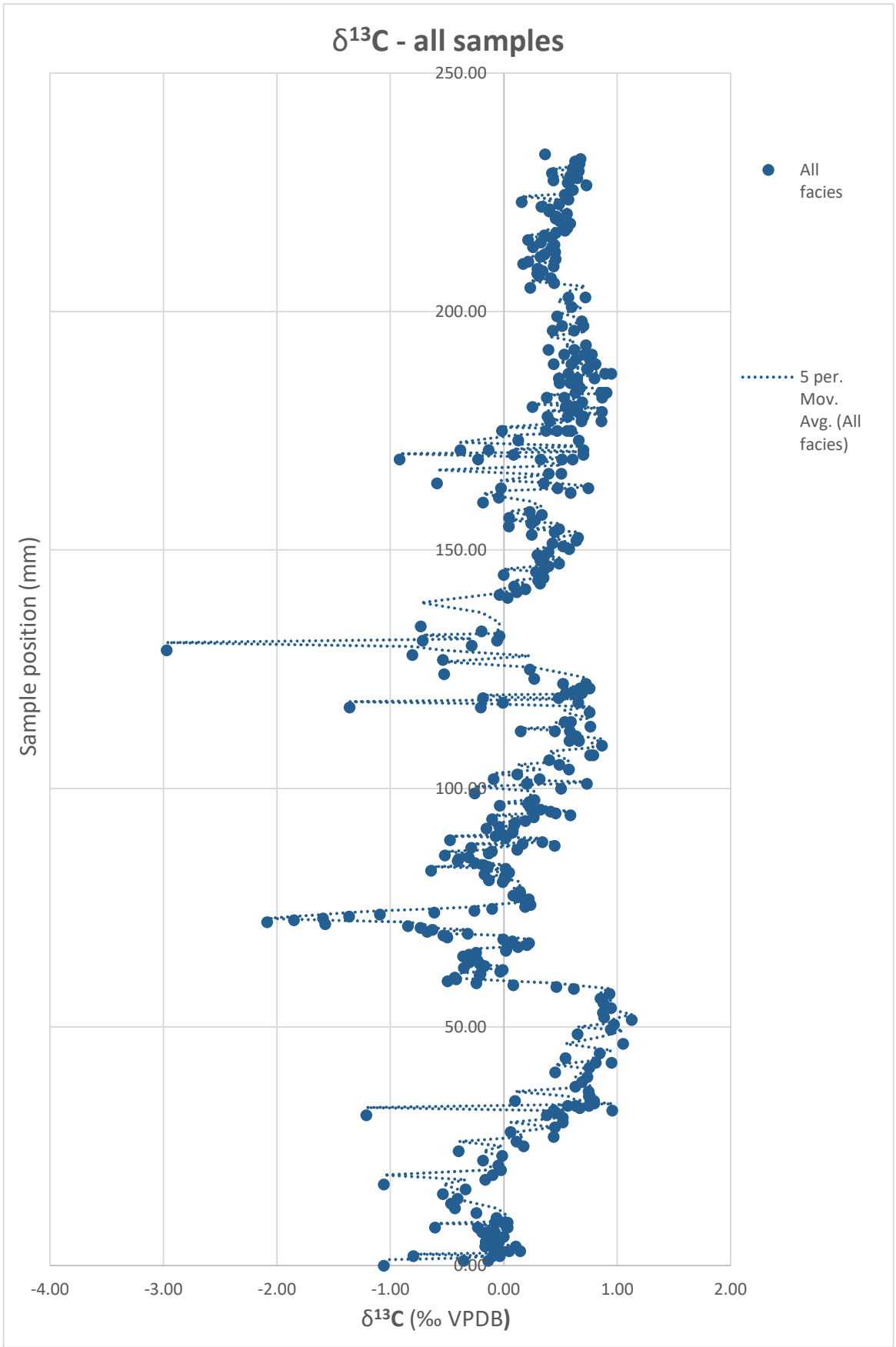

Figure 4.27 Stable isotope composition for carbon according to the sample stratigraphic position of all facies, with a moving average trendline with data averaged over five samples.

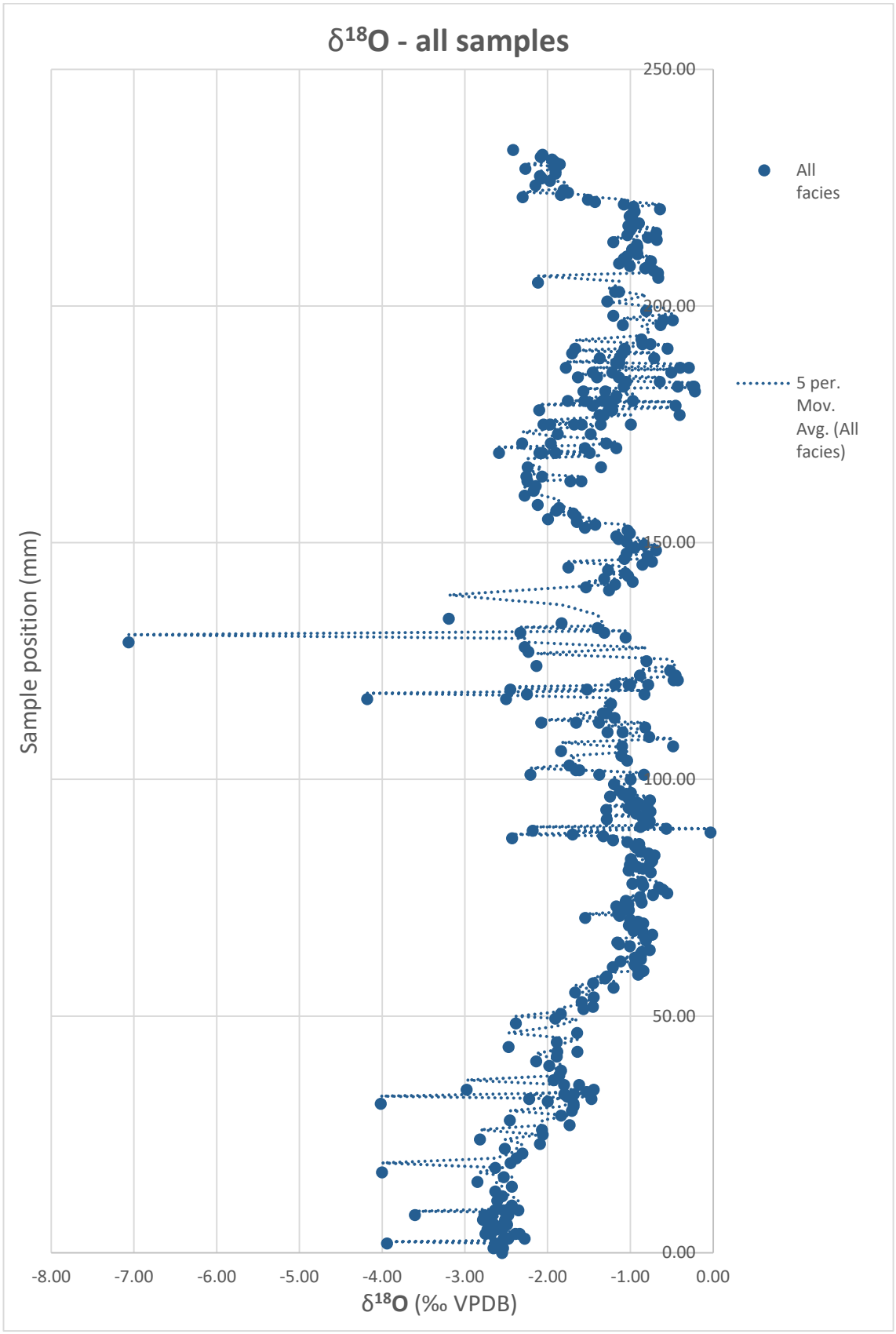

Figure 4.28 Stable isotope composition for oxygen according to the sample stratigraphic position of all facies, with a moving average trendline with data averaged over five samples.

CHAPTER 5

Discussion and conclusions

5.1 Clumped isotope analyses.

The coolest Δ_{47} -derived temperatures (+4.4 ±5.8 to +11.5 ±4.7 °C) are in the micritic layers of the Upper Cotham Member below the Cotham Marble. The laminated stromatolite facies (L1, L2, and L3) mainly formed at Δ_{47}-derived temperatures between +12.9 ±4.7°C and +26.7 ±4.1°C. The widest range of temperatures for the stromatolite laminae was recorded within L1, with a marked difference between the lower and grey set of laminae (ca. +13 to +15°C) and the upper set of laminae (ca. +27°C). The dendrolite facies formed at temperatures between +14.6 ±4.7°C and +24.8 ±4.1°C, with cooler temperatures in the first dendrolite facies.

The difference in temperatures found in two samples of sediment fill in D2 (+15.2 ±4.1°C and +23 ±4.7 °C) may be real or could be an artefact of differential cementation. As the $\delta^{13}C$ and $\delta^{18}O_{CARBONATE}$ values of sample CM-D2f (Table 4.1) are lower than those of the other microbialite micrites, and closer to those of cross-cutting vein-hosted sparry calcites, it is possible that the area from which the sample was drilled may have been contaminated by larger amounts of cementing sparry calcite. This noted, the cooler Δ_{47}-derived temperatures of a spar contaminated sample would not be expected, raising the possibility that an earlier, pre-fracture, phase of cementation was involved. So far light and cathodoluminescence microscopy has not been diagnostic on this possibility. This issue is re-examined in discussion of the depressions in the L2 laminar stromatolites in section 5.2.2.2.

The lowest temperature found In the Upper Cotham Member non-microbialite facies (+4.4 ±5.8°C), from a thin, grey, micritic layer overlying the thrombolite layer also seems anomalous. Inspection of the $\delta^{13}C$ and $\delta^{18}O_{CARBONATE}$ replicates of this sample (CM-c: Table 4.1) shows that, while the $\delta^{13}C$ values are close, there is a large difference (ca. 0.5‰) between the $\delta^{18}O_{CARBONATE}$ values, not observed in the repeats of other

samples. A difference in $\delta^{18}O_{CARBONATE}$ but not in $\delta^{13}C$, is probably caused by re-equilibration of oxygen isotopes between the evolved carbon dioxide and the water vapour produced during acid digestion of the carbonate (P. Dennis, pers. comm., 2023).

$CaCO_3 + H_3PO_4 \rightarrow CO_2 + H_2O$
$CO_2 + H_2O \leftrightarrow H_2CO_3$

While the carbon isotope composition is transferred from the carbonate to the carbon dioxide, the oxygen isotopes from the carbonate are susceptible to exchange between carbon dioxide and water, altering the real isotope composition of the carbonate. At the same time, it is likely that the Δ_{47} value of the CO_2 is also partially re-equilibrated ($\Delta_{47\ 1} = 0.640 \pm 0.018$, $\Delta_{47\ 2} = 0.678 \pm 0.018$;), explaining the cooler temperature.

It is not possible to determine which analysis to reject without measurements of further replicates. However, the temperatures calculated for each of the replicates individually are $T_1 = +9.8 \pm 5.8°C$ and $T_2 = -0.8 \pm 5.8°C$ which suggests that T_1 most closely approximates the actual temperature of deposition. In support of this, the associated Upper Cotham Member micrites (Table 4.1) also returned Δ_{47}-derived temperatures between +8 and +12°C suggesting that depositional temperatures were cooler at this time than during deposition of the overlying Cotham Marble.

A few other samples, such dendrolite D2d, and the upper lamina of L1 (L1up), also have $\delta^{18}O_{CARBONATE}$ replicates with around 0.4-0.5‰ differences. This might be explained by re-equilibration of oxygen isotopes or might reflect heterogeneity in the sample powder resulting from accidental mixtures of microfabrics during drilling (e.g. mixture of dendrolite micrite with sediment fill).

Overall, the Δ_{47}-derived temperatures reported here do not support the presence of distinct, alternating, lower (dendrolites) and higher (laminated stromatolites) temperatures in the Cotham Marble microbialites (Petryshyn et al. 2020). They claimed that dendrolitic layers formed at temperature of +13.1 ± 3.6 °C (SD), while the laminated layers formed at +29.6 ± 4.7 °C (SD), a difference of 16.5°C between facies types. This difference was attributed to strong seasonality of end Triassic climate. The new data presented show no trend in temperatures in the Cotham Marble microbial facies, and critical reassessment of the clumped isotope data in (Petryshyn et al. 2020) by Prof. P. Dennis casts significant doubt on the veracity of the older data.

The reassessment of the data reported In Petryshyn et al. found that the Incorrect application of the Δ_{47}-temperature calibration resulted in too high temperatures; the equation to calculate temperatures, derived by Bernasconi et al. (2018) for a 25°C carbonate reaction, was erroneously attributed to a temperature of reaction of their carbonate samples of 90°C (P. Dennis, pers. comm., 2022).

However, Δ_{47}-derived temperatures calculated with three different equations with correct parameters for a 90°C reaction (Bernasconi et al., 2018; Dennis et al., 2019; Anderson et al., 2021) show low values (< 10°C) in the majority of the facies and negative values in some cases; negative temperatures are not plausible and suggest that the clumped isotope data themselves may have been affected by contamination (P. Dennis, pers. comm., 2022). Inspection of Δ_{48} data reported in Petryshyn et al. reveals a significant number of samples with markedly positive Δ_{48} values measured with respect to the working reference gas. This is an indication of contamination of the analyte CO_2, either as a result of contaminated samples or error during sample preparation.

It is however clear that Cotham Marble depositional temperatures were generally warmer (ca. +12 to +26°C) than those in the underlying thrombolite and non-microbial micrites (+8 to +12°C).

A source of uncertainty in using clumped isotope palaeothermometry to establish depositional temperatures is possible alteration at elevated temperatures. The solid-state diffusion of C and O atoms at temperatures above those common at Earth's surface can lead to reordering of C–O bonds in the calcite mineral lattice without changing its microstructure, thus altering the clumped isotope composition of the carbonate and the derived palaeotemperature (Henkes et al., 2014; Petryshyn et al., 2020). This is important in ancient sedimentary rocks, such as these Triassic ones, because post-depositional burial can lead to temperatures elevated enough to affect the isotopic compositions of limestones. According to Henkes et al. (2014), on timescales of 10^6-10^8 years, appropriate for the burial history of these Triassic formations, reordering commences when the mineral undergoes heating at 100 °C and in 10^8 years, a burial temperature of 150 °C, corresponding to a burial of 5-6 km, is sufficient to reorder completely a calcite. However, if the burial temperature remains under 100 °C calcite undergoes little or no-reordering, even on geological timescales (Henkes et al., 2014).

Data on maximum burial temperatures of the Rhaetian at Wickwar are not easily determined because the sediment cover from Jurassic and Cretaceous is unknown. Palaeotemperature reconstruction from apatite fission-track and vitrinite reflectance data in Green et al. (2001) indicate that Rhaetic sediments from the Apley Barn Borehole near Witney (about 65 km ENE of Wickwar) reached burial temperatures of around 60-70 °C. Further data inferred from burial temperatures (< 50 °C) of Callovian (Middle Jurassic) sediments at Cleveland Farm gravel pit near Cricklade (about 35 km from Wickwar) and assuming a further cover of 200-300 m of Lower and Middle Jurassic sediments with a geothermal gradient of 30°C/km, indicate that Rhaetic sediments may have reached burial temperatures of around 60°C (J. Andrews, pers. comm., 2023). Therefore, we can be reasonably confident that the Upper Cotham Member sediments did not reach burial temperatures of more than 70°C. The single analysis of a post-brittle-fracture, vein-fed, sparry calcite is concrete evidence that burial fluids precipitated at temperatures around 34°C, but the timing of this event is not known and could significantly post-date maximum burial.

Overall, the clear differences in temperatures measured (Table 4.1) are not consistent with homogenisation of Δ_{47} values: similar reasoning was used by Petryshyn et al. (2020) in their earlier study of these rocks.

5.1.1 Clumped isotopes and depositional water compositions.

If it is accepted that global mean Rhaetian seawater had a $\delta^{18}O$ close to 0‰ VSMOW (Korte et al., 2005) then coastal seawater in the SW England area probably had a similar or slightly more negative (? –1‰ VSMOW) composition due to freshwater inputs from rivers. The $\delta^{18}O$ water compositions calculated from the clumped isotope data for the lower facies of the Upper Cotham Member within the specimen are between –2 and –4‰ VSMOW (Table 4.1) suggesting that the lagoons had a strong component of meteoric-derived river water, which at low latitude would be expected to have $\delta^{18}O$ compositions around or below –4‰ VSMOW, based on modern latitudinal precipitation mapping (Darling et al., 2005). The lagoon water of the Cotham Marble microbialites, calculated from the clumped isotope data had $\delta^{18}O$ compositions between –1 and +2‰ VSMOW which are either of marine origin, or evaporated, lower salinity water: a marine component was very likely as the presence of gypsum pseudomorphs in L1 and rare marine bioclasts (Ibarra et al., 2015) suggest at least episodic wash-in of seawater.

The carbon isotope composition of inorganic carbon in Rhaetic seawater is suggested to have been around +2‰ VPDB (Korte et al., 2005) and on this basis the environmental variability in $\delta^{13}C$ in the Cotham Member limestones, between +1 and –1‰ VPDB (discussed below), probably indicate some input of isotopically negative soil water from continental runoff into the lagoons.

5.2 Bulk isotope analyses.

The bulk isotope data allow a higher resolution analysis of the microfabrics under study. The data are overall similar to those in Ibarra et al. (2016) who presented sparse data from a few sites, and the data from Wickwar undertaken by Cushing (2018) in a UEA undergraduate project. When combined with the clumped isotope information on water oxygen isotope compositions and water temperatures, the high-resolution stable isotope data can be used to set limits of likely variation in temperature and/or water compositions at the micro-scale. Moreover, the carbon isotope compositions inform on carbon sources to the lagoon system as recorded by the isotopic composition of the dissolved inorganic carbon (DIC) which is closely related to the carbonate $\delta^{13}C$.

The total range In $\delta^{18}O$ is about 7.5‰ (between (0.0 and –7.5‰ VPDB), although most of the values are within 2‰ (between –2.5 and –0.5‰ VPDB). $\delta^{18}O$ below –2‰ mostly vary positively with $\delta^{13}C$ (Figures 4.9, 4.14, and 4.18) and in many cases these negative values (outlier points) are indicative of incorporation of sparry calcite cement into the sample (inferred from the end-member composition of the clumped isotope data on fracture filling sparry calcite). For interpretation of Rhaetic lagoonal conditions, it is thus possible to largely discount Cotham marble $\delta^{18}O$ and $\delta^{13}C$ values below ca. –2 and –1 ‰ VPDB respectively; in the Upper Cotham Member below the microbialites (Figure 4.11) the data distribution suggests the cut-off for spar contamination may be lower, ca. –3 and –0.5 ‰ VPDB respectively.

The total range in $\delta^{13}C$ values is about 4‰ (between +1.1 and –3.0‰ VPDB), although many of the values below –1‰ are due to sparry calcite contamination (as above). Thus most of the environmental variability in $\delta^{13}C$ is in a range between +1 and –1‰ VPDB. An important exception is a negative spike in $\delta^{13}C$ down to –2‰ VPDB in L1 (Figure 4.13) which does not co-vary with $\delta^{18}O$ and is interpreted as an environmental signal (discussed below).

5.2.1 Upper Cotham Member.

The Δ_{47} data for these beds, never before studied isotopically, suggest non-marine lagoon water with water $\delta^{18}O$ between –2 to –4‰ and temperatures between 8 and 12°C. The higher resolution $\delta^{18}O$ data show steadily increasing values from around –2.5‰ at the base to –1.2‰ VPDB (Figure 4.11). The basal layers (Sla and SLb) may be in part contaminated with sparry calcite cement that fills former aragonitic shell moulds. If we discount the more negative stable isotope values from these layers, there is still a steady increase in $\delta^{18}O$ from around –2.0‰ at 25 mm sample depth to –1.2‰ VPDB (Figure 4.11) at the top. This change could be recording steadily decreasing water temperature, or increasing evaporation or input of seawater. While it is not possible to be diagnostic on these options, a decrease in temperature seems less likely as the values stabilise in the lower part (L1) of the Cotham Marble (Figure 4.13), where the Δ_{47}-derived temperatures are between 13-15°C and continue rising, to 27°C into the top layers of L1 (Table 4.1). It thus seems more likely that lagoon water temperatures were becoming warmer but also more evaporated/saline in the transition into the basal Cotham Marble. An increase of 1.5‰ in water $\delta^{18}O$ would readily explain the change seen in $\delta^{18}O_{CARBONATE}$ values. Similar arguments have been made to explain Scottish Middle Jurassic lagoonal $\delta^{18}O$ variability ranging between –1 and –5‰ VSMOW (Holmden & Hudson, 2003).

The $\delta^{13}C$ data show an upward progression from values around 0 to 0.9‰ VPDB (Figure 4.11). These values are much less affected by minor contamination from sparry calcite in former shell moulds: if assumed to form under near equilibrium conditions, the values are not dissimilar to those seen in marine carbonates today and are probably indicative of lagoon DIC derived from either seawater sources or weathering sources brought to the lagoons by rivers which were dissolving limestones in their catchments. The increase in values upward is consistent with the notion of lagoon water steadily evaporating under increasing residence times. The positive co-varying trend in $\delta^{13}C$ and $\delta^{18}O$ corroborates this interpretation and may indicate that the lagoons were becoming more closed from open marine influence. Similar isotopic covariation has been observed in Middle Jurassic lagoonal carbonates from Scotland (Holmden and Hudson, 2003); here DIC $\delta^{13}C$, recorded in shell carbonates, had values between +1 and +2.5‰ PDBVPD, the higher values reflecting waters with longer residence times and fuller equilibration with atmospheric CO_2.

It Is worth noting that the Isotopic composition of the thrombolite layer In the Upper Cotham Member (Figure 4.11) is not much different to the micrites immediately below. Thus despite the presence of an erosive contact at the base of the thrombolite, it formed in lagoonal conditions broadly similar to the beds below. The rather fragmented appearance of the thrombolite elements, set in a fine micritic matrix, may be a result of storm conditions that disturbed the overall laminar disposition of the lower beds.

5.2.2 Cotham Marble Stromatolite facies

5.2.2.1 Stromatolite L1

The Δ_{47} data for L1 suggest lagoon water with $\delta^{18}O$ compositions variably between -1 and +2‰, and with water temperatures between 13 and 27 °C. The $\delta^{18}O$ compositions allow marine input to the lagoons and the presence of gypsum in L1 confirms its likely presence, at least sporadically. The overall picture seems to be a warm, evaporating quasi-marine, lagoonal mudflat. The higher resolution $\delta^{18}O$ data (Figure 4.13) show L1 lamina by lamina fluctuations of around 1‰ around a central value of ca. –1‰ VPDB. This variability could be driven by either small changes in water temperature or water $\delta^{18}O$, or a combination of the two. Layer (i.e. set of laminae) L1m (Figure 4.13) shows remarkably variable $\delta^{18}O$ between –2.4 and 0 ‰ VPDB which is probably explained by the presence of micro-sparry cement (the $\delta^{13}C$ values are also quite variable).

The L1 $\delta^{13}C$ values are markedly lower, but mostly around a central value of ca. 0‰ VPDB, than those in the underlying thrombolite (Figure 4.13). The values fluctuate lamina by lamina by around 1‰ but do not co-vary with $\delta^{18}O$ ($R^2 = 0.04$). The 1‰ decrease in $\delta^{13}C$ near the base of L1 suggests the lagoon DIC contained more isotopically light carbon, and it may be that this was related to either increased runoff with a soil carbon component, or increased availability of organic carbon related to the establishment of the microbial mats. These issues will be discussed further (Section 5.3 5.2.2.2) in relation to the most remarkable feature of the L1 $\delta^{13}C$ record, a clear negative spike of around –2‰ in layer L1g (Figure 4.13) which is not accompanied by change in $\delta^{18}O$.

The L1 data compare well with those In Ibarra et al. (2016), their Lower Wood data being from the Wickwar site. Their lowest L1 $\delta^{13}C$ from Stowey Quarry is similar to that

presented here and may be tentative evidence that the L1 negative $\delta^{13}C$ excursion at Wickwar will be found at other sites.

5.2.2.2 Stromatolites L2 and L3

The single Δ_{47}-derived temperatures in L2 and L3 are between 20-25 °C, within error of one another and with most of the Δ_{47}-derived temperatures in L1. Similarly the lagoon water $\delta^{18}O$ compositions are between 0.5-0.8‰ VSMOW similar to the upper layers of L1. The higher resolution stable isotope data (Figures 4.17 and 4.23) are remarkably constant and with values broadly similar to those in L1. Only the upper laminae in L3 shows a clear step down in $\delta^{18}O$ by around 1‰, which could reflect warming water temperatures, or perhaps more likely, the presence of less saline or less evaporated water.

The L2 and L3 data are generally comparable with equivalent values In Ibarra et al. (2016) excepting the L2 $\delta^{13}C$ values; these are mostly more negative in the Ibarra et al. (2016) data than those presented here and in Cushing (2018).

Depressions in L2.

Depressions in stromatolitic laminae are inherited by the morphological adaptation of the stromatolites to the underlying dendrolite topography. Isotopic investigation of the depression cavities was used to better understand their character and how these features relate to the surrounding facies. The first two sample series (L2Dep A and L2Dep B) were drilled from a depression that is not obviously filled by sediment or by sparry calcite cement. The $\delta^{18}O$ and $\delta^{13}C$ values for these depression samples are more or less identical to those of the equivalent horizontally bedded laminae (Figure 4.19) and this confirms that the feature is simply a depression in the laminae not filled by additional sediment, brought about by the morphology inherited from the underlying dendrolites.

A third (L2Dep C) series was drilled from a different L2 depression and here (Figures 4.18 and 4.19) the data show a striking covariant trend ($R^2 = 0.95$) to markedly negative values in the upper part of the depression. These negative values, down to –4‰ for $\delta^{18}O$ and –2‰ for $\delta^{13}C$ are exactly as expected for increasing sparry calcite cement presence (based on the clumped isotope data for the fracture-hosted sparry calcites) and suggest that the upper part of the depression contains silty sediment from the overlying D1 layer (see below), rich in microsparitic cement.

5.2.2.3 Cotham Marble Dendrolite facies (D1 and D2)

The Δ_{47} data for the dendrolite facies (D1 and D2) suggest lagoon water with $\delta^{18}O$ compositions mostly between 0 and 1‰ VSMOW, and with water temperatures between 18 and 25 °C, the more saline/evaporated and warmer conditions in D2. The $\delta^{18}O$ compositions again allow marine input to the lagoons, but evaporation may also be influencing water compositions. Overall the data are not distinctly different to the stromatolitic facies (L1-L3) and broadly the high resolution stable isotope data are also similar. It is worth noting that the $\delta^{18}O$ and $\delta^{13}C$ co-vary strongly, especially in D2 (R^2=0.78 for the sediment fill and R^2=0.99 for the dendrolite structures; Figure 4.20). This is consistent with the presence of variable amounts of microsparitic cement that are difficult to avoid during drilling. This suggests that the least negative $\delta^{18}O$ and $\delta^{13}C$ values are closest to Rhaetic environmental parameters.

The Wickwar stable isotope data for D1 and D2 are generally comparable with equivalent values in Ibarra et al. (2016).

5.3 Negative carbon isotope spike in L1.

An initial negative carbon isotope excursion (I-CIE), first observed in organic matter in the St Audrie's Bay section of the Cotham Member (Hesselbo et al., 2004), has been interpreted as a globally significant, initial organic carbon isotope excursion (I-CIE) as the result of a massive flux of isotopically light carbon from exogenous sources into the atmosphere driven by volcanism of the Central Atlantic Magmatic Province (CAMP) and subsequently used as a possible marker for end of the Triassic and its associated mass extinction (Hesselbo et al., 2002). It is thus likely that such a perturbation would be present in stratigraphically equivalent limestone $\delta^{13}C$ records (inorganic carbon) although Ibarra et al. (2016) failed to locate it.

However, more recently, the attribution of a volcanic-driver for the SW England CIE has been challenged by Fox et al. (2020, 2022) who interpret the Cotham Member CIE as a relatively local effect caused by the emergence of microbial mats, influenced by influx of fresh to brackish waters, which provided isotopically light carbon to both the organic carbon and inorganic carbon pools, in very shallow waters.

The data presented in this study suggest that the I-CIE may be present in the inorganic carbon record of the Cotham Marble L1 where the 2‰ negative $\delta^{13}C$ spike is of the

correct sign and magnitude. The $\delta^{13}C$ values either side of this spike are around 0‰, a distinct 1‰ decrease relative to the underlying Upper Cotham Member thrombolite. This, while not diagnostic, supports the suggestion by Fox et al. (2020, 2022) that the L1 lagoon DIC was receiving more isotopically light carbon, and it may be that this was related to either increased runoff with a soil-zone carbon component, or increased availability of organic carbon related to the establishment of the microbial mats; rapid intensification of such mechanisms could explain the I-CIE.

5.4 Palaeoenvironmental inferences and modern microbialite analogues.

Modern microbialite environments in the Persian Gulf, Australia, and California (Chapter 2) provide potential analogues model for the microbialite features of the Cotham Marble and their paleoenvironmental context.

Earlier work on the Cotham Marble identified domal microbial growth structures (Wright and Mayall, 1981). The formation of laminar stromatolites is consistent with conditions of sea level still-stands over vast areas where frequent flooding (such as the diurnal tidal flooding of the coastal sabkha in Abu Dhabi) allowed growth of polygonal/domal microbial mats. Frequent exposure combined with generally harsh environmental conditions may have inhibited competition from grazing metazoans, another condition for undisturbed microbial growth (Paul et al., 2021). The space between domes may have been a morphological adaptation to facilitate drainage during flooding events. The hypothesis of exposure is also consistent with the presence of desiccation surfaces, such as those apparent at the level of the microdigitate features that could be evidence of burrowing by small organisms appearing during drier periods.

The growth of dendrolite microbialites and the graded deposition of fine sediment around them is consistent with hydrodynamic conditions of prevalent or constant inundation, such as the case of modern microbialites growing in intertidal pools in Shark Bay (W Australia; Suosaari et al., 2018). Here, dendrolites grow over stromatolite mats, as they also do in geothermal pools in the Long Valley Caldera of California (Bradley et al., 2017). These authors found that the microbes were actively fixing inorganic carbon in both the dendrolitic cone tips and the microbial mats, from warm pool waters supersaturated with respect to calcite. Thrombolites growing in immersed intertidal pools in Abu Dhabi (Paul et al., 2021) calcify due to high saturation with calcium carbonate

(Caumartin et al. 2023), a common chemical condition required for microbialite calcification worldwide.

Below the Cotham Marble, the depositional environment appears to have been characterised by low energy periods interrupted by high energy events. The latter resulted in mixed micritic layers with shells, evidence of load casts, cross lamination, erosional scours and a partially disturbed thrombolite layer. It is possible the higher energy episodes decreased in frequency and intensity before the deposition of the Cotham marble microbialite facies, although presence of echinoid fragments in L1 still supports some storm wash-in.

Recent studies by Fox et al. (2020, 2022) imply the presence of a sea-level standstill for the formation of the Upper Cotham Member and the Lilstock Formation. Analysing isotopic and biogeochemical proxies in stratigraphic sections (St. Audrie's Bay and Lilstock) where the Cotham Marble facies are not present, Fox and co-authors found that the negative organic carbon isotopic excursion (CIE) was caused by the emergence of microbial mats, influenced by an influx of fresh to brackish waters, which provided isotopically light carbon to both organic and inorganic carbon pools, in very shallow water depths. Such shallow water depths resulted from an abrupt sea level drop that consequently led to the transition from a marine to a non-marine environment and to the disappearance of marine organisms (Fox et al., 2020).

According to Fox et al. (2020), the transfer of ^{13}C-depleted organic carbon associated with microbial mats to the inorganic carbon pool is through microbial respiration. Several authors (Andres et al., 2006; Nitti et al., 2012; Breitbart et al., 2018) suggest that depleted $\delta^{13}C$ values of the microbialite carbonate can only be explained through the addition of a ^{13}C-depleted source of carbon to the local DIC reservoir, rather than disequilibrium in the precipitation of the microbialites. Breitbart et al. (2018) suggests that respiration of ^{13}C-depleted photoautotrophic biomass by both aerobic and anaerobic heterotrophic organisms (i.e cyanobacteria, sulphate-reducing bacteria and aerobic heterotrophs) would release ^{13}C-depleted CO_2 to the DIC reservoir, resulting in a negative shift of the inorganic ^{13}C. Furthermore, Nitti et al. (2012) found that ^{13}C depletion in inorganic carbon must indicate the remineralisation of buried organic matter by anaerobic heterotrophic microbial community and subsequent incorporation of the ^{13}C-depleted carbon into CaCO3.

The facies transitions described from Wickwar are broadly consistent with the suggestion that regressive conditions promoted deposition of the lower facies of the Upper Cotham Member in cool, coast marginal lagoons of broadly non-marine character. The Cotham Marble microbialites developed during sea-level stillstand in quasi-marine, warm lagoons where evaporation was common and water residence times relatively long. Alternating exposure and inundation created the hydrodynamic conditions under which laminar stromatolites and dendrolites developed, respectively.

5.5 Further comments.

- We noted the presence of accretions of mm-scale sparitic pillow-like areas within the hedges of D1 at the top of L1 (Section 4.1.2). The radial and partly porous appearance of some of these pillow-like clumps suggests that they may have contained domains richer in organic material that acted as substrate for early diagenetic radial microspar. In other words, the areas now filled with the pillow-like sparitic accretions during deposition were probably filled with organic matter. When the organic matter decayed, its radial structure appearance was preserved by the calcite.

- CL shows that all micrites have bright orange luminescence, while late spars in veins and large void spaces have a dull brown luminescence. The CL colours show that the late spars both in veins and void spaces is co-eval, while microspars are clearly earlier than these veins fed spars which cross-cut them. In shelter cavities of articulated shells (Figure 4.3, c and d), the microspar alteration of micrites in geopetal sediment floors clearly predates the coarser void filling spar, and was formed by early diagenetic meteoric cementation/neomoiphism, a process that may have helped keep void space open during later burial.

5.6 Summary and conclusions.

1. The clumped isotope data show no trend in temperatures between the Cotham Marble microbial facies. The Δ_{47}-derived temperatures do not support the presence of a distinct pattern with alternating lower temperatures in the dendrolite facies and higher temperatures in the laminated stromatolite facies (Petryshyn et al. 2020), implying the presence of a strong seasonality of the end Triassic climate. However, the clumped isotope data show that Cotham Marble depositional temperatures were generally warmer (ca. +12 to +26 °C) than those in the underlying thrombolite and non-microbial micrites (+8 to +12 °C).

2. A distinct negative inorganic carbon excursion observed in this study in the first laminar stromatolites, L1, is consistent with the possibility that the growth of microbial mats provided isotopically light carbon as a result of microbial respiration, as identified by Fox et al. (2020) in the Upper Cotham Member. Further investigations are needed in the Cotham Marble at other localities to confirm the presence of the negative excursion at regional level. Furthermore, as the successive stromatolite phases, L2 and L3, returned positive carbon isotope values, as did the majority of the dendrolite samples and the thrombolite layer, it is not clear that the presence of microbialites directly determine negative inorganic carbon isotopic values.

3. The combined data on modern microbial analogues, clumped isotopes and high-resolution stable isotope analysis present the most complete picture of environmental conditions for deposition of the Cotham Marble. Overall, the data show that:

- The formation of laminar stromatolites is consistent with conditions of sea level still-stands over vast areas where frequent flooding, similar to the tidal flooding of the coastal sabkha in Abu Dhabi (Paul et al., 2021), allowed the growth of polygonal/domal microbial mats. Frequent exposure may have been a condition to inhibit competition from grazing metazoan and allow undisturbed microbial growth. The domal growth of the microbialites could be a morphological adaptation to facilitate drainage through the channels between the domes and therefore enhance exposure to inhibit competition from metazoan and/or improve environmental conditions for their growth.
- The hypothesis of exposure is also consistent with the presence of desiccation surfaces, such as those apparent at the level of the microdigitate features that could be evidence of burrowing by small organisms appearing during drier periods.
- The growth of dendrolite microbialites and the graded deposition of fine sediment around them is consistent with hydrodynamic conditions of prevalent or constant inundation, such as the case of modern microbialites growing in intertidal pools in Shark Bay in Australia (Suosaari et al., 2018) and in geothermal pools in the Long Valley Caldera of California (Bradley et al., 2017).
- High saturation with calcium carbonate of warm waters may have been a condition for the calcification of structures or the active fixation of inorganic carbon by microbial communities in dendrolites and microbial mats, as identified for microbial calcification worldwide (Caumartin et al., 2023).

- The depositional environment of the thrombolite and non-microbial facies underlying the Cotham Marble appears to have been characterised by low energy periods interrupted by high energy events, which resulted in mixed micritic layers with shells, evidence of load casts, cross lamination, erosional scours and a partially disturbed thrombolite layer. It is possible that the frequency and intensity of the high energy events decreased, thus allowing the formation of microbialites (thrombolites and then laminar stromatolites), although the presence of echinoid fragments in L1 still supports some storm wash-in.
- The facies transitions described above are broadly consistent with the findings by Fox et al. (2020) that the Upper Cotham Member and the Lilstock Formation formed during a sea-level standstill and under shallow water depths resulted from an abrupt sea level drop, that consequently led to the transition from a marine to a non-marine environment and to the disappearance of marine organisms. In such a context, regressive conditions promoted deposition of the lower facies of the Upper Cotham Member in cool, coastal marginal lagoons of broadly non-marine character. The Cotham Marble microbialites developed during sea-level stillstand in quasi-marine, warm lagoons where evaporation was common and water residence times relatively long. Alternating exposure and inundation created the hydrodynamic conditions under which laminar stromatolites and dendrolites developed, respectively.

5.7 Future work.

Future investigations should:

- attempt to verify the presence of the negative carbon isotope excursion in the lower stromatolite of the Cotham Marble at other sites to demonstrate regional significance or otherwise.
- better understand differences in isotopic values at different localities (e.g. Stowey Quarry in Ibarra et al., 2016), particularly in L2 and D2; and more generally, consolidate results across studies and sites for the Upper Cotham Member underlying the Cotham Marble, to solidify general palaeoenvironmental models for these upper Triassic deposits.

- identify how different types of analyses and palaeoenvironmental indicators can improve the understanding of the palaeoenvironmental conditions that surrounded the establishment of the Upper Cotham Member, such as trace elements and strontium

isotope analysis. The combination of clumped isotope with trace elements of Mn and Fe for example can help identify potential kinetic fractionation in ancient natural samples that resulted in apparent clumped isotope temperatures higher than environmental temperatures although mainly in calcitic veins (Herlambang and Cédric, 2020).

- compare results with stromatolites at global context to identify the existence of similar negative carbon isotope excursions due either to the microbialite presence or global geochemistry conditions.

References

Aitken, J.D., 1967. Classification and environmental significance of cryptalgal limestones and dolomites, with illustrations from the Cambrian and Ordovician of southwestern Alberta. *J. Sed. Petrol*., **37**, 1163–1178.

Allwood, A.C., Rosing, M.T., Flannery, D.T. Hurowitz, J.A., Heirwegh, C.M., 2018. Reassessing evidence of life in 3,700-million-year-old rocks of Greenland. *Nature*, **563**, 241–244. https://doi.org/10.1038/s41586-018-0610-4

Anderson, N., Kelson, J. R., Kele, S., Daëron, M., Bonifacie, M., Horita, J., Mackey, T. J., John, C. M., Kluge, T. & Petschnig, P., 2021. A unified clumped isotope thermometer calibration (0.5–1,100°C) using carbonate-based standardization. *Geophysical Research Letters,* **48**(7), e2020GL092069.

Andres, M., Sumner, D., Reid, R., and Swart, P. 2006. Isotopic fingerprints of microbial respiration in aragonite from Bahamian stromatolites. *Geology,* **34**, 973–976.

Andrews, J.E., 1986. Microfacies and geochemistry of Middle Jurassic algal limestones from Scotland. *Sedimentology,* **33**(4), 499-520.

Andrews, J.E., 2006. Palaeoclimatic records from stable isotopes in riverine tufas: synthesis and review. *Earth-Science Reviews*, **75**, 85–104.

Andrews, J.E., and Brasier, A.T., 2005. Seasonal records of climatic change in annually laminated tufas: short review and future prospects. *Journal of Quaternary Science*, **20**, 411–421.

Andrews, J.E., Riding, R., Dennis, P.F., 1997. The stable isotope record of environmental and climatic signals in modern terrestrial microbial carbonates from Europe. *Palaeogeography, Palaeoclimatology, Palaeoecology,* **129**, 171–189.

Arenas, C., Osácar, M.C., Auqué, L. and Sancho, C. 2019. Coupling textural and stable-isotope variations in fluvial stromatolites: Comparison of Pleistocene and recent records in NE Spain. Journal of Palaeogeography, **8**: 13.

Arp, G., Bielert, F., Hoffmann, VE. and Löffler, T. 2005. Palaeoenvironmental significance of lacustrine stromatolites of the Arnstadt Formation ("Steinmergelkeuper", Upper Triassic, N-Germany). Facies, **51**, 419–441. https://doi-org.uea.idm.oclc.org/10.1007/s10347-005-0063-8

Benton, M.J., Cook, E., Turner, P., 2002. Permian and Triassic Red Beds and the Penarth Group of Great Britain. *Geological Conservation Review Series*, No. 24, JNCC, Peterborough, ISBN 1 86 107 493 X.

Bernasconi, S.M., Daëron, M., Bergmann, K.D., Bonifacie, M., Meckler, A.N., Affek, H.P., Anderson, N., Bajnai, D., Barkan, E., Beverly, E., D. Blamart, L. Burgener, D. Calmels, C. Chaduteau, M. Clog, B. Davidheiser-Kroll, A. Davies, F. Dux, J.M. Eiler, B. Elliott, C. Fetrow, J. Fiebig, S. Goldberg , M. Hermoso, K.W. Huntington, E. Hyland, M. Ingalls, M. Jaggi, C.M. John, A .B. Jost, S. Katz, J. Kelson, T. Kluge, I.J. Kocken, A. Laskar, T.J. Leutert, D. Li ang, J. Lucarelli, T.J. Mackey, X. Mangenot, N. Meinicke, S.E. Modestou, I.A. Müller, S. Murray, A. Neary, N. Packard, B.H. Passey, E. Pelletier, S. Petersen, A. Piasecki, A. Schauer, K.E. Snell, P.K. Swart, A. Tripati, D. Upadhyay, T. Ven nemann, I. Winkelstern, D. Yarian, N. Yoshida, N. Zhang, M. Ziegler, 2021. InterCarb: a community effort to improve interlaboratory standardization of the carbonate clumped isotope thermometer using carbonate standards. *Geochem. Geophys. Geosyst*. **22**(5), e2020GC009588.

Bernasconi, S. M., Müller, I. A., Bergmann, K. D., Breitenbach, S. F., Fernandez, A., Hodell, D. A., Jaggi, M., Meckler, A. N., Millan, I. & Ziegler, M., 2018. Reducing uncertainties in carbonate clumped isotope analysis through consistent carbonate-based standardization. *Geochem. Geophys. Geosyst*. **19**(9), 2895–914.

Bradley, J.A., Daille, L.K., Trivedi, C.B., Bojanowski, C.L., Stamps, B.W., Stevenson, B.S, Nunn, H.S., Johnson, H.A., Loyd, S.J., Berelson, W.M., Corsetti, F.A., and Spear, J.R., 2017. Carbonate-rich dendrolitic cones: insights into a modern analog

for incipient microbialite formation, Little Hot Creek, Long Valley Caldera, California. *Npj Biofilms Microbiomes* **3** (32). https://doi.org/10.1038/s41522-017-0041-2

Brasier, A.T., Andrews, J.E., Marca-Bell, A.D., Dennis, P.F. 2010. Depositional continuity of seasonally laminated tufas: Implications for δ18O based palaeotemperatures. *Global and Planetary Change,* **71**, 160–167.

Brasier, A.T. 2011. Searching for travertines, calcretes and speleothems in deep time: processes, appearances, predictions and the impact of plants. *Earth Sci. Rev*., **104**, 213–239.

Breitbart, M., Hoare, A., Nitti, A., Siefert, J., Haynes, M., Dinsdale, E., Edwards, R., Souza, V., Rohwer, F., & Hollander, D. 2009. Metagenomic and stable isotopic analyses of modern freshwater microbialites in Cuatro Ciénegas, Mexico. *Environmental Microbiology*, **11**(1), 16–34.

Caumartin, J., Benzerara, K., Havas, R.,Thomazo, C., Lòpez-García, P., Duprat, E., 2023. The chemical conditions necessary for the formation of microbialites. *Geochem.Persp. Let*. **25**, 30–35. **https://doi.org/10.7185/geochemlet.2311**

Cushing, J., 2018. *Geochemical Analysis of the Cotham Marble*. Unpublished undergraduate research dissertation, School of Environmental Sciences, University of East Anglia. 63p.

Dabkowski, J., Limondin-Lozouet, N., Antoine, P., Marca-Bell, A., Andrews, J. 2011. Enregistrements des variations climatiques au cours des interglaciaires pléistocènes d'après l'étude des isotopes stables de la calcite des tufs calcaires. *Quaternaire*, **22** (4), 275-283.

Darling, W.G., Bath, A.H., Gibson, J.J., Rozanski, K., 2005. Isotopes in water. In: Leng, M.J. (Ed.), *Isotopes in Palaeoenvironmental Research*, Vol. 10 in Developments in Paleoenvironmental Research series, Springer, Dordrecht, pp. 1–66.

Defliese, W. F., & Lohmann, K.C., 2015. Non-linear mixing effects on mass-47 CO_2 clumped isotope thermometry: Patterns and implications. *Rapid Communications in Mass Spectrometry,* **29**(9), 901-909.

Dennis, K.J., Affek, H.P., Passey, B.H., Schrag, D. P., & Eiler, J.M., 2011. Defining an absolute reference frame for 'clumped'isotope studies of CO2. *Geochimica et Cosmochimica Acta*, **75**(22), 7117-7131.

Dennis, P.F., 2014. On the cause of mass spectrometer non-linearity during clumped isotope measurements. Figshare: https://doi.org/10.6084/m9.figshare.1254807.v1

Dennis, P.F., Vinen, S., Marca-Bell, A., & Rowe, P., 2014. MIRA: a new isotope ratio mass spectrometer for clumped isotope studies of CO2. Figshare: https://doi.org/10.6084/m9.figshare.899817.v1

Dennis, P.F., Myhill, D.J., Marca, A. & Kirk, R. 2019. Clumped isotope evidence for episodic, rapid flow of fluids in a mineralized fault system in the Peak District, UK. *Journal of the Geological Society*, **176**(3), 447– 461.

Eiler, J.M., 2007. "Clumped-isotope" geochemistry – the study of naturally-occurring, multiply-substituted isotopologues Earth Planet. Sci. Lett. **262**, 309-327.

Eiler, J.M., 2011. Paleoclimate reconstruction using carbonate clumped isotope thermometry. *Quaternary Science Reviews*, **30**(25-26), 3575-3588.

Eiler, J. M., & Schauble, E., 2004. $^{18}O^{13}C^{16}O$ in Earth's atmosphere. *Geochimica et Cosmochimica Acta,* **68**(23), 4767-4777.

Fairchild, I.J., Marshall, J.D., Bertrand-Sarfati, J., 1990. Stratigraphic shifts in carbon isotopes from Proterozoic stromatolitic carbonates (Mauritania): influences of primary mineralogy and diagenesis. *Am. J. Sci*., **290**-A, 46–79.

Fernandez, A., Müller, I. A., Rodríguez-Sanz, L., van Dijk, J., Looser, N., & Bernasconi, S.M., 2017. A reassessment of the precision of carbonate clumped isotope

measurements: Implications for calibrations and paleoclimate reconstructions. *Geochemistry, Geophysics, Geosystems*, **18**(12), 4375-4386.

Flannery, D.T.; Walter, M.R., 2012. Archean tufted microbial mats and the Great Oxidation Event: New insights into an ancient problem. *Aust. J. Earth Sci.*, **59**, 1–11.

Flügel, E. 1964. Mikroproblematika aus den rhätischen Riffkalken der Nordalpen. *Paläont. Z*. **38**, 74–87.

Fox, D., 2018. Cotham Marble, **https://researchworcestershire.wordpress.com/2018/08/24/cotham-marble/**

Fox, C.P., Cui, X., Whiteside, J.H., Olsen, P.E., Summon, R.E., Grice, K., 2020. Molecular and isotopic evidence reveals the end-Triassic carbon isotope excursion is not from massive exogenous light carbon. *PNAS*, **117**, 30171-30178

Fox, C.P., Whiteside, J.H., Olsen, P.E., Cui, X., Summon, R.E., Idiz, E., Grice, K., 2022 Two-pronged kill mechanism at the end-Triassic mass extinction. *Geology,* **50** (4): 448–453. Doi: https://doi- org.uea.idm.oclc.org/10.1130/G49560.1

Frantz, C.M., Petryshyn, V.A., Marenco, P.J., Tripati, A., Berelson, W.M. and Corsetti, F.A., 2014. Dramatic local environmental change during the Early Eocene Climatic Optimum detected using high res-olution chemical analyses of Green River Formation stromatolites. *Palaeogeography, Palaeoclimatology, Palaeoecology*, **405**, 1–15.

Gehler, A., and Reich, M., 2010. Founding of the Term 'Stromatolite': Ernst Louis Kalkowsky (1851–1938) and His Early Stromatolite Research. In: *Advances in Stromatolite Geobiology (eds J Reitner, NV Quéric, G Arp). Lecture Notes in Earth Sciences*, **131**, 3–11.

Ghosh, P., Adkins, J., Affek, H., Balta, B., Guo, W., Schauble, E. A., Schrag, D. & Eiler, J.M., 2006. 13C–18O bonds in carbonate minerals: a new kind of paleothermometer. *Geochimica et Cosmochimica Acta,* **70**(6), 1439-1456.

Grotzinger, J.P.; Knoll, A.H., 1999. Stromatolites in Precambrian carbonates: Evolutionary mileposts or environmental dipsticks? *Annu. Rev. Earth Planet*. Sci., **27**, 313–358.

Guo, W., Mosenfelder, J.L., Goddard III, W.A., & Eiler, J.M. 2009. Isotopic fractionations associated with phosphoric acid digestion of carbonate minerals: insights from first-principles theoretical 113esoprote and clumped isotope measurements. *Geochimica et Cosmochimica Acta,* **73**(24), 7203-7225.

Hamilton, D. 1961. Algal growth in the Rhaetic Cotham Marble of southern England. *Palaeontology*, **4**, 324–333.

Hamilton, D. 1977. Aust Cliff. In *Geological Excursions in the Bristol District (ed. R. J. G. Savage)*, pp. 110-19. University of Bristol Press.

Hamilton, D. and Whittaker, A. 1977. Coastal exposures near Blue Anchor, Watchet and St Audrie's Bay, Somerset. In *Geological Excursions in the Bristol District (ed. R. J. G. Savage)*, pp. 101-10. University of Bristol Press.

Herlambang, A., Cédric M. J. 2021. Combining clumped isotope and trace element analysis to constrain potential kinetic effects in calcite. Geochimica et Cosmochimica Acta, 296, 117-130, https://doi.org/10.1016/j.gca.2020.12.024.

Hesselbo, S.P., Robinson, S.A., Surlyk, F. and Piasecki, S. 2002. Terrestrial and marine extinction at the Triassic-Jurassic boundary synchronized with major carbon-cycle perturbation: A link to initiation of massive volcanism? *Geology*, **30**(3), 251-254.

Hesselbo, S.P., Robinson, S.A. and Surlyk, F. 2004. Sea-level change and facies development across potential Triassic–Jurassic boundary horizons, SW Britain. *Journal of the Geological Society*, **161**(3), 365-379.

Hohl, S.V., Viehmann, S., 2021. Stromatolites as geochemical archives to reconstruct microbial habitats through deep time: potential and pitfalls of novel radiogenic and stable isotope systems. *Earth-Sci. Rev*. **218**, 103683.

Holmden, C., & Hudson, J. D., 2003. 87Sr/86Sr and Sr/Ca Investigation of Jurassic mollusks from Scotland: Implications for paleosalinities and the Sr/Ca ratio of seawater. *Geological Society of America Bulletin*, **115**(10), 1249-1264.

Hren, M.T. and Sheldon, N.D., 2012. Temporal variations in lake water temperature: paleoenvironmental implications of lake carbonate $\delta^{18}O$ and temperature records. *Earth and Planetary Science Letters*, **337–338**, 77–84.

Hren, MT, Sheldon, ND., 2020. Terrestrial microbialites provide constraints on the mesoproterozoic atmosphere. *Depositional Record*, **6**, 4–20. https://doi.org/10.1002/dep2.79

Huntington, K.W., Eiler, J.M, Affek, H.P., Guo, W., Bonifacie, M., Yeung, L.Y., Thiagarajan, N., Passey, B., Tripati, A., Daëron, M. & Came, R., 2009. Methods and limitations of 'clumped'CO2 isotope (Δ47) analysis by gas-source isotope ratio mass spectrometry. *Journal of Mass Spectrometry*, **44**(9), 1318-1329.

Ibarra, Y., Corsetti, F.A., Greene, S.E., Bottjer, D.J. 2014. Microfacies of the Cotham Marble: a tubestone carbonate microbialite from the Upper Triassic, southwestern U.K. *Palaios*, **29** (1/2), 1-15.

Ibarra, Y., Corsetti, F.A., Greene, S.E., Bottjer, D.J. 2015. Microfacies of the Cotham Marble: a tubestone carbonate microbialite from the Upper Triassic, southwestern U.K.: A reply. *Palaios*, **30** (11/12), pp. 806-809.

Ibarra, Y., Corsetti, F.A., Greene, S.E., Bottjer, D.J. 2016. A microbial carbonate response in synchrony with the end-Triassic mass extinction across the SW UK. *Sci. Rep.*, **6**, p. 19808.

Kalkowsky, E., 1908. Oolith und Stromatolith im norddeutschen Buntsandstein. *Zeitschrift der Deutschen geologischen Gesellschaft*, **60**, 68–125, 3 figs., pls. IV–XI

Kele, S., Breitenbach, S.F.M., Capezzuoli, E., Meckler, A.N., Ziegler, M., Millan, I.M., Kluge, T., Deák, J., Hanselmann, K., John, C.M., Yan, H., Liu, Z., Bernasconi, S.M., 2015. Temperature dependence of oxygen- and clumped isotope fractionation in carbonates: a study of travertines and tufas in the 6–95 °C temperature range. *Geochim. Cosmochim. Acta*, **168**, 172-192.

Kendall, C.G.S.C. and Skipwith, P.A.D.E., 1968. Recent Algal Mats of a Persian Gulf Lagoon. *Journal of Sedimentary Research*, **38** (4), 1040-1058.

Kennard, J.M. and James, N.P., 1986. Thrombolites and stromatolites: two distinct types of microbial structures. *Palaios*, **1**, 492–503.

Kim, S.-T., & O'Neil, J.R., 1997. Equilibrium and nonequilibrium oxygen isotope effects in synthetic carbonates. *Geochimica et Cosmochimica Acta,* **61**(16), 3461-3475.

Kirk, R. 2017. *Development of clumped isotope techniques and their application to palaeoclimate studies.* Ph.D thesis, University of East Anglia.

Korte, C., Kozur, H.W., Veizer, J., 2005. $\Delta^{13}C$ and $\delta^{18}O$ values of Triassic brachiopods and carbonate rocks as proxies for coeval seawater and palaeotemperature. *Palaeogeogr. Palaeoclimatol. Palaeoecol*. **226** (3–4), 287–306. https://doi.org/10.1016/j.palaeo.2005.05.018.

Krumbein, W.E. 2008. Biogenerated rock structures. *Space Science Reviews*, **135**, 81–94.

Lee, J.-H., 2021. Stromatolite, In: Elias, S. and Alderton, D. (Eds.), *Encyclopedia of Geology (Second Edition)*. Academic Press, 375-388. https://doi.org/10.1016/B978-0-12-409548-9.11974-8

Ludwig, R., Theobald, G., 1852. Ueber die Mitwirkung der Pflanzen bei der Ablagerung des kohlensauren Kalkes. *Annalen für Physik und Chemie*, **87**, 91-107.

Mander, L., Twitchett, R.J., Benton, M.J., 2008. Palaeoecology of the late Triassic extinction event in the SW UK. *J. Geol. Soc*. **165**, 319–332.

Martin-Bello, Leticia, Arenas, Concha, Andrews, Julian, Alonso Zara, Ana M. and Marca, Alina (2019) Lacustrine stromatolites as multi-scale recorders of climate change: Insights from the Miocene Ebro Basin. *Palaeogeography, Palaeoclimatology, Palaeoecology*, **530**. 312-329. ISSN 0031-0182

Mata, SA, Harwood, CL, Corsetti, FA, Stork, NJ, Eilers, K, Berelson, WM and Spear, JR., 2012. Influence of gas production and filament orientation on stromatolite microfabric. *Palaios*, **27**(3/4), 206–219.

Mayall, M.J., 1979. *Sedimentology of the Rhaetic (upper Triassic) in S.W. Britain*. Ph.D. Thesis, University of Reading. 389p.

Mayall, M.J., 1983. An earthquake origin for synsedimentary deformation in a late Triassic (Rhaetian) lagoonal sequence, southwest Britain. *Geological Magazine*, **120**(6), 613-622.

Mayall, M.J., and Wright, V.P., 2015. Comment to Ibarra et al. Microfacies of the Cotham Marble: a tubestone carbonate microbialite from the Upper Triassic, southwestern U.K. *PALAIOS*, **30**(11/12), 802–805.

McCrea, J.M. 1950. On the isotopic chemistry of carbonates and a paleotemperature scale. J. Chem. Phys., **18**, 849-857.

Nitti, A., Daniels, C. A., Siefert, J., Souza, V., Hollander, D. and Breitbart, M. 2012. Spatially resolved genomic, stable isotopic, and lipid analyses of a modern freshwater microbialite from Cuatro Ciénegas, Mexico. *Astrobiology*, **12**, 685–698.

Nutman, A.P., Bennett, V.C., Friend, C.R.L., Kranendonk, M.J.V., and Chivas, A.R., 2016. Rapid emergence of life shown by discovery of 3,700-million-year-old microbial structures. *Nature,* **537**, 535–538. https://doi.org/10.1038/nature19355

Owen, E., 1754. *Observations on the Earths, Rocks, Stones and Minerals, for some Miles about Bristol and on the Nature of the Hot-Well and the Virtues of its Water.* W. Johnston, London.

Pálfy, J., Demény, A., Hass, J., Hetényi, M., Orchard, M.J., and Veto, I., 2001. Carbon isotope anomaly and other geochemical changes at the Triassic-Jurassic boundary from a marine section in Hungary. Geology, **29**, 1047–1050.

Paul, A., Lokier, S.W., Sherry, A., Andrade, L.L., Court, W.M., van der Land, C., Dutton, K.E. and Head, I.M. (2021), Erosion-initiated stromatolite and thrombolite formation in a present-day coastal sabkha setting. *Sedimentology*, **68**, 382-401. https://doi.org/10.1111/sed.12783

Paul., J., Peryt, T.M., and Burne, R.V., 2010. Kalkowsky's Stromatolites and Oolites (Lower Buntsandstein, Northern Germany). In: *Advances in Stromatolite Geobiology (eds J Reitner, NV Quéric, G Arp). Lecture Notes in Earth Sciences*, **131**, 13–28.

Park, R.K. 1977. The preservation potential of some recent stromatolites. *Sedimentology*, **24**: 485-506.

Paxton, R.B., 2022. *Clumped isotope geochemistry of British Middle and Upper Jurassic sedimentary archives*. PhD thesis, University of East Anglia

Petroff, A.P.; Sim, M.S., Maslov, A.; Krupenin, M.; Rothman, D.H.; Bosak, T., 2010. Biophysical basis for the geometry of conical stromatolites. *Proc. Natl. Acad. Sci.*, **107**, 9956–9961.

Petryshyn, V.A., Corsetti, F.A., Frantz, C.M., Lund, S.P. and Berelson, W.M., 2016. Magnetic susceptibility as a biosignature in stromatolites. *Earth and Planetary Science Letters*, **437**, 66–75.

Petryshyn, V.A., Greene, S.E., Farnsworth, A., Lunt, D.J., Kelley, A., Gammariello, R., Ibarra, Y., Bottjer, D.J., Tripati, A., Corsetti, F.A., 2020. The role of temperature in the initiation of the end-Triassic mass extinction. *Earth-Sci. Rev.*, **208**, 103266, 10.1016/j.earscirev.2020.103266

Radley, J.D. and Carpenter, S.C., 1998. The Late Triassic strata of Manor Farm, Aust, south Gloucestershire. *Proceedings of the Bristol Naturalists' Society*, **58**, 57–66

Richardson, L., 1904. Notes on the Rhaetic rocks around Charfield, Gloucestershire. *Geological Magazine*, **41**, 532-5.

Riding, R., 2010. The Nature of Stromatolites: 3,500 Million Years of History and a Century of Research In: *Advances in Stromatolite Geobiology (eds J Reitner, NV Quéric, G Arp). Lecture Notes in Earth Sciences*, **131**, 29–74.

Scoffin, T.P., 1987. An Introduction to Carbonate Sediments and Rocks. Blackie, Glasgow, London. 274 pp.

Siahi, M., Hofmann, A., Master, S., Wilson, A., Mayr, C., 2018. Trace element and stable (C, O) and radiogenic (Sr) isotope geochemistry of stromatolitic carbonate rocks of the Mesoarchaean Pongola Supergroup: implications for seawater composition. *Chem. Geol*. **476**, 389–406.

Simms, M.J. 2003. Uniquely extensive seismite from the latest Triassic of the United Kingdom: evidence for bolide impact? *Geology*, **31**, 557-560

Simms, M.J. 2007. Uniquely Extensive Soft-Sediment Deformation in the Rhaetian of the UK: Evidence for Earthquake or Impact? *Triassic-Jurassic Boundary Events: Problems, Progress, Possibilities*, **244**, no. 1, 407–23.

Stickle, W.B., and Diehl, W.J., 1987. Effects of salinity on echinoderms, in Jangoux, M., and Lawrence, J.M., eds., *Echinoderm Studies II*: Rotterdam, A.A. Balkema, p. 235-285.

Suosaari, E.P.; Awramik, S.M.; Reid, R.P.; Stolz, J.F.; Grey, K., 2018. Living Dendrolitic Microbial Mats in Hamelin Pool, Shark Bay, Western Australia. *Geosciences*, **8**(6), 212-229. https://doi.org/10.3390/geosciences8060212

Suosaari, E.P.; Reid, R.P.; Abreu Araujo, T.A.; Playford, P.E.; Holley, D.K.; McNamara, J.K.; Eberli, G.P., 2016. Environmental pressures influencing living stromatolites in Hamelin Pool, Shark Bay, Western Australia. *Palaios*, **31**, 483–496.

Swart, P.K., Burns, S., & Leder, J., 1991. Fractionation of the stable isotopes of oxygen and carbon in carbon dioxide during the reaction of calcite with phosphoric acid as a function of temperature and technique. *Chemical Geology: Isotope Geoscience section,* **86**(2), 89-96.

Swift, A., and Martill, D.M. 1999. *Fossils of the Rhaetian Penarth Group*. Blackwell for the Paleontological Association, London

Talbot, M.R., 1990. A review of the palaeohydrological interpretation of carbon and oxygen isotopic ratios in primary lacustrine carbonates. *Chemical Geology*, **80**, 261–279.

Thompson, B., 1894. Landscape Marble. *Quarterly Journal of the Geological Society*, **50** (1-4), 393 – 410. doi.org/10.1144/GSL.JGS.1894.050.01-04.2

Urey, H. C., Lowenstam, H. A., Epstein, S., and McKinney, C. R. 1951. Measurement of paleotemperatures and temperatures of the Upper Cretaceous of England, Denmark, and the south-eastern United States, *Geol. Soc. Am. Bull*., **62**, 399–416, https://doi.org/10.1130/0016-7606(1951)62[399:MOPATO]2.0.CO;2,.

Walter, M.R., Buick, R., Dunlop, J.S.R., 1980. Stromatolites 3400–3500 Myr old from the North Pole area, Western Australia. *Nature*, **284**, pp. 443-445

Ward, P.D., Haggart, J.W., Carter, E.S., Wilbur, D., Tipper, H.W., and Evans, T., 2001. Sudden productivity collapse associated with the Triassic-Jurassic boundary mass extinction. **Science**, **292**, 1148–1151.

Warrington, G., Audley-Charles, M.G., Elliott, R.E., Evans, W.B., Ivimey-Cook, H.C., Kent, P.E., Robinson, P.L., Shotton, F.W. and Taylor, F.M. 1980. A correlation of the Triassic rocks in the British Isles. *Special Report of the Geological Society of London*, No.13, 1-78.

Woodward, H.B. 1892. II.—Remarks on the Formation of Landscape Marble. *Geological Magazine*, **9**(3), 110-114. doi:10.1017/S0016756800139354.

Wright, W.P., and Mayall, M.J. 1981. Organism-sediment interactions in stromatolites: An example from the Upper Triassic of South West Britain, C. Monty (Ed.), *Phanerozoic Stromatolites*, Springer-Verglag, Berlin (1981).

Appendix I

Bulk isotope analyses. Distance indicates the stratigraphic position from the base of the specimen.

Sample ID	Facies	$\delta^{13}C$ (‰ VPDB)	$\delta^{18}O$(‰ VPDB)	Distance (mm)
L3SL43	L3	0.36	-2.42	233.00
L3SL42	L3	0.68	-2.06	232.00
L3SL41	L3	0.63	-2.08	231.50
L3SL40	L3	0.67	-1.95	231.00
L3SL39	L3	0.64	-1.92	230.50
L3SL38	L3	0.61	-1.85	230.00
L3SL37	L3	0.66	-1.93	229.50
L3SL36	L3	0.42	-2.27	229.00
L3SL35	L3	0.59	-1.90	228.50
L3SL34	L3	0.65	-1.90	228.00
L3SL33	L3	0.44	-2.09	227.50
L3SL32	L3	0.56	-2.07	227.00
L3MD2	L3	0.73	-1.97	226.50
L3MD1	L3	0.61	-2.15	225.50
L3SL31	L3	0.54	-1.81	224.50
L3SL30	L3	0.55	-1.75	224.00
L3SL29	L3	0.57	-1.84	223.50
L3SL28	L3	0.16	-2.30	223.00
L3SL27	L3	0.49	-1.51	222.50
L3SL26	L3	0.33	-1.43	222.00
L3SL25	L3	0.40	-1.08	221.50
L3SL24	L3	0.40	-0.96	221.00
L3SL23	L3	0.56	-0.64	220.50
L3SL22b	L3	0.46	-0.95	220.00
L3SL22	L3	0.46	-0.97	219.50
L3SL21	L3	0.49	-1.01	219.00
L3SL20	L3	0.59	-0.98	218.50
L3SL19	L3	0.53	-0.98	218.00
L3SL18	L3	0.56	-0.90	217.50
L3SL17	L3	0.54	-1.02	217.00
L3SL16	L3	0.46	-0.99	216.50
L3SL15	L3	0.36	-1.00	216.00
L3SL14	L3	0.42	-0.69	215.50
L3SL13	L3	0.21	-1.04	215.00
L3SL12	L3	0.33	-0.79	214.50
L3SL11	L3	0.45	-0.68	214.00
L3SL10b	L3	0.26	-1.21	213.50
L3SL10	L3	0.41	-0.92	213.00
L3SL9	L3	0.45	-0.91	212.50

L3SL8	L3	0.36	-0.98	212.00
L3SL7	L3	0.32	-0.92	211.50
L3SL6	L3	0.46	-0.91	211.00
L3SL5	L3	0.22	-1.04	210.50
L3SL4	L3	0.17	-1.08	210.00
L3SL3	L3	0.44	-0.75	209.50
L3SL2	L3	0.30	-1.14	209.00
L3SL1	L3	0.34	-1.00	208.50
L3SLB3	L3	0.29	-0.82	208.00
L3SLB2	L3	0.31	-0.72	207.50
L3SLB1	L3	0.42	-0.67	207.00
L2DF50	D2 Fill	0.44	-0.66	206.00
L2D43	D2 Dendr	0.23	-2.12	205.00
L2D41	D2 Dendr	0.72	-1.14	203.00
L2DF49	D2 Fill	0.57	-1.18	203.00
L2D42	D2 Dendr	0.60	-1.28	201.00
L2DF43	D2 Fill	0.47	-0.81	199.00
L2D38	D2 Dendr	0.69	-1.21	198.00
L2DF48	D2 Fill	0.51	-0.60	197.00
L2DF47	D2 Fill	0.70	-0.49	197.00
L2D40	D2 Dendr	0.62	-1.09	196.00
L2D39	D2 Dendr	0.43	-0.64	196.00
L2DF45	D2 Fill	0.72	-0.87	193.00
L2DF46	D2 Fill	0.39	-0.76	192.00
L2DF42	D2 Fill	0.62	-0.85	192.00
L2DF40	D2 Fill	0.53	-1.67	191.00
L2D36	D2 Dendr	0.78	-0.55	191.00
L2D30	D2 Dendr	0.71	-1.07	191.00
L2D37	D2 Dendr	0.76	-1.10	190.00
L2DF39	D2 Fill	0.64	-1.70	190.00
L2DF31	D2 Fill	0.81	-0.71	189.00
L2D29	D2 Dendr	0.60	-1.13	189.00
L2D29	D2 Dendr	0.44	-1.37	189.00
L2D35	D2 Dendr	0.73	-1.13	188.00
L2D25	D2 Dendr	0.74	-1.17	188.00
L2DF38	D2 Fill	0.57	-1.78	187.00
L2DF30	D2 Fill	0.89	-0.40	187.00
L2DF29	D2 Fill	0.95	-0.29	187.00
L2DF33	D2 Fill	0.48	-1.45	186.00
L2DF26	D2 Fill	0.80	-0.50	186.00
L2D24	D2 Dendr	0.65	-1.22	186.00
L2D34	D2 Dendr	0.65	-1.14	185.00
L2DF37	D2 Fill	0.59	-1.63	185.00

L2DF35	D2 Fill	0.49	-1.40	185.00
L2DF27	D2 Fill	0.67	-0.64	184.00
L2D28	D2 Dendr	0.67	-1.05	184.00
L2D31	D2 Dendr	0.63	-1.08	183.00
L2DF34	D2 Fill	0.89	-0.23	183.00
L2DF32	D2 Fill	0.91	-0.43	183.00
L2DF23	D2 Fill	0.86	-0.24	183.00
L2DF28	D2 Fill	0.87	-0.22	182.00
L2DF16	D2 Fill	0.38	-1.57	182.00
L2D26	D2 Dendr	0.53	-1.30	182.00
L2D23	D2 Dendr	0.69	-1.17	181.00
L2D33	D2 Dendr	0.55	-0.97	180.00
L2D32	D2 Dendr	0.64	-1.21	180.00
L2D27	D2 Dendr	0.25	-1.56	180.00
L2D19	D2 Dendr	0.59	-1.28	180.00
L2DF36	D2 Fill	0.62	-1.75	180.00
L2DF15	D2 Fill	0.63	-1.33	180.00
L2DF24	D2 Fill	0.87	-0.45	179.00
L2DF14	D2 Fill	0.65	-1.46	179.00
L2DF17	D2 Fill	0.39	-2.10	178.00
L2DF12	D2 Fill	0.86	-0.40	177.00
L2D20	D2 Dendr	0.70	-1.26	178.00
L2D17	D2 Dendr	0.56	-1.22	178.00
L2D22	D2 Dendr	0.69	-1.32	177.00
L2D11	D2 Dendr	0.41	-1.37	177.00
L2DF21	D2 Fill	0.59	-0.99	175.00
L2DF11	D2 Fill	0.37	-1.59	175.00
L2DF8	D2 Fill	-0.01	-2.05	175.00
L2D18	D2 Dendr	0.59	-1.68	175.00
L2D16	D2 Dendr	0.56	-1.97	175.00
L2D15	D2 Dendr	0.47	-1.36	175.00
L2D13	D2 Dendr	0.66	-1.48	173.00
L2DF10	D2 Fill	0.13	-1.88	173.00
L2DF9	D2 Fill	-0.13	-2.31	171.00
L2DF7	D2 Fill	-0.38	-1.96	171.00
L2D14	D2 Dendr	0.70	-1.29	171.00
L2DF6	D2 Fill	0.09	-1.17	170.00
L2D9	D2 Dendr	0.70	-1.55	170.00
L2DF5	D2 Fill	-0.92	-2.59	169.00
L2DF1	D2 Fill	-0.23	-2.10	169.00
L2D12	D2 Dendr	0.51	-1.90	169.00
L2D10	D2 Dendr	0.61	-1.49	169.00
L2D5	D2 Dendr	0.32	-2.06	169.00
L2DF4	D2 Fill	0.40	-1.36	166.00

L2D2	D2 Dendr	0.51	-2.24	166.00
L2D6	D2 Dendr	-0.59	-2.26	164.00
L2D4	D2 Dendr	0.35	-2.07	164.00
L2DF3	D2 Fill	-0.02	-2.24	163.00
L2DF2	D2 Fill	0.48	-1.59	163.00
L2D1	D2 Dendr	0.75	-1.73	163.00
L2D8	D2 Dendr	0.59	-2.14	162.00
L2D3	D2 Dendr	-0.04	-2.17	161.00
L2D7	D2 Dendr	-0.18	-2.28	160.00
L2S31	L2	0.23	-2.12	158.00
L2S30	L2	0.34	-1.86	157.40
L2S29	L2	0.05	-1.89	156.80
L2S28	L2	0.28	-1.69	156.20
L2S27	L2	0.24	-1.66	155.60
L2S26	L2	0.05	-2.00	155.00
L2S25	L2	0.49	-1.65	154.40
L2S24	L2	0.45	-1.42	153.80
L2S23	L2	0.25	-1.55	153.20
L2S22	L2	0.65	-1.03	152.60
L2S21	L2	0.64	-1.01	152.00
L2S20	L2	0.43	-1.17	151.40
L2S19	L2	0.52	-1.14	150.80
L2S18	L2	0.58	-1.04	150.20
L2S17	L2	0.39	-0.83	149.60
L2S16	L2	0.30	-0.95	149.00
L2S15	L2	0.35	-0.69	148.40
L2S14	L2	0.32	-1.05	147.80
L2S13	L2	0.49	-0.79	147.20
L2S12	L2	0.39	-1.07	146.60
L2S11	L2	0.36	-0.74	146.00
L2S10	L2	0.28	-0.86	145.40
L2S9	L2	0.00	-1.75	144.80
L2S8	L2	0.35	-1.27	144.20
L2S7	L2	0.30	-1.06	143.60
L2S6	L2	0.32	-1.03	143.00
L2S5	L2	0.09	-1.31	142.40
L2S4	L2	0.19	-0.97	141.80
L2S3	L2	0.11	-1.18	141.20
L2S2	L2	-0.04	-1.54	140.60
L2S1	L2	0.03	-1.26	140.00
L1D52	D1 Fill	-0.73	-3.19	134.00
L1D51	D1 Fill	-0.20	-1.83	133.00
L1D50	D1 Fill	-0.04	-1.40	132.00
L1D49	D1 Fill	-0.06	-1.31	131.00

L1D48	D1 Fill	-0.71	-2.33	131.00
L1D47	D1 Fill	-0.28	-1.06	130.00
L1D46	D1 Dendr	-2.97	-7.06	129.00
L1D45	D1 Fill	-0.81	-2.28	128.00
L1D44	D1 Fill	-0.54	-2.23	127.00
L1D42	D1 Fill	0.23	-0.80	125.00
L1D41	D1 Fill	-0.53	-2.14	124.00
L1D40	D1 Fill	0.27	-0.52	123.00
L1D39	D1 Fill	0.52	-0.45	122.00
L1D38	D1 Fill	0.72	-0.89	122.00
L1D37	D1 Fill	0.67	-0.43	121.00
L1D34	D1 Fill	0.76	-0.48	121.00
L1D33	D1 Fill	0.55	-1.18	120.00
L1D32	D1 Fill	0.69	-0.78	120.00
L1D36	D1 Dendr	0.61	-1.02	120.00
L1D35	D1 Fill	0.62	-1.00	120.00
L1D31	D1 Fill	0.48	-1.52	119.00
L1D30	D1 Fill	-0.18	-2.45	119.00
L1D29	D1 Fill	-0.01	-2.25	118.00
L1D25	D1 Dendr	0.66	-0.83	118.00
L1D28	D1 Fill	-1.36	-4.18	117.00
L1D26	D1 Fill	-0.20	-2.50	117.00
L1D24	D1 Fill	0.76	-1.23	116.00
L1D23	D1 Fill	0.54	-1.29	114.00
L1D19	D1 Fill	0.59	-1.33	114.00
L1D22	D1 Dendr	0.76	-1.19	113.00
L1D18	D1 Fill	0.45	-1.65	112.00
L1D16	D1 Fill	0.58	-1.38	112.00
L1D15	D1 Fill	0.15	-2.08	112.00
L1D20	D1 Dendr	0.64	-0.82	111.00
L1D21	D1 Fill	0.58	-1.28	110.00
L1D14	D1 Fill	0.66	-1.09	110.00
L1D17	D1 Fill	0.86	-0.77	109.00
L1D13	D1 Fill	0.76	-1.10	107.00
L1D11	D1 Fill	0.79	-0.48	107.00
L1D12	D1 Fill	0.40	-1.84	106.00
L1D9	D1 Dendr	0.49	-1.11	105.00
L1D8	D1 Dendr	0.57	-1.04	104.00
L1D5	D1 Dendr	0.12	-1.74	103.00
L1D6	D1 Dendr	0.32	-1.62	102.00
L1D4	D1 Fill	-0.09	-1.66	102.00
L1D10	D1 Fill	0.20	-2.21	101.00
L1D2	D1 Dendr	0.21	-1.38	101.00
L1D1	D1 Dendr	0.73	-0.83	101.00

L1D0	D1 Dendr	0.51	-1.00	100.00
L1D3	D1 Fill	-0.26	-1.20	99.00
L1L26	L1	0.27	-1.13	97.6
L1L25	L1	0.22	-0.99	97.2
L1L24	L1	0.21	-1.08	96.8
L1L23	L1	-0.04	-1.25	96.4
L1L22	L1	0.23	-1.02	96
L1L21	L1	0.32	-0.76	95.6
L1L20	L1	0.41	-0.92	95.2
L1L19	L1	0.46	-0.89	94.8
L1L18	L1	0.59	-0.79	94.4
L1L17	L1	0.26	-1.02	94
L1L16	L1	-0.10	-1.29	93.6
L1L15	L1	0.19	-0.76	93.2
L1L14	L1	0.10	-0.93	92.8
L1L13	L1	0.09	-0.82	92.4
L1L12	L1	-0.04	-0.85	92
L1L11	L1	-0.15	-1.28	91.6
L1L10	L1	0.08	-0.77	91.2
L1L9	L1	0.08	-0.77	90.8
L1L8	L1	-0.01	-0.84	90.4
L1L7	L1	-0.07	-0.88	90
L1L6	L1	0.02	-0.57	89.6
L1L5	L1	-0.47	-2.18	89.2
L1L4	L1	0.34	-0.03	88.8
L1L3	L1	0.17	-1.70	88.4
L1L2	L1	0.45	-1.33	88
L1L1	L1	-0.29	-2.43	87.6
L1T10	L1	0.12	-1.21	87.2
L1T9	L1	-0.11	-1.04	86.8
L1T8	L1	-0.13	-0.89	86.4
L1T7	L1	-0.52	-0.95	86
L1T6	L1	-0.31	-0.93	85.6
L1T5	L1	-0.40	-0.88	85.2
L1T5	L1	-0.41	-0.87	84.8
L1T4	L1	-0.25	-0.78	84.4
L1T3	L1	-0.18	-0.71	84
L1T2	L1	-0.14	-0.77	83.6
L1T1	L1	0.02	-0.99	83.2
CMBL 33	L1	-0.64	-0.74	82.8
CMBL 34	L1	0.05	-0.76	82.4
CMBL 35	L1	-0.17	-1.00	82
CMBL 36	L1	0.01	-0.92	81.6

CMBL 37	L1	0.01	-0.85	81.2
CMBL 38	L1	-0.13	-1.02	80.8
CMBL 39	L1	-0.01	-0.75	80.4
CMBL 5	L1	0.14	-0.86	78.4
CMBL 6	L1	0.14	-0.98	78
CMBL 7	L1	0.08	-0.84	77.6
CMBL 8	L1	0.12	-0.66	77.2
CMBL 9	L1	0.22	-0.61	76.8
CMBL 11	L1	0.20	-0.55	76
CMBL 12	L1	0.23	-0.73	75.6
CMBL 13	L1	0.19	-0.88	75.2
CMBL 14	L1	-0.10	-0.88	74.8
CMBL 15	L1	-0.26	-1.05	74.4
CMBL 16	L1	-0.61	-0.86	74
CMBL 17	L1	-1.09	-1.02	73.6
CMBL 18	L1	-1.36	-1.17	73.2
CMBL 19	L1	-1.59	-1.04	72.8
CMBL 20	L1	-1.85	-1.02	72.4
CMBL 21	L1	-2.09	-1.14	72
CMBL 22	L1	-1.57	-1.14	71.6
CMBL 23	L1	-0.85	-1.13	71.2
CMBL 24	L1	-0.73	-1.55	70.8
CMBL 25	L1	-0.63	-1.00	70.4
CMBL 26	L1	-0.67	-0.91	70
CMBL 27	L1	-0.32	-0.84	69.6
CMBL 28	L1	-0.53	-1.02	69.2
CMBL 29	L1	-0.50	-0.91	68.8
CMBL 30	L1	0.00	-0.92	68.4
CMBL 31	L1	0.07	-0.96	68
CMBL 32	L1	0.22	-0.85	67.6
CMBL 33	L1	0.20	-0.74	67.2
CMBL 34	L1	0.13	-0.83	66.8
CMBL 35	L1	0.03	-0.82	66.4
CMBL 36	L1	0.02	-0.81	66
CMBL 37	L1	-0.24	-1.16	65.6
CMBL 38	L1	-0.31	-1.14	65.2
CMBL 39	L1	-0.36	-1.01	64.8
CMBL 40	L1	-0.23	-0.77	64
CMBL 41	L1	-0.30	-0.86	63.6
CMBL 42	L1	-0.21	-0.87	63.2
CMBL 43	L1	-0.17	-0.87	62.8
CMBL 44	L1	-0.35	-0.95	62.4
CMBL 45	L1	-0.01	-0.87	62
CMBL 46	L1	-0.03	-1.12	61.6

CMBL 47	L1	-0.21	-0.94	61.2
CMBL 48	L1	-0.21	-0.95	60.8
CMBL 49	L1	-0.43	-1.21	60.4
CMBL 50	L1	-0.42	-0.91	60
CMBL 51	L1	-0.50	-0.84	59.6
CMBL 52	L1	-0.24	-0.88	59.2
CMBL 53	L1	0.08	-0.90	58.8
CMBL 54	L1	0.46	-1.28	58.4
CMBL 55	L1	0.62	-1.31	58
Thrmb1	Thrombolite	0.93	-1.45	57
Thrmb2	Thrombolite	0.85	-1.20	56
Thrmb3	Thrombolite	0.88	-1.67	55
Thrmb4	Thrombolite	0.95	-1.44	54
Thrmb5	Thrombolite	0.87	-1.59	53
Thrmb6	Thrombolite	0.89	-1.45	52
SL1	Mixed layers + shells	1.13	-1.57	51.5
SL2	Mixed layers + shells	0.97	-1.84	50.5
SL3	Mixed layers + shells	0.94	-1.91	49.5
SL4	Mixed layers + shells	0.65	-2.38	48.5
SL6	Mixed layers + shells	1.05	-1.64	46.5
SL8	Mixed layers + shells	0.85	-1.89	44.5
SL9	Mixed layers + shells	0.54	-2.47	43.5
SL10	Mixed layers + shells	0.95	-1.64	42.5
SL11	Mixed layers + shells	0.81	-1.88	42.5
SL12	Mixed layers + shells	0.75	-1.89	41.5
SL13	Mixed layers + shells	0.45	-2.14	40.5
SL14	Mixed layers + shells	0.74	-1.98	39.5
SL15	Mixed layers + shells	0.69	-1.84	38.5
SL16	Mixed layers + shells	0.63	-1.86	37.5
SL17	Mixed layers + shells	0.75	-1.93	36.5
SL18	Mixed layers + shells	0.76	-1.80	35.5

SL19	Mixed layers + shells	0.10	-2.98	34.5
SL20	Mixed layers + shells	0.56	-1.80	33.5
Shell to SL20	Shells	0.63	-1.79	33.5
SL21	Mixed layers + shells	0.96	-1.47	32.5
SL22	Mixed layers + shells	-1.21	-4.02	31.5
Shells to SL	Shells	0.38	-1.69	31.5
CMB1	Mixed layers + shells	0.75	-1.62	35.5
CMB3	Mixed layers + shells	0.80	-1.44	34.5
CMB4	Mixed layers + shells	0.80	-1.53	34
CMB5	Mixed layers + shells	0.75	-1.68	33.5
CMB6	Mixed layers + shells	0.67	-1.76	33
CMB7	Mixed layers + shells	0.44	-2.22	32.5
CMB9	Mixed layers + shells	0.46	-2.00	32
CMB10	Mixed layers + shells	0.52	-1.68	31
CMB12	Mixed layers + shells	0.52	-1.71	30
CMB13	Mixed layers + shells	0.45	-1.84	29
CMB14	Mixed layers + shells	0.06	-2.46	28
CMB15	Mixed layers + shells	0.44	-1.74	27
CMB16	Mixed layers + shells	0.11	-2.07	26
CMB20	Mixed layers + shells	0.17	-2.06	25
CMB21	Mixed layers + shells	-0.40	-2.82	24
CMB23	Mixed layers + shells	-0.01	-2.09	23
CMB24	Mixed layers + shells	-0.18	-2.52	22
CMB26	Mixed layers + shells	-0.05	-2.31	21
CMB27	Mixed layers + shells	-0.02	-2.38	20
CMB28	Mixed layers + shells	-0.10	-2.45	19
CMB29	Mixed layers + shells	-0.16	-2.63	18

CMB30	Mixed layers + shells	-1.06	-4.00	17
CMB31	Mixed layers + shells	-0.34	-2.53	16
CMB32	Mixed layers + shells	-0.54	-2.85	15
CMB33	Mixed layers + shells	-0.41	-2.43	14
CMB37	Mixed layers + shells	-0.47	-2.63	13
CMB38	Mixed layers + shells	-0.43	-2.55	12
CMB39	Mixed layers + shells	-0.24	-2.61	11
WL1	Low layers + shells	-0.06	-2.43	10
WL3	Low layers + shells	0.00	-2.35	9
WL4	Low layers + shells	0.03	-2.49	9
WL5	Low layers + shells	-0.08	-2.54	9
WL6	Low layers + shells	-0.07	-2.64	9
WL7	Low layers + shells	-0.61	-3.60	8
WL8	Low layers + shells	0.02	-2.48	8
WL9	Low layers + shells	-0.23	-2.76	8
WL10	Low layers + shells	0.03	-2.48	8
WL11	Low layers + shells	-0.14	-2.69	7
WL12	Low layers + shells	-0.08	-2.51	7
WL13	Low layers + shells	-0.10	-2.52	7
WL16	Low layers + shells	-0.19	-2.78	7
WL17	Low layers + shells	0.00	-2.49	6
WL18	Low layers + shells	-0.10	-2.52	6
WL19	Low layers + shells	-0.07	-2.65	6
WL20	Low layers + shells	-0.11	-2.54	6
WL21	Low layers + shells	-0.12	-2.73	5
WL21	Low layers + shells	-0.06	-2.62	5

WL22	Low layers + shells	-0.04	-2.55	5
WL23	Low layers + shells	-0.16	-2.65	5
WL24	Low layers + shells	-0.16	-2.75	4
WL25	Low layers + shells	-0.08	-2.68	4
WL27	Low layers + shells	-0.10	-2.39	4
WL28	Low layers + shells	0.11	-2.34	4
WL29	Low layers + shells	0.05	-2.50	3
WL30	Low layers + shells	-0.07	-2.53	3
WL31	Low layers + shells	-0.02	-2.47	3
WL32	Low layers + shells	0.14	-2.28	3
WL33	Low layers + shells	-0.04	-2.58	2
WL34	Low layers + shells	-0.10	-2.63	2
WL35	Low layers + shells	-0.80	-3.94	2
WL36	Low layers + shells	-0.14	-2.54	1
WL37	Low layers + shells	-0.35	-2.65	1
WL38	Low layers + shells	-1.06	-2.55	0
L2SF19	Depression A	0.12	-1.35	141.3
L2SF19	Depression A	0.12	-1.35	141.3
L2SF18	Depression A	-0.07	-1.34	140.6
L2SF17	Depression A	-0.14	-1.19	139.9
L2SF16	Depression A	-0.17	-1.31	139.2
L2SF15	Depression A	-0.38	-1.93	138.5
L2SF14bis	Depression A	0.26	-0.77	137.8
L2SF14	Depression A	-0.45	-2.03	137.1
L2SF13	Depression A	-0.48	-1.97	136.4
L2SF12	Depression A	-0.17	-1.29	135.7
L2SF11	Depression A	-0.04	-1.10	135.0
L2SF10	Depression A	-0.20	-1.33	134.3
L2SF9	Depression A	-0.19	-1.28	133.6
L2SF8	Depression A	-0.17	-1.21	132.9
L2SF7	Depression A	-0.13	-1.21	132.2
L2SF6	Depression A	-0.21	-1.41	131.5

L2SF5	Depression A	-0.38	-1.93	130.8
L2SF4	Depression A	-0.21	-1.65	130.1
L2SF3	Depression A	-0.15	-1.39	129.4
L2SF2	Depression A	-0.07	-1.22	128.7
L2SF1	Depression A	-1.74	-4.76	128.0
L2SF40	Depression B	-0.28	-2.34	152.5
L2SF39	Depression B	-0.34	-1.99	152
L2SF38	Depression B	-0.48	-1.89	151.5
L2SF37	Depression B	-0.51	-1.86	151
L2SF36	Depression B	-0.50	-1.89	150.5
L2SF35	Depression B	-0.95	-2.68	150
L2SF34	Depression B	-0.62	-2.12	149.5
L2SF33	Depression B	-0.47	-1.92	149
L2SF32	Depression B	-0.30	-1.95	148.5
L2SF31	Depression B	0.29	-1.42	148
L2SF30	Depression B	0.20	-1.80	147.5
L2SF29	Depression B	0.28	-1.78	147
L2SF28	Depression B	-0.01	-1.76	146.5
L2SF27	Depression B	0.04	-1.72	146
L2SF26	Depression B	0.06	-1.77	145.5
L2SF25	Depression B	0.21	-1.63	145
L2SF24	Depression B	0.55	-1.19	144.5
L2SF23	Depression B	0.56	-1.14	144
L2SF22	Depression B	0.37	-1.26	143.5
L2SF21	Depression B	0.53	-1.20	143
L2SF20	Depression B	0.44	-1.39	142.5
L2SF19bis	Depression B	0.28	-1.42	142
L2SF18ter	Depression B	0.32	-1.19	141.5
L2SF18bis	Depression B	0.08	-1.47	141
L2SF17bis	Depression B	0.12	-1.31	140.5
L2SF16ter	Depression B	0.30	-0.99	140
L2SF16bis	Depression B	0.40	-0.83	139.5
L2SF15ter	Depression B	0.30	-0.91	139
L2SF15bis	Depression B	0.11	-0.99	138.5
L2F28	Depression C	-1.61	-3.77	147.6
L2F27	Depression C	-1.99	-4.09	146.8
L2F26	Depression C	-1.58	-3.69	146
L2F25	Depression C	0.13	-2.38	145.2
L2F24	Depression C	-1.43	-3.98	144.4
L2F23	Depression C	-1.58	-3.56	143.6
L2F22	Depression C	-1.44	-3.50	142.8
L2F21	Depression C	-1.12	-3.27	142

L2F20	Depression C	-1.00	-3.16	141.2
L2F19	Depression C	-0.71	-2.73	140.4
L2F18	Depression C	-0.64	-2.77	139.6
L2F17	Depression C	-0.04	-1.93	138.8
L2F16	Depression C	0.17	-1.63	138
L2F15	Depression C	0.26	-1.41	137.2
L2F14	Depression C	0.37	-1.08	136.4
L2F13	Depression C	0.22	-1.31	135.6
L2F12	Depression C	0.30	-1.30	134.8
L2F11	Depression C	0.34	-1.30	134
L2F10	Depression C	0.38	-1.17	133.2
L2F9	Depression C	0.13	-1.70	132.4
L2F8	Depression C	-0.02	-2.07	131.6
L2F7	Depression C	0.37	-1.48	130.8
L2F6	Depression C	0.27	-1.45	130
L2F5	Depression C	0.36	-1.53	129.2
L2F4	Depression C	0.05	-2.13	128.4
L2F3	Depression C	0.14	-1.90	127.6
L2F2	Depression C	-0.29	-2.28	126.8
L2F1	Depression C	-0.25	-2.32	126

Appendix II

Clumped Isotope Analyses.

measurement ID	Sam ID	d13C/vpdb	d18O CO2/vsmo	d18O CO3 /vsmo	d18O CO3/vpd	D47	D48	D49	D47	D47(ARF)	D47(ARF)
			Carbon Dioxide	Carbonate	Carbonate	LRF (87°C)	LRF (87°C	LRF (87°C	LRF (correctec	87°C	25°C
MIRA_220630_CM-L3A-1	CM-L3A	0.425	38.332	29.683	-1.142	-0.362	-0.149	-4.936	n/a	0.593	0.655
MIRA_220630_CM-L3A-2	CM-L3A	0.473	38.605	29.953	-0.879	-0.333	-0.041	2.123	n/a	0.626	0.688
MIRA_220630_CM-L3A-3	CM-L3A	0.533	38.532	29.881	-0.950	-0.361	-0.139	3.665	n/a	0.594	0.656
MIRA_210720_CMA-D2f	CM-D2f	-1.551	35.426	26.800	-3.938	-0.238	-0.104	-19.495	n/a	0.568	0.630
MIRA_220615_CMA-D2f-1	CM-D2f	-1.584	35.542	26.916	-3.826	-0.297	-0.151	-14.971	n/a	0.669	0.731
MIRA_220615_CMA-D2f-2	CM-D2f	-1.584	35.471	26.845	-3.894	-0.337	-0.141	-14.853	n/a	0.621	0.683
MIRA_220615_CMA-D2f-3	CM-D2f	-1.568	35.530	26.904	-3.837	-0.332	-0.119	-15.054	n/a	0.628	0.690
MIRA_220617_CM-D2f-1	CM-D2f	0.493	38.790	30.137	-0.701	-0.376	-0.205	-18.553	n/a	0.577	0.639
MIRA_220617_CM-D2f-2	CM-D2f	0.473	38.735	30.083	-0.754	-0.338	-0.140	-13.396	n/a	0.621	0.683
MIRA_220617_CM-D2f-3	CM-D2f	0.487	38.784	30.131	-0.708	-0.361	-0.158	-16.444	n/a	0.594	0.656
MIRA_220623_CM-D2D-1	CM-D2D	-0.022	37.681	29.037	-1.768	-0.400	-0.170	-21.710	n/a	0.548	0.610
MIRA_220623_CM-D2D-2	CM-D2D	0.047	37.706	29.062	-1.744	-0.338	-0.134	-15.762	n/a	0.620	0.682
MIRA_220623_CM-D2D-3	CM-D2D	0.073	37.737	29.093	-1.714	-0.390	-0.205	-12.722	n/a	0.560	0.622
MIRA_220808_CM-D2D	CM-D2D	0.103	38.288	29.640	-1.184	-0.314	-0.098	-17.997	n/a	0.640	0.702
MIRA_220616_CM-L2A-1	CM-L2A	-0.575	37.819	29.174	-1.635	-0.373	-0.145	-16.162	n/a	0.580	0.642
MIRA_220616_CM-L2A-2	CM-L2A	-0.591	37.834	29.189	-1.621	-0.393	-0.239	-22.308	n/a	0.557	0.619
MIRA_220616_CM-L2A-3	CM-L2A	-0.617	37.726	29.082	-1.725	-0.327	-0.170	-20.023	n/a	0.633	0.695
MIRA_220701_CM-D1F-1	CM-D1F	0.450	39.105	30.449	-0.398	-0.349	-0.094	-16.338	n/a	0.608	0.670
MIRA_220701_CM-D1F-2	CM-D1F	0.373	39.007	30.352	-0.493	-0.314	-0.193	-7.472	n/a	0.649	0.711
MIRA_220701_CM-D1F-3	CM-D1F	0.415	38.995	30.340	-0.505	-0.344	-0.070	3.513	n/a	0.613	0.675
MIRA_220620_CM-D1D-1	CM-D1D	0.404	38.266	29.617	-1.205	-0.375	-0.182	-25.589	n/a	0.577	0.639
MIRA_220620_CM-D1D-2	CM-D1D	0.393	38.237	29.588	-1.234	-0.301	-0.075	-19.333	n/a	0.664	0.726
MIRA_220621_CM-D1D-3	CM-D1D	0.425	38.409	29.759	-1.068	-0.356	-0.110	-26.338	n/a	0.599	0.661
MIRA_210628_CM-T1	CM-T1	0.551	38.445	29.795	-1.033	-0.219	-0.189	-15.945	n/a	0.589	0.651
MIRA_220621_CM-T1-1	CM-T1	0.547	38.421	29.771	-1.056	-0.324	-0.148	-13.810	n/a	0.637	0.699
MIRA_220621_CM-T1-2	CM-T1	0.573	38.439	29.789	-1.039	-0.377	-0.180	-11.471	n/a	0.575	0.637
MIRA_220808_CM-T1	CM-T1	0.559	39.002	30.347	-0.497	-0.317	-0.118	-16.475	n/a	0.636	0.698
MIRA_210521_CM-L1up	CM-L1up	-0.835	38.433	29.783	-1.045	-0.270	-0.071	-4.804	-0.215	0.600	0.662
MIRA_210602_CM-L1up	CM-L1up	-0.800	38.398	29.748	-1.078	-0.247	-0.214	-9.205	-0.247	0.564	0.626
MIRA_210603_CM-L1up	CM-L1up	-0.844	38.350	29.701	-1.124	-0.251	-0.167	-9.941	-0.242	0.570	0.632
MIRA_220808_CM-L1up	CM-L1up	-0.773	38.855	30.201	-0.639	-0.337	-0.136	-22.291	n/a	0.614	0.676
MIRA_220706_CM-gl-1	CM-gl	0.004	38.441	29.791	-1.037	-0.353	-0.198	-17.064	n/a	0.603	0.665
MIRA_220706_CM-gl-2	CM-gl	-0.012	38.428	29.778	-1.049	-0.301	-0.047	-8.790	n/a	0.664	0.726
MIRA_220706_CM-gl-3	CM-gl	-0.017	38.409	29.759	-1.068	-0.338	-0.152	-9.518	n/a	0.620	0.682
MIRA_220624_CM-L1low-	CM-L1low	-0.419	38.408	29.758	-1.068	-0.339	-0.137	-20.153	n/a	0.619	0.681
MIRA_220624_CM-L1low-	CM-L1low	-0.418	38.422	29.772	-1.055	-0.342	-0.184	-19.244	n/a	0.616	0.678
MIRA_220624_CM-L1low-	CM-L1low	-0.402	38.499	29.848	-0.981	-0.330	-0.151	-13.458	n/a	0.630	0.692
MIRA_220805_CM-c	CM-c	0.733	37.821	29.176	-1.634	-0.314	-0.158	-12.574	n/a	0.640	0.702
MIRA_220808_CM-c	CM-c	0.706	38.317	29.668	-1.156	-0.280	-0.048	-19.024	n/a	0.678	0.740
MIRA_220705_CM-TR-1	CM-TR	0.399	38.025	29.378	-1.437	-0.316	-0.099	-23.209	n/a	0.647	0.709
MIRA_220705_CM-TR-2	CM-TR	0.553	38.073	29.426	-1.391	-0.326	-0.070	1.537	n/a	0.635	0.697
MIRA_220705_CM-TR-3	CM-TR	0.443	38.045	29.398	-1.418	-0.320	-0.047	12.596	n/a	0.642	0.704
MIRA_210720_CMA-af1	CM-af1	0.381	37.474	28.832	-1.967	-0.191	-0.072	-21.881	n/a	0.621	0.683
MIRA_220805_CM-af1-1	CM-af1	0.315	37.770	29.125	-1.683	-0.308	-0.102	-12.138	n/a	0.647	0.709
MIRA_220805_CM-af1-2	CM-af1	0.315	37.737	29.092	-1.715	-0.320	-0.087	-16.624	n/a	0.634	0.696
MIRA_220707_CM-b-1	CM-b	-0.469	36.885	28.248	-2.534	-0.308	-0.108	-17.913	n/a	0.656	0.718
MIRA_220707_CM-b-2	CM-b	-0.466	36.946	28.308	-2.476	-0.305	-0.155	-12.390	n/a	0.659	0.721
MIRA_220707_CM-b-3	CM-b	-0.426	36.984	28.346	-2.439	-0.336	-0.148	-9.443	n/a	0.623	0.685
MIRA_210518_CM-Vein	CM-vein	-2.236	31.630	23.037	-7.589	-0.309	-0.053	-6.773	-0.282	0.524	0.586
MIRA_210519_CM-Vein	CM-vein	-2.201	31.619	23.025	-7.600	-0.271	0.045	-11.714	-0.234	0.578	0.640
MIRA_210520_CM-Vein	CM-vein	-2.286	31.541	22.948	-7.675	-0.261	0.244	10.151	-0.216	0.599	0.661

Period	Transfer function
18.05.2021 – 03.06.2021	1.13753 x Δ47(LRF 87) + 0.84473
28.06.2021 – 20.07.2021	1.1031 x Δ47(LRF 87) + 0.8313
15.06 2022- 07.07.2022	1.16945 x Δ47(LRF 87) + 1.01602
05.08.2022 – 08.08.2022	1.1257 x Δ47(LRF 87) + 0.9935

Transfer functions used to correct local reference frame data to the CDES reference frame at 87°C, with reference to their time periods of use, as described in Section 3.8.3. CDES: Carbon Dioxide Equilibrium Scale.